

Utah State University

DigitalCommons@USU

All Graduate Theses and Dissertations

Graduate Studies

12-2021

Absolute Neutral Densities and Temperatures and Their Climatologies in the Middle Atmosphere Using an Optimal Estimation Method with Rayleigh-Scatter Lidar Observations Obtained at Utah State University

Jonathan L. Price
Utah State University

Follow this and additional works at: <https://digitalcommons.usu.edu/etd>

 Part of the [Physics Commons](#)

Recommended Citation

Price, Jonathan L., "Absolute Neutral Densities and Temperatures and Their Climatologies in the Middle Atmosphere Using an Optimal Estimation Method with Rayleigh-Scatter Lidar Observations Obtained at Utah State University" (2021). *All Graduate Theses and Dissertations*. 8225.
<https://digitalcommons.usu.edu/etd/8225>

This Dissertation is brought to you for free and open access by the Graduate Studies at DigitalCommons@USU. It has been accepted for inclusion in All Graduate Theses and Dissertations by an authorized administrator of DigitalCommons@USU. For more information, please contact digitalcommons@usu.edu.



ABSOLUTE NEUTRAL DENSITIES AND TEMPERATURES AND THEIR CLIMATOLOGIES IN
THE MIDDLE ATMOSPHERE USING AN OPTIMAL ESTIMATION METHOD WITH
RAYLEIGH-SCATTER LIDAR OBSERVATIONS OBTAINED AT
UTAH STATE UNIVERSITY

by

Jonathan L. Price

A dissertation submitted in partial fulfillment
of the requirements for the degree

of

DOCTOR OF PHILOSOPHY

in

Physics

Approved:

Vincent B. Wickwar, Ph.D.
Major Professor

D. Mark Riffe, Ph.D.
Committee Member

Michael Taylor, Ph.D.
Committee Member

Jed Hancock, Ph.D.
Committee Member

Ludger Scherliess, Ph.D.
Committee Member

D. Richard Cutler, Ph.D.
Interim Vice Provost for
Graduate Studies

UTAH STATE UNIVERSITY
Logan, Utah

2021

Copyright © Jonathan L. Price 2021

All Rights Reserved

ABSTRACT

Absolute Neutral Densities and Temperatures and their Climatologies in the Middle Atmosphere using an Optimal Estimation Method with Rayleigh-Scatter Lidar Observations obtained at Utah State University

by

Jonathan L. Price, Doctor of Philosophy

Utah State University, 2021

Major Professor: Dr. Vincent B. Wickwar
Department: Physics

The Earth's atmosphere is composed of stratified layers characterized by their temperature structure. They are, from the ground up, the troposphere, stratosphere, mesosphere and thermosphere. The least well-known region of earth's atmosphere is the mesosphere. This is due to the difficulty in observing the region remotely. Direct observations can be made using sounding rockets, however due to logistics and cost these are impractical for frequent observation. Remote sensing techniques are the only practical methods for regular study of the mesosphere. There are various types of remote sensing equipment capable of observing this region, however all have their drawbacks. Some are limited to certain altitudes based on metallic layers present, some depend on the ionization within the region and others are limited to nighttime only observations. Rayleigh-scatter lidar is a remote sensing technique, used mainly at nighttime, which has the capability of observing the entirety of the mesosphere, even observing the upper stratosphere and lower thermosphere. Utah State University is

currently home to one of the most powerful Rayleigh lidar systems in the world. It can observe from 40 km to above 115 km. Planned upgrades will extend this range to above 125 km.

The data reduction method for extracting temperature profiles from Rayleigh lidar observations has been around since 1980. In 2015 a new method for reducing Rayleigh lidar temperatures was introduced which uses an optimal estimation method to find the optimal temperature profile which fits the observed data. This new method boasts a more robust uncertainty budget and a more well-defined topmost altitude in the temperature profile. This new method was used to obtain Rayleigh lidar temperature at Utah State University. Temperature climatologies were produced using the new method and compared with those made with the old method. We found good agreement between the two from 45 km to ~85 km. Above this we see periods of large disagreement, likely due to effects from using model temperatures to seed the profile in the old method. The optimal estimation technique was further used to directly obtain absolute neutral densities from Rayleigh lidar observations. This new method is superior to previous methods for obtaining absolute densities in that it does not require normalization to model densities at the lowest altitude and provides well defined uncertainties in the resulting densities. With this new reduction, we now have another state variable with which to study the middle atmosphere. This is used in tandem with the temperatures to study annual trends with climatologies and other common atmospheric features such as tides.

PUBLIC ABSTRACT

Absolute Neutral Densities and Temperatures and their Climatologies in the Middle
Atmosphere using an Optimal Estimation Method with Rayleigh-Scatter Lidar
Observations obtained at Utah State University

Jonathan L. Price

The Earth's atmosphere is comprised of layers which can be defined by their temperature characteristics. These layers are the troposphere, stratosphere, mesosphere and thermosphere. The region where life exists is in the troposphere, however the study of the layers above is important as changes in these regions can directly impact, or indicate significant changes in, weather in the troposphere. The mesosphere is the least well-known region because it is the most difficult to observe. One of the best tools for observing this region is the Rayleigh-scatter lidar. It is capable of remotely observing the entirety of the mesosphere with good time and altitude resolution. Until recently, this tool was used mainly to study temperatures in the middle atmosphere. In this work we introduce a new, reliable method for obtaining the absolute densities in this region. Long term trends were studied, and are presented, in the temperature and densities in the form of climatologies. Additionally, a case study of atmospheric tides is presented which utilizes the new densities and temperatures.

ACKNOWLEDGEMENTS

I would like to thank Vince Wickwar for all the time and effort he has put into mentoring me. Your encouragements and patience with me have been a blessing. Also, your long hours of advice and editorial comments have been invaluable. I would also like to thank Mark Riffe, Mike Taylor, Ludger Scherliess, and Jed Hancock for supporting me with patience and accepting my requests to participate on my committee. I would also like to give a special thanks to Robert Sica and Ali Jalali for hosting me at the University of Western Ontario to guide me in learning the optimal estimation method which has been pivotal in my graduate research. I would also like to thank Alexander Haefele for his valuable feedback on my research. I am grateful for Leda Sox and Matthew Emerick who did the hard work of upgrading the lidar system, making much of my work possible. I would also like to thank Karalee Ransom for all her encouragement and much needed guidance throughout this process.

I would like to thank the Utah NASA Space grant program, the Howard Blood and USU College of Science and Physics Department for their financial support during my graduate work. I would also like to thank Don Rice and Jan Sojka for their support and for the laughs while teaching intermediate and advanced lab. I would like to thank my fellow graduate student Ken Zia and Vanessa Chambers for their friendship. I am grateful for my undergraduate students for allowing me to mentor them; Scott Call,

Dusty Johnston, Brett Mortensen, Josh Glatt, Andrew Curtis, Cole Miller, and David Collins.

To my mother, who passed away during this process, I am grateful for how she raised me and the love she showed. She always expressed amazement with anything I did and supported me and my family in all we ever did. To my father who is my friend, thank you for teaching me to work with my hands and to think for myself. To Mary Beth, thank you for being there for my dad and accepting my family as your own. To my brothers and sisters and my wife's family, thank you for your love and support.

To my children, thank you for your unconditional love for me, making me laugh, and bringing richer meaning to life. To my eternal companion, Jessica, thank you for giving me such wonderful children and for your love, support and encouragement to me. I could not have made it without you, this is all for you. Finally, I would like to thank the Lord, my savior, for making all things possible to me.

Jonny Price

CONTENTS

	Page
Abstract.....	iii
Public Abstract	v
Acknowledgements.....	vi
List Of Figures.....	x
Chapter 1 Introduction	1
References	6
Chapter 2 Rayleigh-Scatter Lidar Temperature Reduction Methods	8
Introduction	8
RSL Temperature Reduction	10
HC Method.....	11
HC Method Temperature Uncertainty.....	13
Optimal Estimation Method	16
OEM Error Analysis	23
References	26
Chapter 3 Comparison Of Rayleigh-Scatter Lidar Temperature Climatologies In The Mesosphere And Lower Thermosphere Between The Traditional Reduction Method And The New Optimal Estimation Method.....	29
Introduction	30
RSL Instrument.....	32
Climatology	34
Results.....	36
Original Lidar Results	36
Upgraded Lidar Results	43
Discussion/conclusions	47
References	49
Chapter 4 Obtaining Absolute Neutral Densities In The Mesosphere From Rayleigh-Scatter Lidar Using An Optimal Estimation Method	53
Introduction	54
Absolute Neutral Density Retrieval	55

OEM Density Retrieval	56
Reanalysis Model Densities	61
Comparison Results	65
High-Altitude Lidar Densities	69
Conclusions	71
References	73
Chapter 5 Absolute Neutral Density Climatology Over Utah State University From Rayleigh-Scatter Lidar Observations Using An Optimal Estimation Method	77
Introduction	78
Absolute Density Climatology	80
Original USU RSL System (1993-2004)	80
Upgraded USU RSL System (2014-2015)	83
Model Comparisons	86
Density and Temperature Climatology Comparison	90
Conclusions	92
References	93
Chapter 6 Tides In The Mesosphere Using Rayleigh-Scatter Lidar Temperature And Density Observations From July 20-24, 2003	96
Introduction	97
Classical tidal theory	98
Migrating and nonmigrating tides	103
USU RSL Tides	106
Conclusions:	111
References:	112
Chapter 7 Conclusions And Future Work	115
Summary and Conclusions	115
Future Work	118
References	119
Curriculum Vitae	121

LIST OF FIGURES

	Page
Figure 1.1: A model atmosphere showing the stratified atmosphere as defined by its thermal structure.	1
Figure 2.1: Block diagram of the current USU Rayleigh lidar.	9
Figure 2.2: Averaging kernels from OEM temperature reduction for February 25, 1995.	199
Figure 2.3: The averaging kernel matrix with the sum of the rows of the matrix (plotted in blue, orange and green).	211
Figure 2.4: Plot of the temperatures using different correlation lengths to generate the off-diagonal components for the a priori covariance.	22
Figure 2.5: Temperature uncertainty budget showing the uncertainties of each parameter used in the OEM temperature reduction.	24
Figure 2.6: Temperature uncertainties at different temporal resolutions for the nights of February 25, 1995 (left) and November 8, 2014 (right).	25
Figure 3.1: Chart showing the number of nights the RSL operated at USU.	333
Figure 3.2: Temperature climatology of USU RSL temperatures reduced using OEM... ..	366
Figure 3.3: Temperature climatology of USU RSL temperatures reduced by Herron and Wickwar (2018) using the HC method.	388
Figure 3.4: Plot showing the difference in temperature between OEM and HC.	399
Figure 3.5: Contour plots showing the change in temperature in the climatology with respect to the annual mean temperature.	411
Figure 3.6: Temperature climatology using the upgraded RSL at USU which operated between 2014 and 2015.	444
Figure 4.1: Uncertainty budget for the density reduction of RSL observations for the night of January 4, 1995.	59

Figure 4.2: Density percent uncertainties at different temporal resolutions for the nights of February 25, 1995 (left) and November 8, 2014 (right).	60
Figure 4.3a (top): Density profiles from OEM, MERRA-2 and MSIS2.0 for the night of September 9, 2002. Figure 4.3b (bottom): Percent difference of OEM and MERRA-2 with respect to MSIS2.0.	63
Figure 4.4a (top): Same as Figure 4.3a for May 5, 2001. Figure 4.4b (bottom): Same as Figure 4.3b for February 17, 1997.	64
Figure 4.5a (top): Absolute density values for each night of RSL-USU data at 45 km for OEM, MERRA-2 and MSIS2.0. Figure 4.5b (bottom): The percent difference between OEM and MERRA-2 with respect to MSIS2.0 at 45 km for each night of RSL-USU data.	66
Figure 4.6a (top): Samples of nighttime absolute density profiles from OEM, MERRA-2 and MSIS2.0 from each year of available data. Figure 4.6b (bottom): Samples showing the percent differences between OEM and MERRA-2 with respect to MSIS2.0 from each year of available data.	67
Figure 4.7: A contour plot of the log of density profiles for the night of November 8, 2014.	68
Figure 4.8: Contour plot showing the percent difference of the 15-minute density profiles minus the all-night average density profile.	69
Figure 4.9: Contour plot of the percent uncertainties of the absolute densities from November 8, 2014.	70
Figure 5.1: Annual density climatology, using OEM, showing the log of the densities using data from the original lidar (1993-2004).	79
Figure 5.2: Plot showing the annual percent difference in OEM density with the log of the densities superposed on top.	81
Figure 5.3: Density climatology showing the log of the densities from the upgraded lidar data (2014-2015).	82
Figure 5.4: Density climatologies from the upgraded lidar (2014-2015), left, and those from the original lidar (2003), right.	844
Figure 5.5: Same as Figure 5.2 but with the upgraded lidar densities.	855

Figure 5.6: Density climatologies from the MSIS2.0 empirical model, left, and from the original USU RSL observations normalized to MERRA-2 densities at 45 km.....	87
Figure 5 7: Plot of absolute neutral densities at 45 km from the OEM (blue), the MSIS2 model (orange), and the MERRA-2 model (green).....	88
Figure 5 8: Climatologies of the annual percent difference in densities (colored contours) and temperatures (solid and dashed lines) from the original USU RSL data (OEM), left, and from the MSIS2.0 empirical model, right.....	90
Figure 6.1: Plot of temperature profiles with 30-minute and with 1-km altitude resolution from the nights of July 20-24, 2003.....	105
Figure 6.2: Lomb-Scargle periodograms of the temperature (left) and density (right) from July 20-24, 2003 (62 hours total).	1077
Figure 6.3: Plot of the temperature (blue) and density (red) amplitudes of the first 5 harmonics of the diurnal tide (including the diurnal tide itself) from July 20-24, 2003.	1088
Figure 6.4: Frequency spectrum of temperatures (blue) and densities (orange) at 65 km.....	1099

CHAPTER 1
INTRODUCTION

Earth's atmosphere is one its most important features for fostering life on the planet. It acts as a blanket, trapping infrared radiation for heat while filtering higher energy radiation harmful to most living things. Because of its vital importance to life, the

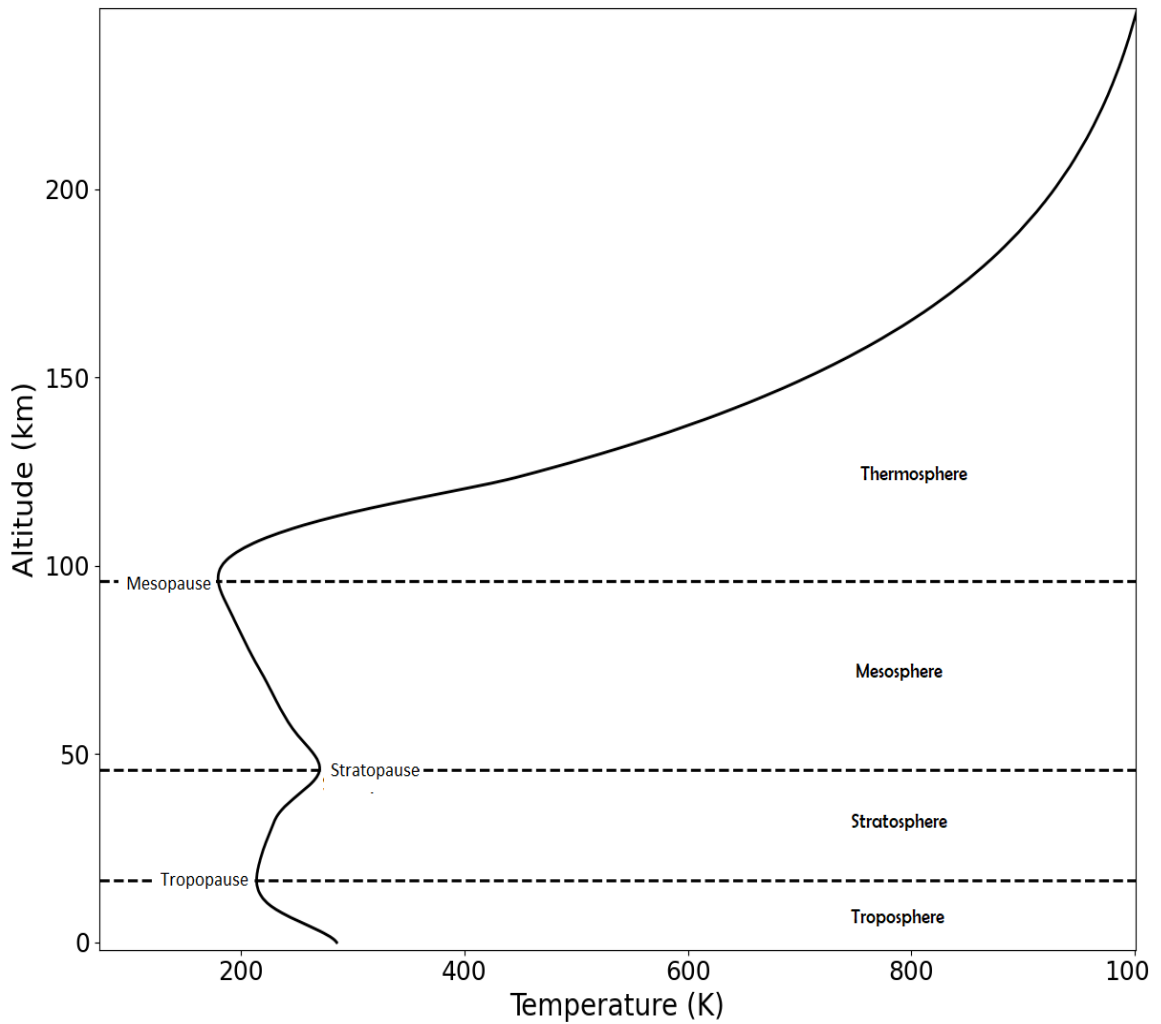


Figure 1.1: A model atmosphere showing the stratified atmosphere as defined by its thermal structure. The regions between, which contain the -pause suffix, are regions where the temperature gradient transitions occur.

study of the atmosphere from the ground to the edge of space can be considered extremely important. The atmosphere can be divided into strata defined by thermal, chemical or dynamical structure. The most common stratification definition is by thermal properties that divide layers by the sign of their temperature gradient. The names of the regions in this convention are the troposphere, stratosphere, mesosphere and thermosphere (Figure 1.1).

The troposphere extending from the ground to ~12 km is characterized by a negative temperature gradient. The neutral atmosphere consists mainly of N₂, O₂, and Ar with a significant presence of H₂O and CO₂. This is the region where life exists. Its upper limit coincides with the upper limit of commercial airlight. Because of the ease of access in this region, there are many instruments available for monitoring state variables such as temperature, density and pressure. The region where the temperature gradient changes from negative to positive is called the tropopause. The exact altitude of the transition regions in the atmosphere varies largely by latitude and time of year.

The stratosphere contains the ozone layer which absorbs ultraviolet radiation, protecting life below from its harmful effects. The absorption causes the neutral atmosphere to heat up and thus the stratosphere is characterized by a positive temperature gradient extending from the tropopause to ~50 km. Weather balloons are launched twice daily from approximately 800 locations around the world providing a good network of observations within this region up to just above 30 km. The region of temperature gradient transition from positive to negative at 50 km is the stratopause.

The mesosphere contains some of the coldest temperatures recorded on Earth and is considered the most difficult region to observe. Cooling by infrared emission, predominantly from CO₂, produces a negative temperature gradient, extending from the stratopause to ~90 km (Brasseur & Solomon, 2006). Large-amplitude oscillations, such as tides and gravity waves, which originate in the troposphere and stratosphere, caused by solar radiation absorption, propagate through the mesosphere and deposit energy and momentum in the upper mesosphere and lower thermosphere. The top region where the temperature gradient reverses again is called the mesopause. Above the mesopause is the thermosphere which contains aurora and artificial satellites. It is characterized by a large positive temperature gradient, with temperatures reaching as high as 2000 K.

The region from ~10 km to ~100 km is generally referred to as the middle atmosphere. Here, the composition of the neutral atmosphere remains consistent at roughly 78% N₂, 20% O₂, and 1% Ar with other trace elements present. Because of this homogeneity, the region, starting from the ground, is also known as the homosphere while above that it is known as the heterosphere. In this region the densities are low enough that turbulent mixing no longer dominates. In addition, photodissociation splits the O₂ to produce 2O, thus changing the composition of the neutral atmosphere. A study presented by Argall (2007) showed the effects of these compositional changes had on RSL temperature retrieval were small. Sox (2016) extended this study further, describing a difference in temperatures due to these effects in the 85-115 km region to be at most 2 K. She concluded that the temperature reduction equations were still valid

with minor modifications to account for the increase in atomic oxygen. The region where these conditions begin to appear is known as the turbopause, which occurs at around 100 km.

Various techniques are used with lidar, radar, optical and radiosonde equipment to study the middle atmosphere. Most techniques alone can only observe certain sections, or altitude ranges, of the middle atmosphere. Radar instruments are used mainly to observe winds and electron densities in the middle atmosphere between ~60 km to above 100 km. Radiosondes are typically launched aboard weather balloons twice daily from many locations around the world providing, among other variables, temperature, pressure and wind data up to around 30 km. USU houses a powerful AMTM, which is headed by Dr. Mike Taylor, that is used to observe the OH layer in the mesosphere which is used to obtain temperatures in a narrow region of the atmosphere. Lidar instruments can be used to observe aerosol properties, concentration of gases such as H₂O and O₃, and temperature and wind profiles using Mie-scatter, Raman-scatter, Rayleigh-scatter and resonance-scatter techniques. Of these techniques, Rayleigh-scatter lidar (RSL) is uniquely capable of observing an extended portion of the middle atmosphere from the upper stratosphere, through the mesosphere, and into the lower thermosphere, from around 30 km to above 115 km. The current observational capabilities of the RSL at Utah State University (USU) are to measure temperatures and densities over an altitude range from 40 km to above 115 km with planned improvements increasing the top of the range to above 125 km. More on the RSL system at USU will be discussed in Chapter 2.

A technique for reducing RSL observations, based on the lidar equation introduced in Chapter 2, to determine temperatures was presented by Hauchecorne and Chanin (1980) (referred to as the HC method) and has been widely used for over 30 years. Recently, a new method for reducing RSL observations was presented by Sica and Haefele (2015) that uses an optimal estimation method (OEM) to obtain temperatures. Both methods are detailed in Chapter 2. Advantages of the OEM over the HC method include a full uncertainty budget and a mathematically determined cutoff for the topmost valid altitude in the profile while maintaining consistency with HC derived temperatures at lower altitudes. This new method has now been used to obtain temperatures from the USU RSL. These results are presented in Chapter 3 through comparisons of the original temperature climatology presented by Herron (2007) and the new climatology using OEM temperatures.

Until recently, due to the small variability in atmospheric transmission and in laser power, only a relative scale for the neutral atmosphere density was produced from RSL observations. Efforts have been made to provide an absolute scale for densities through solving initial value problems (IVP) for the lidar equation, described in Chapter 2, (Mwangi et al., 2001) and by scaling the relative profile to a model-provided absolute density values at the altitude chosen to be unity in the normalized density profile (Barton et al., 2016; Wing et al., 2020). Drawbacks for both methods are their reliance on external data sources. The IVP method relies on an external source for temperatures, for which they use temperatures obtained from a collocated sodium lidar, which limits the results to an altitude range of between ~ 85 km and ~ 110 km. Using the scaling

technique produces its own challenges as it relies on model data to seed the density values within the entire profile and is limited in temporal resolution to that provided by the model.

Chapter 4 presents a new technique for producing absolute neutral densities by adapting the OEM presented in Chapter 2 to reduce RSL observations into densities rather than temperatures. This method includes the benefits outlined in the temperature retrieval as well as the capability of achieving finer temporal resolution. Chapter 5 presents composite climatologies of density profiles produced using the two USU RSL data sets, the original one and the newer, higher altitude one both of which are described in Chapter 3. Comparisons with densities seeded by reanalysis models are shown using the original data set comprising observations from 1993 through 2004. A case study of atmospheric tides using 5 nights of observations from July 2003, using both temperature and density profiles, is presented in Chapter 6. Conclusions and final thoughts on expanding on these studies are presented in Chapter 7.

References

- Argall, P. S. (2007). Upper altitude limit for Rayleigh lidar. *Annales Geophysicae*, 25(1), 19–25. <https://doi.org/10.5194/angeo-25-19-2007>
- Barton, D. L., Wickwar, V. B., Herron, J. P., Sox, L., & Navarro, L. A. (2016). Variations in Mesospheric Neutral Densities from Rayleigh Lidar Observations at Utah State

University. *EPJ Web of Conferences*, 119, 13006.

<https://doi.org/10.1051/epjconf/201611913006>

Brasseur, G. P., & Solomon, S. (2006). *Aeronomy of the middle atmosphere: Chemistry and physics of the stratosphere and mesosphere* (Vol. 32). Springer Science & Business Media.

Hauchecorne, A., & Chanin, M.-L. (1980). Density and temperature profiles obtained by lidar between 35 and 70 km. *Geophysical Research Letters*, 7(8), 565–568.

<https://doi.org/10.1029/GL007i008p00565>

Herron, J. P. (2007). *Rayleigh-Scatter Lidar Observations at USU's Atmospheric Lidar Observatory (Logan, UT) - Temperature Climatology, Temperature Comparisons with MSIS, and Noctilucent Clouds*. All Graduate Theses and Dissertations. Retrieved from <https://digitalcommons.usu.edu/etd/4686>

Mwangi, M., Sica, R., & Argall, P. (2001). Retrieval of molecular nitrogen and molecular oxygen densities in the upper mesosphere and lower thermosphere using ground-based lidar measurements. *Journal of Geophysical Research: Atmospheres*, 106(D10), 10313–10323.

Sica, R. J., & Haefele, A. (2015). Retrieval of temperature from a multiple-channel Rayleigh-scatter lidar using an optimal estimation method. *Applied Optics*, 54(8), 1872. <https://doi.org/10.1364/AO.54.001872>

Sox, L. (2016). *Rayleigh-Scatter Lidar Measurements of the Mesosphere and Thermosphere and their Connections to Sudden Stratospheric Warmings*. All Graduate Theses and Dissertations. Retrieved from <https://digitalcommons.usu.edu/etd/5227>

Wing, R., Martic, M., Hauchecorne, A., Porteneuve, J., Keckhut, P., Courcoux, Y., et al. (2020). Atmospheric Density and Temperature Vertical Profile Retrieval for Flight-Tests with a Rayleigh Lidar On-Board the French Advanced Test Range Ship Monge. *Atmosphere*, 11(1), 75. <https://doi.org/10.3390/atmos11010075>

CHAPTER 2

RAYLEIGH-SCATTER LIDAR TEMPERATURE REDUCTION METHODS

1. Introduction

Rayleigh scattering is the elastic scattering of electromagnetic radiation by particles whose diameter is much smaller than the wavelength of the radiation. This collision induces an oscillation of the particle at the same frequency as the incident radiation causing a photon to be emitted at the same wavelength. The scattering cross-section is proportional to the inverse of the wavelength to the fourth power ($\sim\lambda^{-4}$). Because of this, radiation with shorter wavelengths will scatter more strongly than radiation of longer wavelengths. This is the basic principle involved in Rayleigh-scatter lidar (RSL). A laser beam directed vertically into the atmosphere will interact with the neutral atmosphere causing scattering of light in all directions. A portion of this propagates back toward the telescope where it is focused onto a detector and stored into altitude bins over a set period of time.

The RSL receiver at Utah State University consists of four 1.25 m diameter mirrors operating together in a large housing and one separate 44 cm diameter mirror operating independently. Two lasers operating in tandem, providing more signal, directed vertically, parallel to the fields of view of the mirrors, are used to induce the scattering. The lasers are both high-powered Nd:YAG lasers from Spectra Physics with a fundamental wavelength of 1064 nm. Both lasers are frequency-doubled to generate a

beam at 532 nm producing a total power of 42 W at 30 Hz. Each mirror has a fiber optics cable at the focal point which directs the light to a series of lenses in the detector chamber to combine and focus the light from the four large mirrors. A mechanical chopper, placed at the focus, is used to block the high intensity light from below the

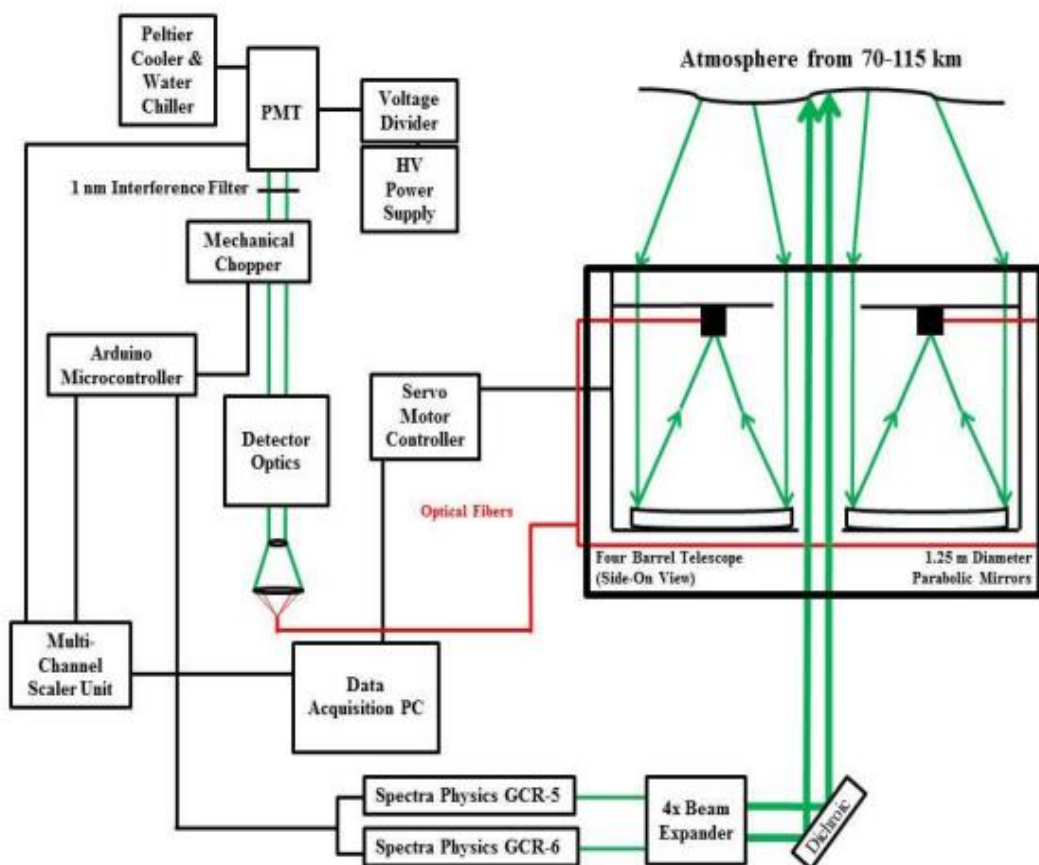


Figure 2. 1: Block diagram of the current USU Rayleigh lidar. From Sox (2016).

desired bottom altitude to prevent saturation of the detector. The light is then collimated and passed through a narrow band-pass interference filter and directed into the detector housing which holds a photomultiplier tube (PMT) from Electron Tubes. The detector housing is cooled to approximately -25°C with a combination of a Peltier

cooler and water cooled to 5° C. A multichannel scaler (MCS) is used to record the signal from the PMT, using an analog to digital converter, and save it into altitude bins with a 37.5 m resolution and integrate it over two minutes. (For more details on the USU system, see Herron, 2007; Sox, 2016; and Wickwar et al., 2001). An analogous system is used with the signal from the 44 cm mirror and the two resulting profiles are combined in the data reduction. The cross over from the low-altitude to the high-altitude signals is at approximately 70 km. The current capabilities of the USU RSL system, using the small and big telescopes, allow us to observe the middle atmosphere from 40 km to above 115 km. There are plans to further upgrade the system in 2021 with a higher efficiency PMT and higher transmittance interference filter for the high-altitude detection of the return signal to enable us to extend these altitude limits at least another 10 km.

2. RSL Temperature Reduction

As mentioned previously, the main method used for temperature reduction of RSL observations was first introduced by Hauchecorne and Chanin (1980) (herein referred to as the HC method). It combines the assumption of an ideal gas in hydrostatic equilibrium with the lidar equation to solve for the temperature using a seed temperature at the top altitude. More recently, a group at the University of Western Ontario (UWO) in London, Ontario, Canada have adapted a method widely used in the radiometry community to use for RSL temperature reduction (Sica & Haefele, 2015). This optimal estimation method (OEM) utilizes an optimization algorithm to obtain the

most likely temperature profile for a given RSL observed profile. It also uses the assumptions of an ideal gas and hydrostatic equilibrium combined with the lidar equation to produce temperature profiles. This new method, developed in MATLAB at UWO which implements the Qpack software package developed by Eriksson et al. (2005), was converted into Python and implemented at USU. The main benefits of using OEM, as outlined by Sica and Haefele, include a full uncertainty budget which provides uncertainties for each component of the lidar equation and a mathematically derived top-most valid altitude in the profile, with less dependence on a seed temperature at the top altitude. Both methods are outlined in this chapter.

2.1 HC Method

To extract temperature, we use the lidar equation to relate the relative neutral density in the atmosphere to the absolute temperature. The lidar equation itself relates the observed number of backscattered photons, $N(h)$, to the number of emitted photons, N_0 , the area, A , of the aperture, the atmospheric transmission, $\tau(h)$ which is squared due to the round trip of the emitted photons, the total efficiency of the receiver, Q , the Rayleigh cross section, σ_R , and the neutral number density, $n(h)$, at a given height above the detector h . The equation is expressed as

$$N(h) = \frac{N_0 A Q \tau^2(h)}{h^2} (n(h) \sigma_R). \quad (2.1)$$

We can then provide initial conditions at a given altitude, h_0 (in our case h_0 is the topmost altitude above sea level), using the MSIS2.0 model. This is then used to take the ratio of the atmospheric number density at two altitudes to find the relative density.

Doing this produces the equation

$$n(h) = n(h_0) \frac{N(h)h^2\tau^2(h_0)}{N(h_0)h_0^2\tau^2(h)}. \quad (2.2)$$

Hydrostatic equilibrium is the balance between the gravitational force and the pressure gradient,

$$\frac{dP(h)}{dh} = -n(h)m(h)g(h), \quad (2.3)$$

where $P(h)$ is the pressure, $m(h)$ is the mean molecular mass and $g(h)$ is the gravitational force, all at altitude h . We can obtain the temperature using the ideal gas law,

$$P(h) = n(h)kT(h) \quad (2.4)$$

where k is Boltzmann's constant, to replace the pressure term in 2.3. We then integrate over altitude from h to h_0 to get

$$k[n(h_0)T(h_0) - n(h)T(h)] = - \int_h^{h_0} n(h')m(h')g(h')dh'. \quad (2.5)$$

Here, $T(h_0)$ is the initial temperature at the top altitude in the profile and is obtained from an outside source such as the MSIS2.0 model. The top altitude is chosen by

determining the altitude where the signal is 16 times its standard deviation. . We can solve Equation 2.5 for the temperature at a given altitude, $T(h)$:

$$T(h) = T(h_0) \frac{n(h_0)}{n(h)} + \frac{1}{k} \frac{n(h_0)}{n(h)} \int_h^{h_0} \frac{n(h')}{n(h_0)} m(h') g(h') dh' . \quad (2.6)$$

Because of the dependence of the temperature on the ratio of two relative density measurements, the temperatures are absolute up to the initial value at the top altitude.

2.1.1 HC Method Temperature Uncertainty

The uncertainty for the photocounts follows Poisson statistics which relates the variance at each height to the photocounts at that height. Thus, the uncertainty in the photocounts is equal to the square root of the photocounts. The total photocounts include the return RSL backscatter signal and the noise. The noise, N , is due mainly to shot noise in the PMT and external light pollution from various sources such as moon light and scattered city lights. The noise is found by selecting a high-altitude region where no detectable backscattering occurs and taking the average value over the number of gates as the noise. The actual signal is found by separating out the noise, i.e., $S = (S + N) - N$ where $S + N$ is the observed signal, which includes the noise N .

To find the uncertainty in the signal we must include the background and account for any temporal and vertical averaging. The observed signal at time j becomes

$$S_j = \frac{1}{K} \sum_{k=1}^K (S + N)_{kj} - \frac{1}{L} \sum_{l=1}^L N_{lj} = \overline{(S + N)}_j - \bar{N}_j \quad (2.7)$$

where K is the number of altitude bins being averaged together, and L is the number of bins in the range chosen to produce the average noise count. The background variance can be represented by

$$d\bar{N}_j = \sum_{l=1}^L \frac{\partial N_j}{\partial N_{lj}} dN_{lj} = \frac{1}{L} \sum_{l=1}^L dN_{lj}. \quad (2.8)$$

The variation of $(S + N)_j$ with respect to $(S + N)_{kj}$ is given by

$$d(S + N)_j = \sum_{k=1}^K \frac{\partial (S + N)_j}{\partial (S + N)_{kj}} d(S + N)_{kj} = \frac{1}{K} \sum_{k=1}^K d(S + N)_{kj}. \quad (2.9)$$

Applying the convention where $\sigma_x^2 = (dx)^2$ to equations 2.8 and 2.9 and substituting into equation 2.7 gives

$$\sigma_{S_j}^2 = \sigma_{(S+N)_j}^2 + \sigma_{\bar{N}_j}^2 = \frac{1}{K^2} \sum_{k=1}^K \sigma_{(S+N)_{kj}}^2 + \frac{1}{L^2} \sum_{j=1}^J \sigma_{N_{lj}}^2. \quad (2.10)$$

Because the photocount profile follows Poisson statistics where $\sigma_x^2 = x$, the signal variance becomes

$$\sigma_{S_j}^2 = \frac{1}{K^2} \sum_{k=1}^K (S + N)_{kj} + \frac{1}{L^2} \sum_{l=1}^L N_{lj}. \quad (2.11)$$

When the vertical averaging is done on the right side of equation 2.11, it simplifies further to

$$\sigma_{S_j}^2 = \frac{1}{K} \langle S + N \rangle_j + \frac{1}{L} \langle N \rangle_j. \quad (2.12)$$

In similar fashion, multiple photocount profiles are averaged together for a vertically and temporally averaged signal resulting in the total variance (the square root of which is the standard deviation)

$$\sigma_S^2 = \frac{1}{JK} \langle \overline{S + N} \rangle + \frac{1}{JL} \langle \overline{N} \rangle. \quad (2.13)$$

The uncertainties in the signal are used to derive the uncertainty for the temperature profile. Using equation 2.6 we start with

$$dT = \frac{\partial T}{\partial T_0} dT_0 + \frac{\partial T}{\partial n_0} dn_0 + \frac{\partial T}{\partial n} dn, \quad (2.14)$$

where T_0 and n_0 denote the temperature and density respectively at the starting altitude h_0 . Performing the derivatives gives

$$dT = \frac{n_0}{n(h)} dT_0 + \frac{T_0}{n(h)} dn_0 - \left[\frac{T_0 n_0}{n(h)} + \frac{mg(h)}{kn(h)} \int_h^{h_0} n(h') dh' \right] \frac{dn}{n(h)} + \frac{mg(h)}{kn_0} \frac{\partial}{\partial n} \left[\int_h^{h_0} n(h') dh' \right] dn. \quad (2.15)$$

Now we let $c = mg/k$, $\partial/\partial n = d/dn$ and $dn = (dn/dh)dh$ with the relationship between density and a constant scale height, H , being

$$n(h) = n_0 e^{\frac{h_0-h}{H}}, \quad (2.16)$$

with $dn/dh = -(n/H)$. Substituting these terms into 2.15 simplifies to

$$\sigma_T^2 = \left[\frac{n_0}{n(h)} \right]^2 \sigma_{T_0}^2 + \left[\frac{T_0}{n(h)} \right]^2 \sigma_{n_0}^2 + \left[\frac{T(h)}{n(h)} \right]^2 \sigma_n^2. \quad (2.17)$$

Finally, substituting equation 2.16 into 2.17 we find the calculation of the temperature variance

$$\sigma_{T_h}^2 = T_h^2 \left(\frac{\sigma_n}{n} \right)^2 + \left[\sigma_{T_0}^2 + T_0^2 \left(\frac{\sigma_{n_0}}{n_0} \right)^2 \right] e^{\frac{-2(h_0-h)}{H}}. \quad (2.18)$$

The scale height for the neutral atmosphere, H , is assumed to be a constant 7 km. The uncertainty related to the initial temperature, the first term within the brackets, is often unknown and so is assumed to be zero. This approximation turns out to have little influence as it decreases rapidly with decreasing altitude, as does the second term inside the brackets.

2.2 Optimal Estimation Method

The OEM was first adapted for use with RSL observations to obtain temperatures by Sica and Haeferle (2015). The method was adapted from the work detailed by Rodgers (2000) and his earlier works (Rodgers, 1976; Rodgers 1990). Further work has been done by Jalali (2018) to reproduce temperature climatologies from the Purple Crow Lidar, in London Ontario Canada (PCL) observations using OEM and using the OEM to derive O_3 densities in the stratosphere. OEM iterates through the routine, making fine adjustments to the a priori temperature to find the optimal temperature which will coincide with a good fit of the RSL photocounts based on the forward model. The

treatment of the OEM derivation follows that of Sica and Haeefele (2015). The general form of the forward model \vec{F} is

$$\vec{y} = \vec{F}(\vec{x}, \vec{b}) + \epsilon, \quad (2.19)$$

where \vec{y} is the measurement vector, \vec{x} is the true state vector, \vec{b} contains the model parameters and ϵ is the measurement noise. The true state vector, \vec{x} , contains all parameters to be retrieved and the model parameters, \vec{b} , contain all other parameters needed to model the measurements. The forward model is derived from equation 2.1, with the ideal gas law substituting temperature and pressure in place of density. The state variables here include temperature and detector noise. The lidar equation depends on atmospheric properties and the system hardware configuration which are part of the model parameter vector.

Solutions for the state vector are found by minimizing a cost function. A cost function is used to measure the performance of the model in its ability to fit the observed data, with a value of one being a perfect match. The cost function is formed using Bayes' theorem using the instrument measurement, \vec{y} , the covariance of the measurement, \vec{S}_y , the forward model, the retrieved state parameters, the a priori, \vec{x}_a , and the a priori covariance, \vec{S}_a . The general form of the cost function is

$$cost = [\vec{y} - \vec{F}(\vec{x}, \vec{b})]^T \vec{S}_y^{-1} [\vec{y} - \vec{F}(\vec{x}, \vec{b})] + [\vec{x} + \vec{x}_a]^T \vec{S}_a^{-1} [\vec{x} - \vec{x}_a]. \quad (2.20)$$

The most likely state variable, or retrieval state \hat{x} , is produced when the cost function is sufficiently minimized and is given by

$$\hat{x} = \vec{x}_a + (\vec{K}^T \vec{S}_y^{-1} \vec{K} + \vec{S}_a^{-1})^{-1} \vec{K}^T \vec{S}_y^{-1} (\vec{y} - \vec{K} \vec{x}_a) = \vec{x}_a + \vec{G} (\vec{y} - \vec{K} \vec{x}_a). \quad (2.21)$$

Here, \vec{K} is the Jacobian matrix and \vec{G} is the gain matrix. The gain matrix demonstrates the sensitivity of the retrieval state vector to the measurement and is retrieved by

$$\vec{G} = \frac{\partial \hat{x}}{\partial \vec{y}} = (\vec{K}^T \vec{S}_y^{-1} \vec{K} + \vec{S}_a^{-1})^{-1} \vec{K}^T \vec{S}_y^{-1}. \quad (2.22)$$

The gain matrix is also used in the computation of the averaging kernel. The averaging kernel is a diagnostic tool that gives the sensitivity of the retrieved state to the measurements:

$$\vec{A} = \vec{G}_y \vec{K}_x. \quad (2.23)$$

Now we let $\vec{\epsilon} = \vec{y} - \vec{K} \vec{x}$ and apply this to equation 2.21 to get

$$\hat{x} = \vec{x}_a + \vec{A} (\vec{x} - \vec{x}_a) + \vec{G} \vec{\epsilon}. \quad (2.24)$$

Here we can see that if \vec{A} is unity at each altitude then \vec{x}_a drops out, leaving the retrieval only sensitive to the measurements with no influence from the a priori.

Altitudes where \vec{A} is less than unity have some amount of contribution from the a priori.

This can be visually represented by plotting the sum of each row of \vec{A} . Values of one indicate no a priori influence while values below one show what fraction of the return is based on the measurements versus the a priori. An example of this is found in Figure 2.2. We can also find the number of degrees of freedom in the retrieval state by taking the trace of \vec{A} . The number of degrees of freedom is associated with the number of valid bins in the retrieval. For example, if the number is 20 and we have an altitude resolution

of 2.5 km starting at 45 km, the topmost valid altitude in the retrieval is $20 \times 2.5 + 45 = 95$ km. We can also obtain the retrieved vertical resolution, or altitude resolution, by measuring the full width at half-maximum of \vec{A} at each altitude. The OEM itself uses the Marquardt-Levenberg method iteratively because the lidar temperature is nonlinear (Sica & Haeefe, 2015).

The forward model, $\vec{F}(\vec{x}, \vec{b})$, used is based on the lidar equation,

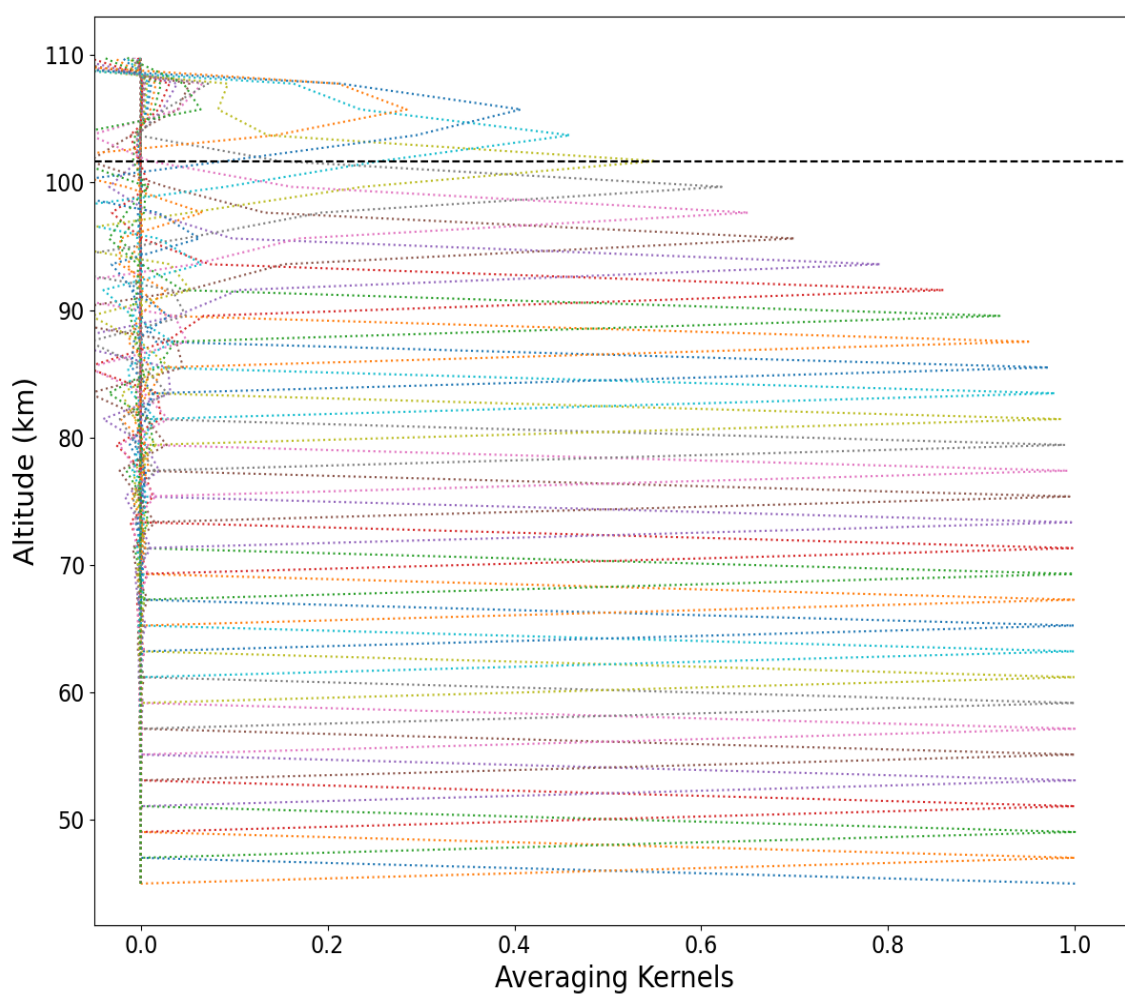


Figure 2. 2: Averaging kernels from OEM temperature reduction for February 25, 1995. The black dashed line shows the top altitude of the profile, determined by the number of degrees of freedom of the averaging kernel matrix.

$$N(h) = \frac{\psi(h)n(h)}{h^2} + B, \quad (2.25)$$

where B , which is retrieved with temperature, is the instrument noise and $\psi(h)$ is the instrument function:

$$\psi(h) = C\sigma_R(h)e^{-2\tau_{O_3}(h)}e^{-2\tau_R(h)}. \quad (2.26)$$

Here, C is the lidar constant, which is also retrieved and consists of the area of the receiver, the system efficiency, and the number of emitted photons; σ_R is the Rayleigh cross section; τ_{O_3} is the ozone optical depth at 532 nm; and τ_R is the optical depth due to Rayleigh extinction. The temperature reduction is equivalent to the HC method in that it uses the assumptions of the atmosphere as an ideal gas in hydrostatic equilibrium. With these assumptions we replace $n(h)$ using

$$n(h) = \frac{n_0 T_0}{T(h)} e^{-\int_h^{h_0} \frac{m(h')g(h')}{RT(h')} dh'}, \quad (2.27)$$

where R is the gas constant and T is the temperature which in the first iteration it is the a priori temperature. The mean molecular mass, m , is thought to be constant up to the point (~ 90 km) where photodissociation occurs causing O_2 to split into $2O$ and turbulent mixing loses dominance to chemical processes. The change in the composition of the neutral atmosphere is accounted for by estimating the mean molecular mass at each altitude bin using the MSIS2.0 model to retrieve the predicted Rayleigh cross-sectional density of each component at the given altitude (Argall, 2007; Sox, 2016). Equation 2.27 is a modified form from Sica and Haeferle (2015) who use pressure

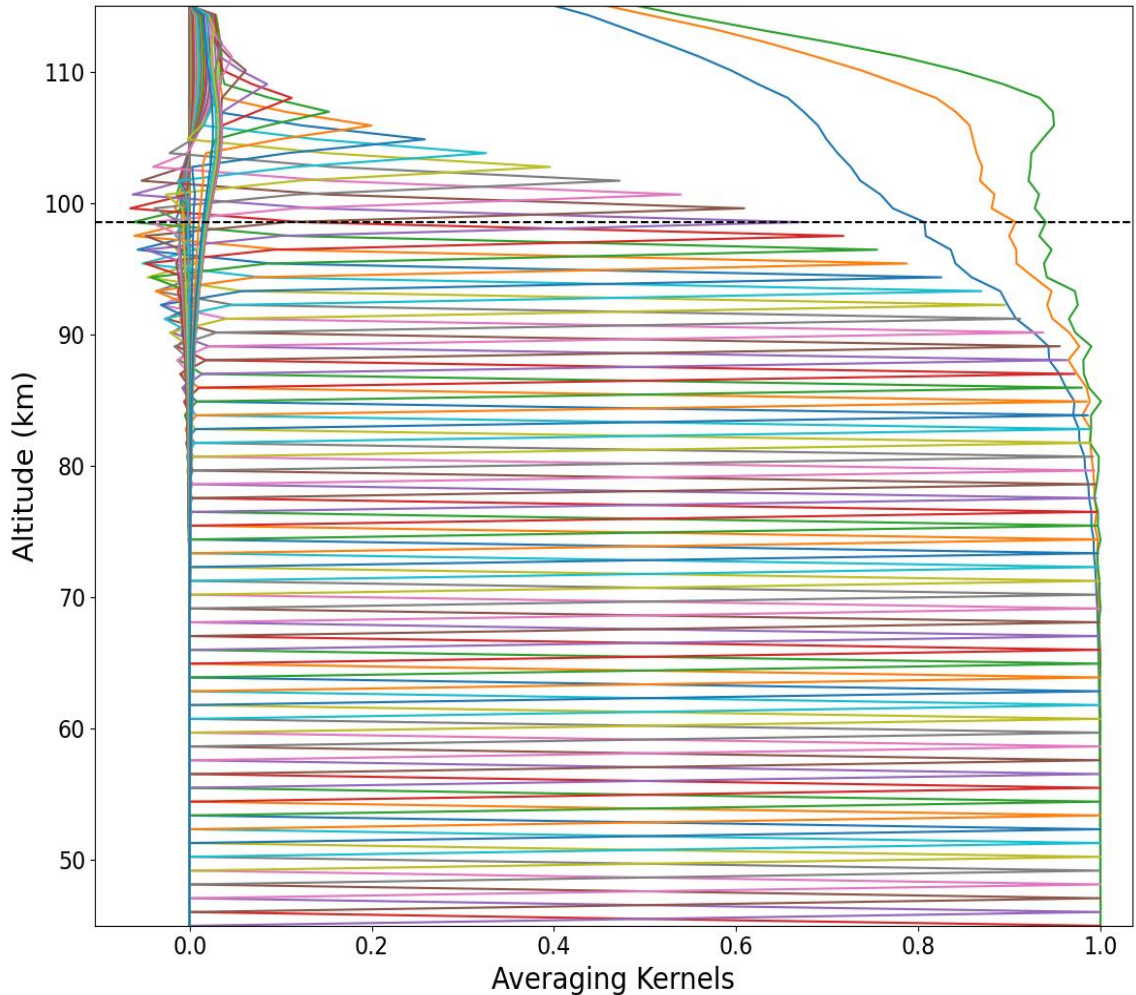


Figure 2. 3: The averaging kernel matrix with the sum of the rows of the matrix (plotted in blue, orange and green). The blue line shows the sum of the rows using a 1 km correlation length while the orange used a 2 km length and the green used a 3 km length.

instead of density for their temperature retrieval. Chapter 4 introduces the use of this method to obtain absolute neutral densities with the main difference from the temperature retrieval being that we do not need to substitute equation 2.26 into 2.25 to find solutions.

Here we need to discuss the importance of the covariances from the observation and from the a priori. The values at each altitude bin in the RSL signal is assumed to be

independent of values at other altitudes. As such, the signal covariance matrix, S_y , is a diagonal matrix (Sica & Haefele, 2015). The a priori covariance, however, should have off-diagonal elements (Eriksson et al., 2005). A correlation length appropriate to the desired retrieval altitude resolution is required to generate the off-diagonal components. This was done using a tent function to correlate off diagonal components. Different values for the correlation length were tested by adjusting the values and

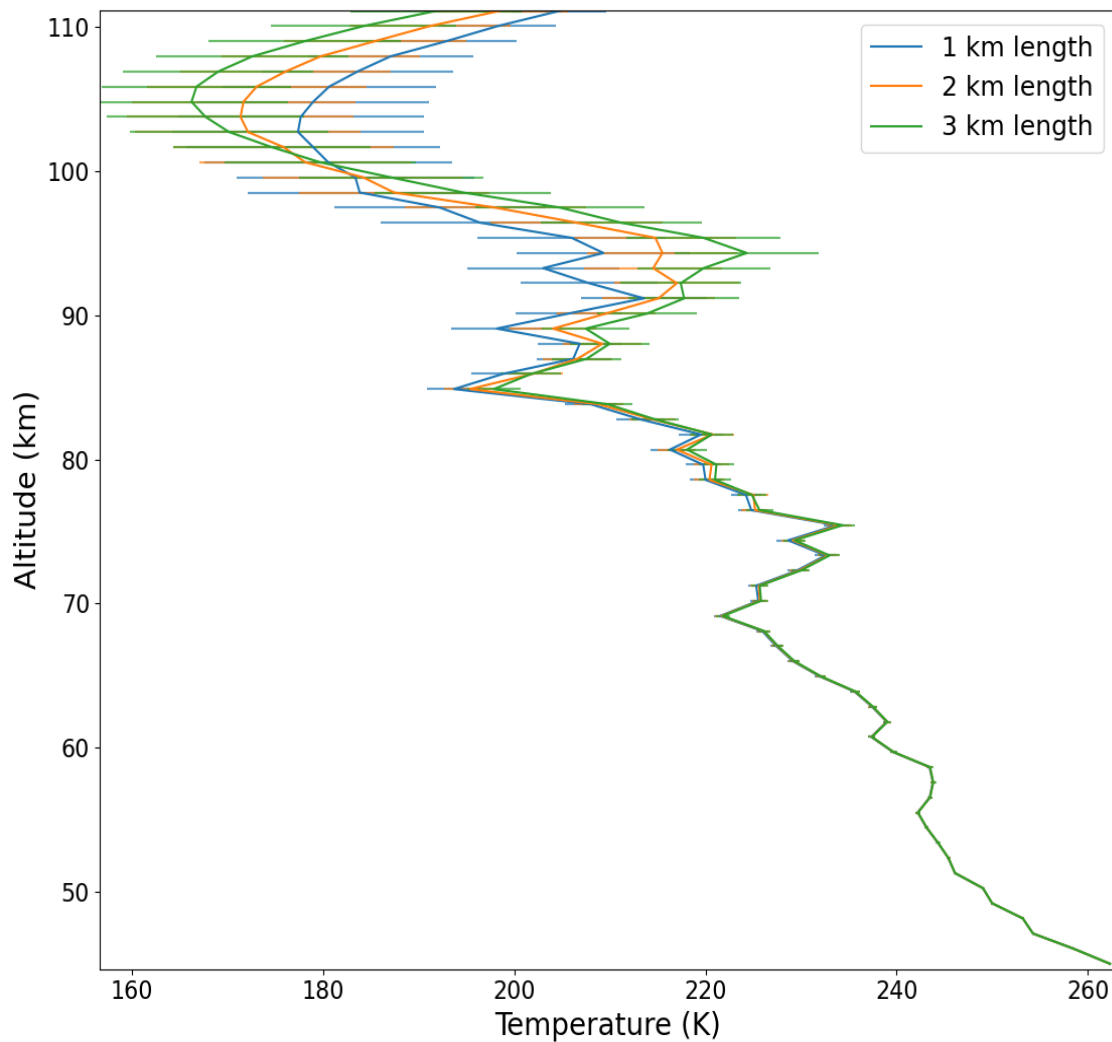


Figure 2.4: Plot of the temperatures using different correlation lengths to generate the off-diagonal components for the a priori covariance.

observing the effect on the averaging kernel. Figure 2.3 shows a plot of the sum of the rows in the averaging kernel for a sample night with a 1 km altitude resolution. The values tested for correlation length were 1 km, 2 km and 3 km. A length of 1 km demonstrated over constraint as the sum of the values drops below 1 more quickly, bringing in more a priori influence at lower altitudes. The 3 km length showed under constraint with some rows summing to greater than 1. The 2 km length appeared to show the proper amount of constraint with less influence from the a priori at lower altitudes while showing a gradual increase in a priori influence at higher altitudes. Thus, the correlation length used to produce off diagonal components was the desired altitude resolution plus 1 km. Figure 2.4 shows the direct impact of differing correlation lengths on the temperature profile.

2.2.1 OEM Error Analysis

A full uncertainty budget can be retrieved using the Jacobian matrix retrieved with the state variable. The covariance due to measurement noise, \vec{S}_m , is defined as

$$\vec{S}_m = \vec{G}_y \vec{S}_y \vec{G}_y^T. \quad (2.28)$$

The statistical covariance due to forward model parameters, \vec{S}_F , is given by

$$\vec{S}_F = \vec{G}_y \vec{K}_b \vec{S}_b \vec{K}_b^T \vec{G}_y^T, \quad (2.29)$$

where \vec{S}_b is the model parameter covariance, which includes the covariance of each parameter in the forward model, and \vec{K}_b is the Jacobian of those parameters. The total

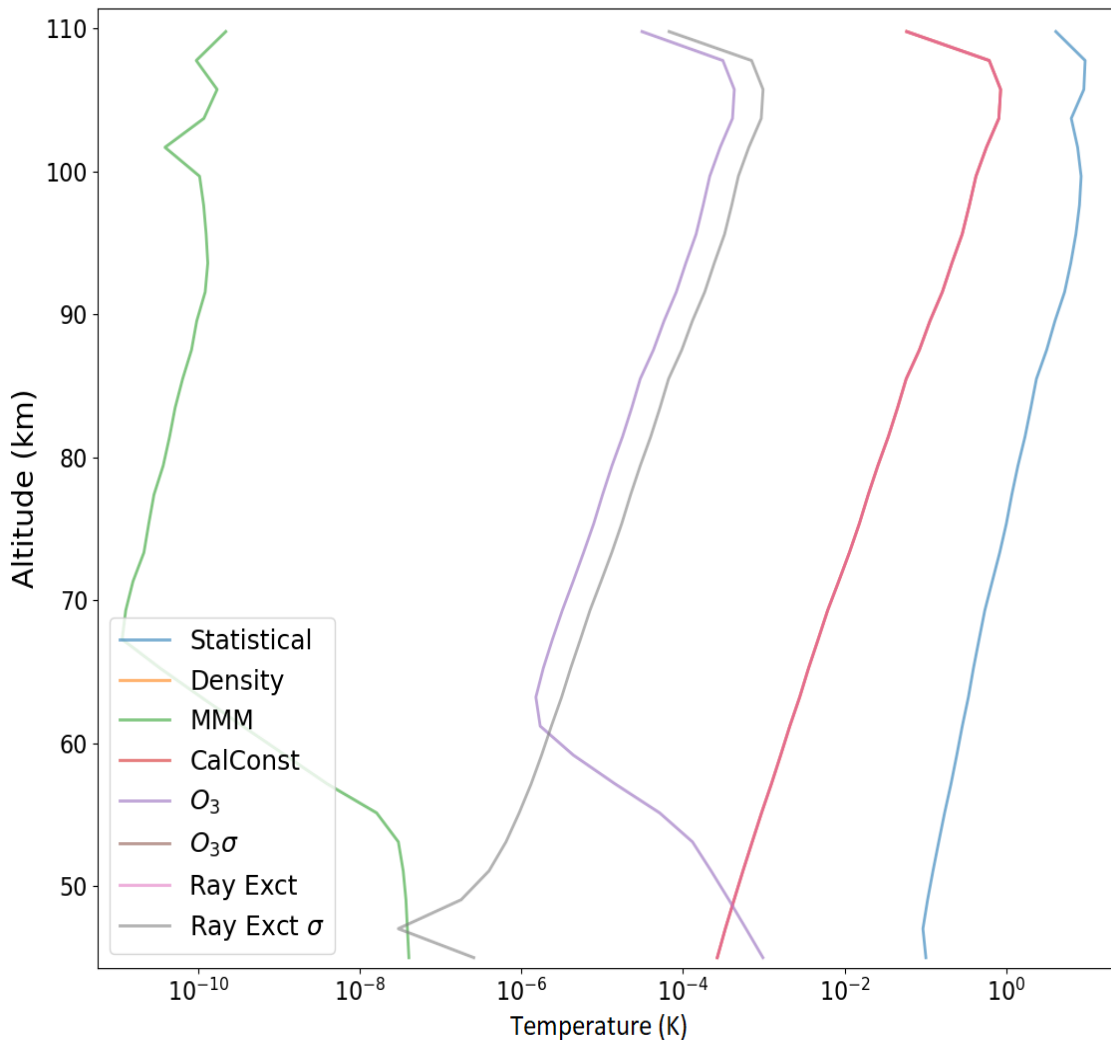


Figure 2.5: Temperature uncertainty budget showing the uncertainties of each parameter used in the OEM temperature reduction.

covariance is found from $\vec{S}_{total} = \vec{S}_m + \vec{S}_F$. The covariances for each model parameter, \vec{S}_p , are found by calculating the Jacobian matrix for each, \vec{K}_x , and using the retrieved

gain matrix along with the estimated uncertainty of the parameter. This is represented by

$$\vec{S}_p = \vec{G}_y \vec{K}_x \vec{S}_x \vec{K}_x^T \vec{G}_y^T. \quad (2.30)$$

An example plot of the temperature uncertainty budget is provided in Figure 2.5. Note that the major contributors to the total uncertainty are the statistical uncertainty and

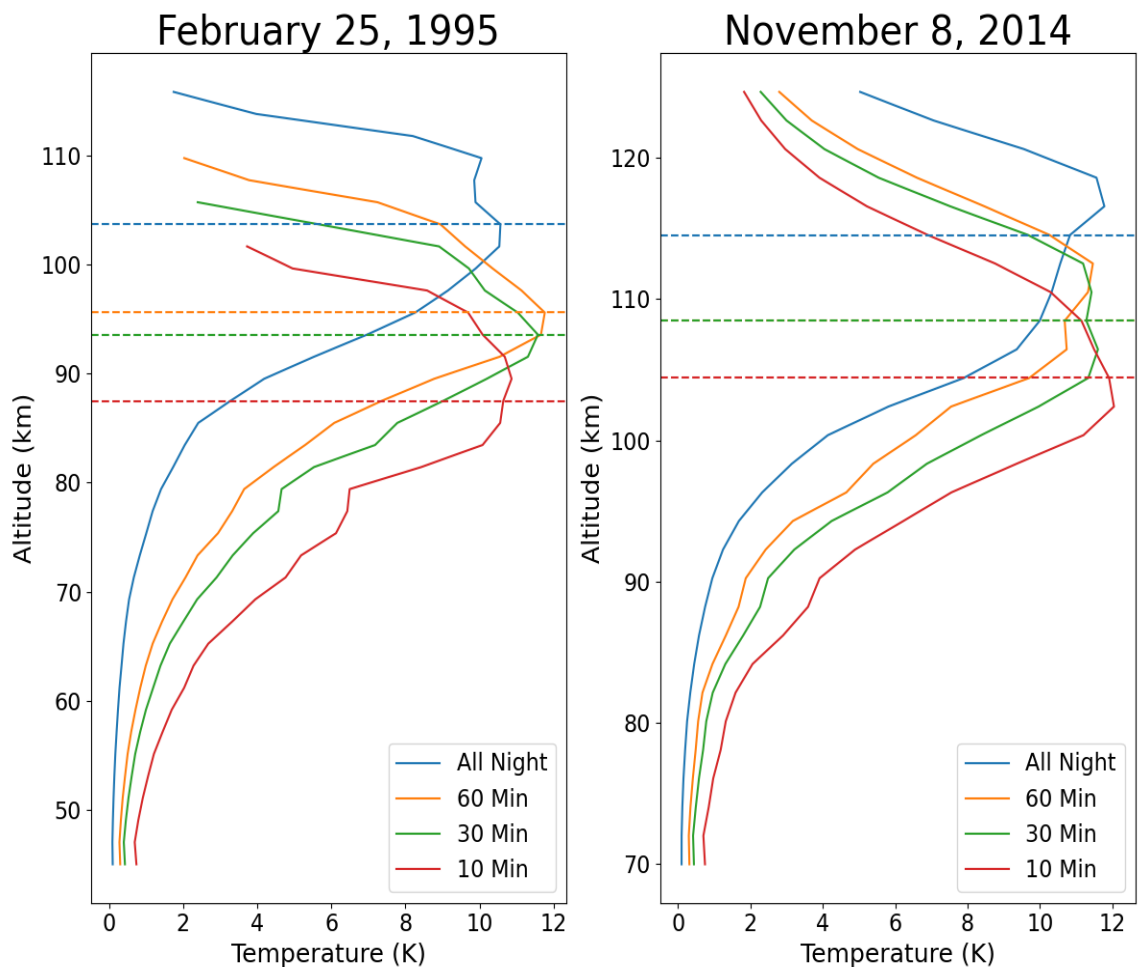


Figure 2.6: Temperature uncertainties at different temporal resolutions for the nights of February 25, 1995 (left) and November 8, 2014 (right). Here we see the uncertainties grow with finer temporal resolution along with lowering the top altitude (dashed lines with the 60 min and 30 min profiles in November having the same top altitude).

the uncertainty of the lidar constant with the rest having negligible impact on the total uncertainty.

The total OEM temperature uncertainty depends on the chosen temporal resolution. As an example of this, Figure 2.6 shows the total uncertainties for temporal resolutions of all night (9 hours for February 25 and 11.5 hours for November 8), 1-hour, 30-minutes and 10-minutes all with a 2 km altitude resolution using the original and upgraded lidar data. Here we see that, along with lowering the top altitude of the profile, the uncertainties increase starting at the lowest altitudes with finer temporal resolution. The changes in uncertainty, however, are relatively small with the maximum difference between the all-night uncertainties and the 10-minute uncertainties being around 8 K near the cutoff altitudes of the 10-minute profiles. Above the top altitude, the temperature uncertainties decrease rapidly as a result of the a priori taking over the returned profile.

References

- Argall, P. S. (2007). Upper altitude limit for Rayleigh lidar. *Annales Geophysicae*, 25(1), 19–25. <https://doi.org/10.5194/angeo-25-19-2007>
- Eriksson, P., Jiménez, C., & Buehler, S. A. (2005). Qpack, a general tool for instrument simulation and retrieval work. *Journal of Quantitative Spectroscopy and Radiative Transfer*, 91(1), 47–64.

- Hauchecorne, A., & Chanin, M.-L. (1980). Density and temperature profiles obtained by lidar between 35 and 70 km. *Geophysical Research Letters*, 7(8), 565–568.
<https://doi.org/10.1029/GL007i008p00565>
- Herron, J. P. (2007). *Rayleigh-Scatter Lidar Observations at USU's Atmospheric Lidar Observatory (Logan, UT) - Temperature Climatology, Temperature Comparisons with MSIS, and Noctilucent Clouds*. All Graduate Theses and Dissertations. Retrieved from <https://digitalcommons.usu.edu/etd/4686>
- Jalali, A. (2018). *Validating and Highlighting the Advantages of the Optimal Estimation Method For Rayleigh Lidar Middle Atmospheric Temperature Retrievals*. Electronic Thesis and Dissertation Repository. Retrieved from <https://ir.lib.uwo.ca/etd/5957>
- Rodgers, C. D. (1976). Retrieval of atmospheric temperature and composition from remote measurements of thermal radiation. *Reviews of Geophysics*, 14(4), 609–624.
- Rodgers, C. D. (1990). Characterization and error analysis of profiles retrieved from remote sounding measurements. *Journal of Geophysical Research: Atmospheres*, 95(D5), 5587–5595.
- Rodgers, C. D. (2000). *Inverse methods for atmospheric sounding: theory and practice* (Vol. 2). World scientific.
- Sica, R. J., & Haeferle, A. (2015). Retrieval of temperature from a multiple-channel Rayleigh-scatter lidar using an optimal estimation method. *Applied Optics*, 54(8), 1872. <https://doi.org/10.1364/AO.54.001872>
- Sox, L. (2016). *Rayleigh-Scatter Lidar Measurements of the Mesosphere and Thermosphere and their Connections to Sudden Stratospheric Warmings*. All Graduate Theses and Dissertations. Retrieved from <https://digitalcommons.usu.edu/etd/5227>

Wickwar, V. B., Wilkerson, T. D., Hammond, M., & Herron, J. P. (2001). Mesospheric temperature observations at the USU/CASS Atmospheric Lidar Observatory (ALO). In U. N. Singh, T. Itabe, & N. Sugimoto (Eds.) (p. 272). Presented at the Second International Asia-Pacific Symposium on Remote Sensing of the Atmosphere, Environment, and Space, Sendai, Japan. <https://doi.org/10.1117/12.417056>

CHAPTER 3

COMPARISON OF RAYLEIGH-SCATTER LIDAR TEMPERATURE CLIMATOLOGIES IN THE MESOSPHERE AND LOWER THERMOSPHERE BETWEEN THE TRADITIONAL REDUCTION METHOD AND THE NEW OPTIMAL ESTIMATION METHOD.

Abstract

An optimal estimation method (OEM) was used to obtain all-night temperature profiles from Rayleigh-scatter lidar (RSL) observations obtained by the original and updated lidar systems at Utah State University (USU). These data were used to produce annual climatologies of temperatures above USU. The climatology of temperatures from the original lidar, which operated from late 1993 through 2004, was compared with the climatology produced using the widely used Hauchecorne-Chanin method (HC). This comparison highlights the similarities at lower altitudes and differences, which start between 70 km and 80 km and extend to the top altitudes with the OEM temperatures warmer on average than those of the HC. The differences between methods are likely due to the reliance of the HC on a seeding temperature at the top altitude which likely has a large influence on the temperatures at the top 10 km. OEM and HC temperature climatologies were also produced using observations from the upgraded RSL at USU, which operated from early 2014 to early 2015. Like the original climatology, the newer climatology was seen to differ most at higher altitudes. The OEM climatologies from the original and newer data sets were compared, showing good agreement in the location

of the summer mesopause but with colder temperatures in this region from the newer observations.

1. Introduction

Rayleigh-scatter lidar (RSL) is an important tool for studying the middle atmosphere. It is uniquely capable of observing the upper portion of the stratosphere, the entirety of the mesosphere and the lower thermosphere with high temporal and height resolution. RSL has been used mainly in studying temperature characteristics in the middle atmosphere. Study topics have included atmospheric gravity waves (Hauchecorne et al., 1987; Kafle 2009; Sica & Argall, 2001), model validation (Ehard et al., 2018; Wing et al., 2018a, 2018b), and long-term temperature trends (Hauchecorne et al., 1991). A useful tool for studying annual temperature trends is by creating a temperature climatology (Argall & Sica, 2011; Herron, 2007; Herron & Wickwar, 2018; Jalali et al., 2018). An annual temperature climatology consists of averaging temperature profiles from each day, week or month over the entire data set. One such climatology was done by Herron (2007) (Herron & Wickwar, 2018) which used observation from over 900 nights of RSL data between late 1993 through 2004.

Hauchecorne and Chanin (1980) (HC) introduced a robust temperature retrieval method for the RSL observations. This widely used method uses a top down method integrating from the top altitude down, requiring an initial temperature at the top altitude. The lidar equation is utilized along with the assumptions that the atmosphere

consists of an ideal gas in hydrostatic equilibrium. Recently, a new method has been introduced which uses an optimal estimation method (OEM) to retrieve atmospheric temperatures. The method was developed by Rodgers (2000) for use in the radiometric community and applied to RSL temperature reduction by Sica and Haefle (2015). Some key improvements over the HC method include a robust uncertainty budget which provides uncertainties in instrument performance, atmospheric transmission, Rayleigh-scatter cross section along with statistical uncertainties and a well-defined limit for the topmost altitude in the temperature profile. Originally developed for use with the MATLAB scientific programming language, I have ported the OEM into Python and used it to reduce the USU RSL observations. The conversion to Python is based on the goal of providing an open-source version of the OEM which removes the reliance on expensive software subscriptions.

For comparisons with the HC results from Herron (2007), a new climatology was produced in the same manner using OEM temperatures reduced from the original USU RSL observations. Jalali et al. (2018) did a similar comparison between these methods using data from the Purple Crow lidar (PCL) at the University of Western Ontario, Canada (UWO), demonstrating good consistency with the HC method. Good agreement between the HC and OEM temperature climatologies using USU RSL observations, particularly for the first 40 km, was demonstrated in this study. A slight increase in the altitudes of the topmost valid temperatures was also demonstrated. In addition to the slight increase in altitude, the temperatures at the top altitudes are much less dependent on an a priori temperature value than in the HC method. An additional

temperature climatology using both OEM and HC methods consisting of observations made using the upgraded lidar system (Sox, 2016), which extends about 20 km higher, up to 115 km, is also presented.

2. RSL Instrument

The original RSL on the Utah State University campus (41.74° N, 111.81° W) operated from August 1993 through November 2004. During this period there were two Nd:YAG lasers used at different times. The initial setup used a 24-watt Spectra Physics laser operating at 532 nm at a 30 Hz repetition rate. It was later replaced with an 18-watt Spectra Physics laser operating at 532 nm at a 30 Hz repetition rate. The telescope receiver consisted of a single 44 cm diameter mirror which focused light through a field stop, limiting the field of view to 3 times that of the 1-mrad divergence of the laser beam. The light was focused onto the plane of a mechanical chopper to prevent oversaturating the PMT detector with very intense light from scattering at lower altitudes. The light was then collimated and passed through a narrow bandpass filter, which isolated light at the laser wavelength, and then passed to a Peltier cooled photomultiplier tube (PMT). The signal was converted from analog to digital using a converter then sent to a multichannel scaler and stored into altitude bins of 37.5 m (125 ns sampling) and integrated over two minutes. The effective range of observation was from 45 km to above 90 km when the signal was integrated over an entire night. More details on the system are given by Wickwar et al., (2001) and Herron, (2004).

By 2014, the lidar system had been significantly upgraded. The new system combined both the 18-watt and 24-watt lasers for a total power of 42 watts. The receiver system was upgraded to four coaligned 1.25 m diameter mirrors, providing an effective aperture area of 4.9 m². A 1.5 mm diameter fiber optic was placed at the focal point of each mirror. The light from the four mirrors was then combined, focused on the chopper plane, collimated and directed onto the PMT. The increased power and

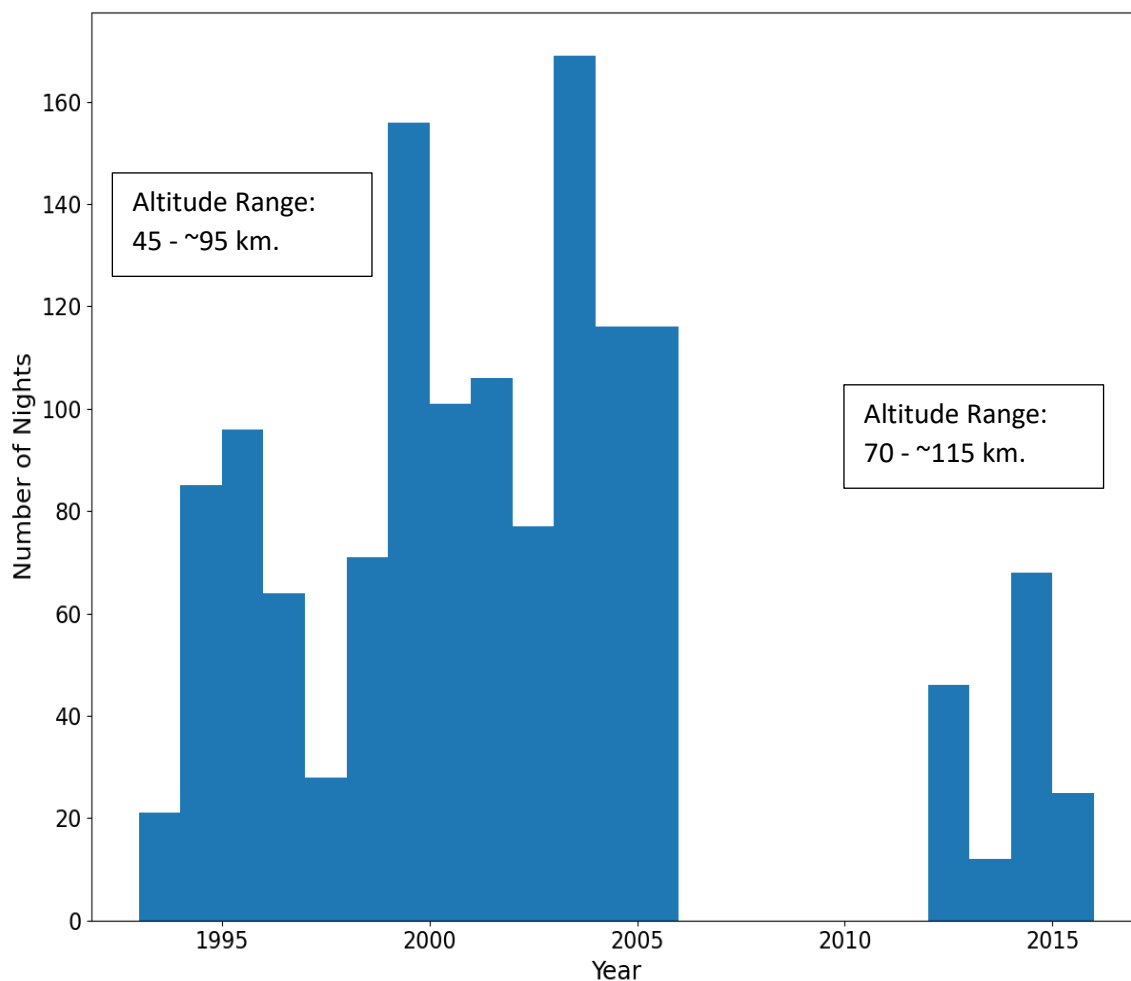


Figure 3. 1: Chart showing the number of nights the RSL operated at USU. The original lidar operated from 1993 through 2004. The upgraded system mainly operated during 2014 and 2015 with just over 50 nights of test data shown in 2012 and 2013.

aperture area extended the all night USU RSL observation range upward to ~ 115 km. The bottom of the valid altitude range was moved up to 70 km in order to prevent signal from lower altitudes saturating the detector, preventing us from detecting the faint signal at the topmost altitudes. Over 100 nights of observations were made between 2014 and 2015. Sox (2016) provides extensive details on the upgraded lidar system. Another upgrade repurposed the 44 cm diameter mirror and added another detector system, lowering the bottom altitude to 40 km while overlapping significantly with the signal from the 4-mirror telescope. This combined system showed that the range could be extended from 40 to 115 km. A future planned upgrade involving new detectors and interference filters should extend the top range upward to 125 km and lower the minimum range to 30 km. Figure 3.1 shows a chart of the number of nights of observation for each year of operation. The nights in 2012 and 2013 are early tests of the upgraded system, some of which are used in the data analysis herein.

3. Climatology

Creating a climatology of the temperature data is a technique used to model the expected behavior for the temperatures on a given day of the year. This provides a broad look at the quality of the data and a quick look at how the OEM compares with the HC method for temperature retrieval. It also provides a way to detect and compare individual profiles that differ significantly or demonstrate interesting behavior from the

composite model profile for that night. The original eleven-year data set, consisting of over 1000 nighttime observations, provides an excellent foundation for a climatology.

The composite year climatology of USU RSL temperatures using the OEM retrieval method is created in the same way as the HC based climatology of Herron and Wickwar (2018). The temperatures were first averaged by day of year over the eleven years. A running average was then performed for each composite day using a 31-day window with each day at the center to produce a composite day representing each day of the year. Before any averaging is performed, outliers within the data set are filtered from use if the profile differs by more than 3 standard deviations from a monthly mean profile. This is done to exclude extreme temperature profiles to create a more likely representation of a typical year. Out of the 1090 available profiles, ~200 profiles were excluded using this process. Many of these excluded profiles contain erroneous temperatures mainly due to instrument errors or poor weather conditions. Some are likely due to anomalous temperatures caused by unknown, but real, sources, such as on the night of February 20, 2004 (Bentley et al., 2018). While many of these profiles were deemed as 'bad' nights (Herron, 2007), not all should be labeled as such and merit further investigation as they could represent real anomalous atmospheric behavior. As the purpose of a climatology is to present more normal behavior, these nights have been left out.

4. Results

4.1 Original Lidar Results

Figure 3.2 shows the temperature climatology for a composite year using the OEM. The climatology consists of ~ 890 nights of temperature observations from USU extending from 45 km to about 100 km in some cases. The summer mesopause (starting

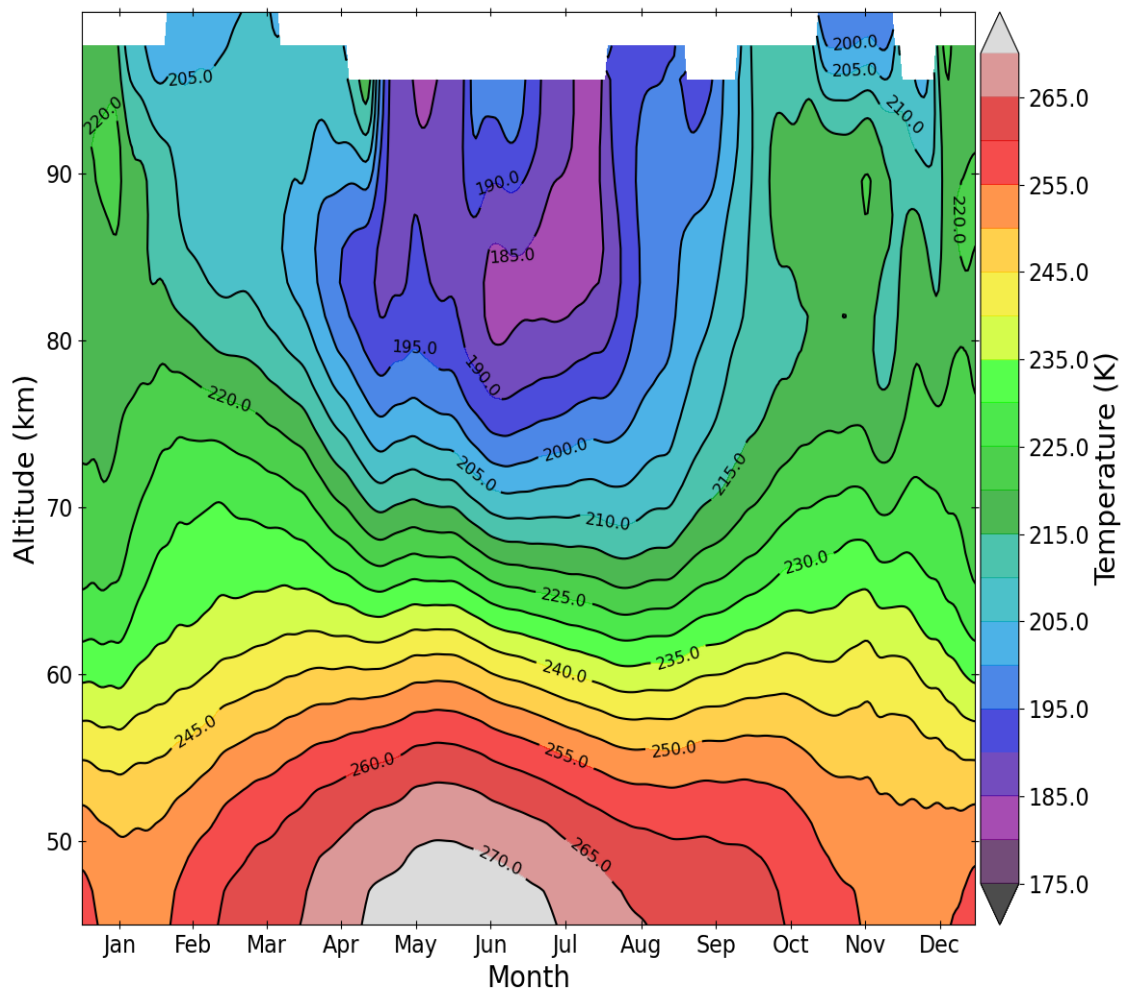


Figure 3.2: Temperature climatology of USU RSL temperatures reduced using OEM.

with the dark purple region), which contains the lowest temperatures in the mesopause, occurs from mid-April through mid-August, with the minimum temperatures (light purple region) occurring between mid-June through the end of July centered about roughly 83 km. Hints of lower temperatures in the spring and fall can be seen at the top altitudes. However, without being able to see higher we cannot say for sure where the winter mesopause is located. We can only say that we expect it to be above 100 km.

Large temperature gradients occur in the summer between 50 km and 80 km. This is due to the high altitude of the summer stratopause, which is the hottest region of the stratosphere located around 45 km, and low altitude of the summer mesopause being closer together in altitude during the summer causing a higher rate of change in the temperature in this range. The top of the summer stratopause can be seen around 45 km from April through mid-August (light pink). From winter to spring we see higher relative temperatures descend from ~90 km down to ~65 km from late-January until early March respectively. Later, from fall to winter we see higher relative temperatures ascending from ~55 km to ~87 km from mid-November until late-December respectively, with a low temperature trough creating a double peak appearance. Between these relative maxima we see a relative minimum occur in mid-January, most evident between 50 km and 70 km. Similar features were described by Herron and Wickwar (2018) which used the same data set but with the HC method to derive the temperatures. They also discuss the hotspot seen up to 50 km from late-December to early-January as a common feature among lidar groups and attribute the phenomena to

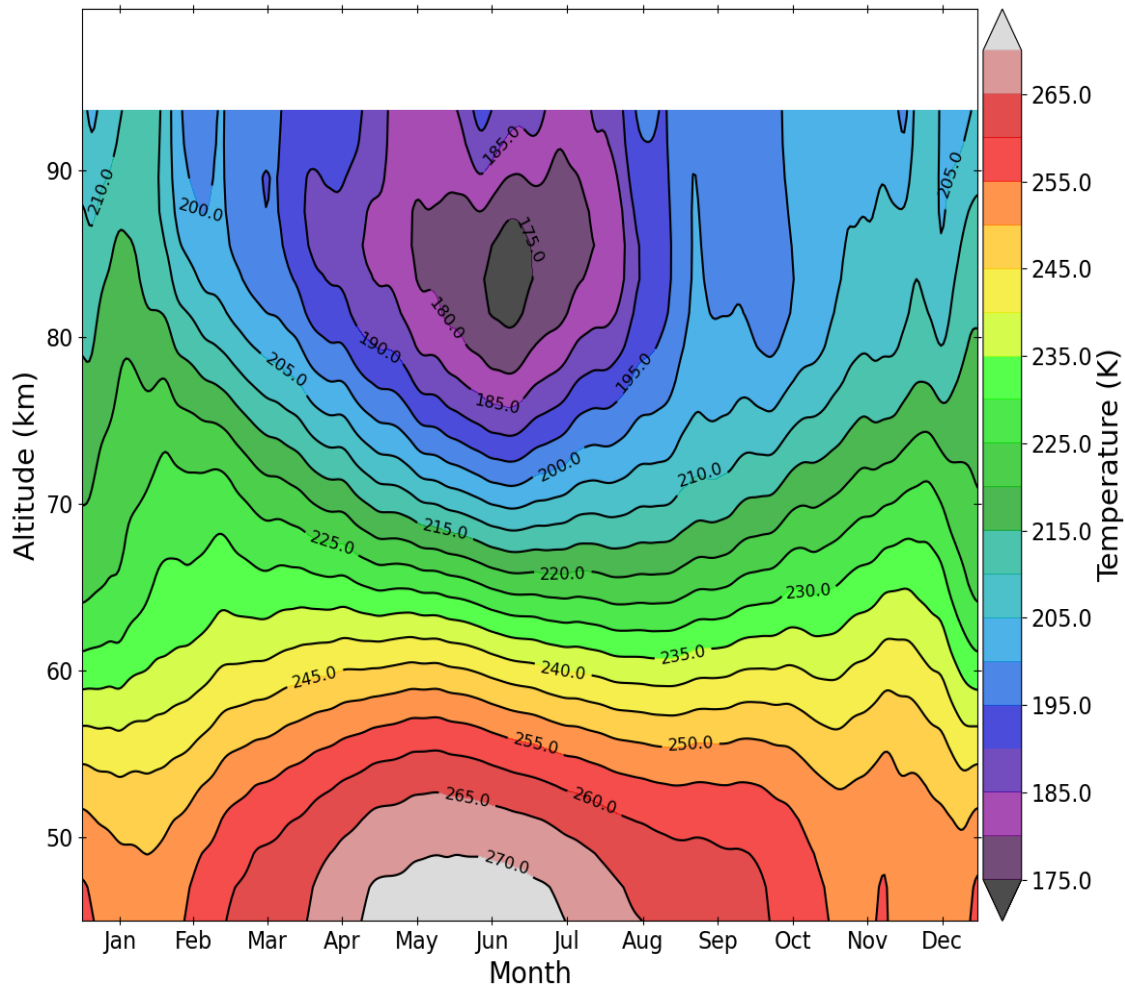


Figure 3.3: Temperature climatology of USU RSL temperatures reduced by Herron and Wickwar (2018) using the HC method.

Sudden Stratospheric Warmings (SSWs), pointing to a study of SSWs by Sox (2016) which also uses the USU RSL HC temperatures in the study.

Figure 3.3 shows the earlier climatology produced using temperatures reduced with the HC method for ~880 nights. The two temperature climatologies largely agree, with the summer mesopause (starting with the dark purple region) occurring around 83 km from mid-April through mid-August and the minimum temperatures centered

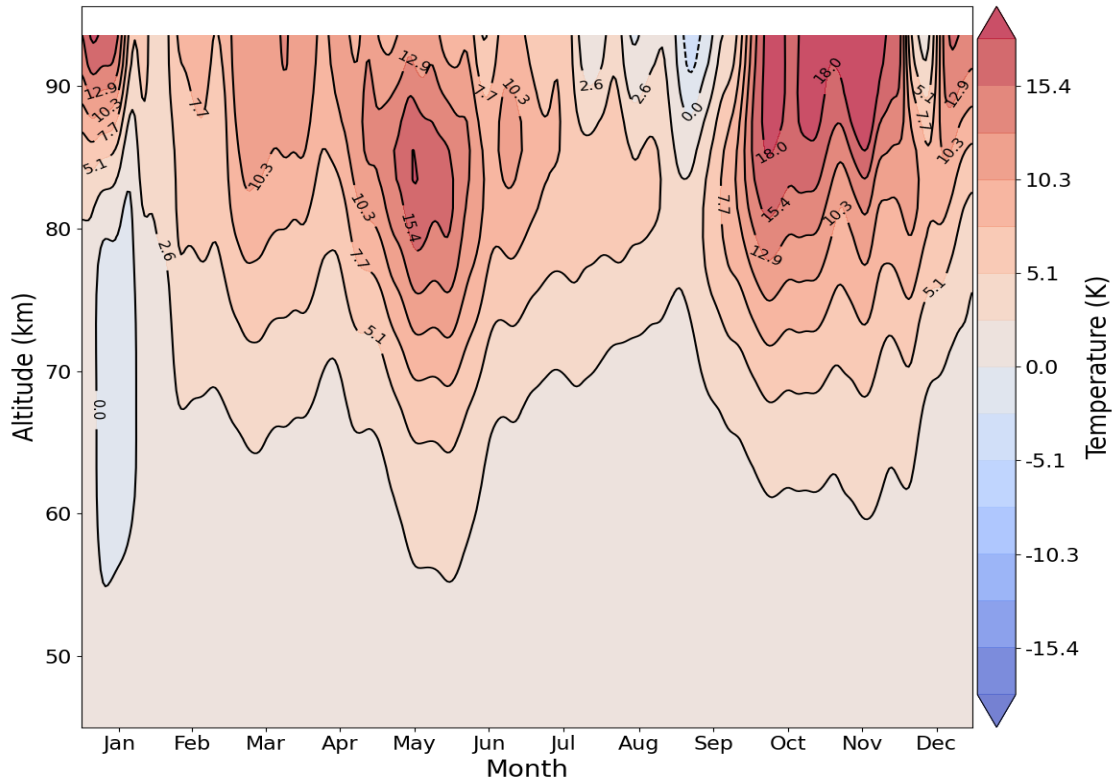


Figure 3.4: Plot showing the difference in temperature between OEM and HC. The overall positive temperature differences mean that the OEM temperature reduction produced higher temperatures overall than the HC temperature reduction, particularly above 70 km.

around mid- to late -June. The summer stratopause around 45 km shows the warmest temperatures between mid-April and mid-July in both images. Above 80 km, however, the temperatures are, on average, higher in the OEM climatology. Only minor differences are apparent at lower altitudes, which show similar features discussed by Herron and Wickwar (2018). The differences between the OEM and HC derived climatologies are plotted in Figure 3.4.

Figure 3.4 was made by subtracting the HC composite temperatures from the OEM composite temperatures. In this manner, the positive values denote higher OEM

temperatures while the negative values denote higher HC temperatures. From the comparison we see that, overall, the OEM temperature climatology shows higher temperatures than the HC climatology. Below 70 km, however, the temperature differences are small (under ~ 2 K). The largest differences occur above 85 km from mid-September through November. Because the top altitude of the HC temperature retrieval is obtained externally (from a model or other source), many RSL researchers remove the top 10 km altogether from the retrieval in order to remove the possible effect of the seed temperature (Argall & Sica, 2007; Jalali et al., 2018; Sica & Haefele, 2015). This does not necessarily mean we should ignore the top 10 km in the HC temperature climatology, but that it could be a source of error attributing to the differences between the HC method and OEM method temperatures at these altitudes. The OEM temperatures do not rely wholly on the a priori temperature and so the values, with their uncertainties, can be used with confidence throughout the valid profile (Jalali et al., 2018; Sica & Haefele, 2015).

To further examine the temperature variations, a climatology of the change in temperature with respect to the annual mean of the composite year was created using the OEM composite temperatures. For comparison, a similar climatology was created using temperatures from MSIS2. This model was chosen for the comparison because it uses vast amounts of observations from various ground-based and space-based detectors (Emmert et al., 2020) to generate the model temperatures above USU. It is also the model used to provide the a priori temperatures used in the OEM temperature reduction. Figure 3.5 shows how the OEM temperatures change with respect to the

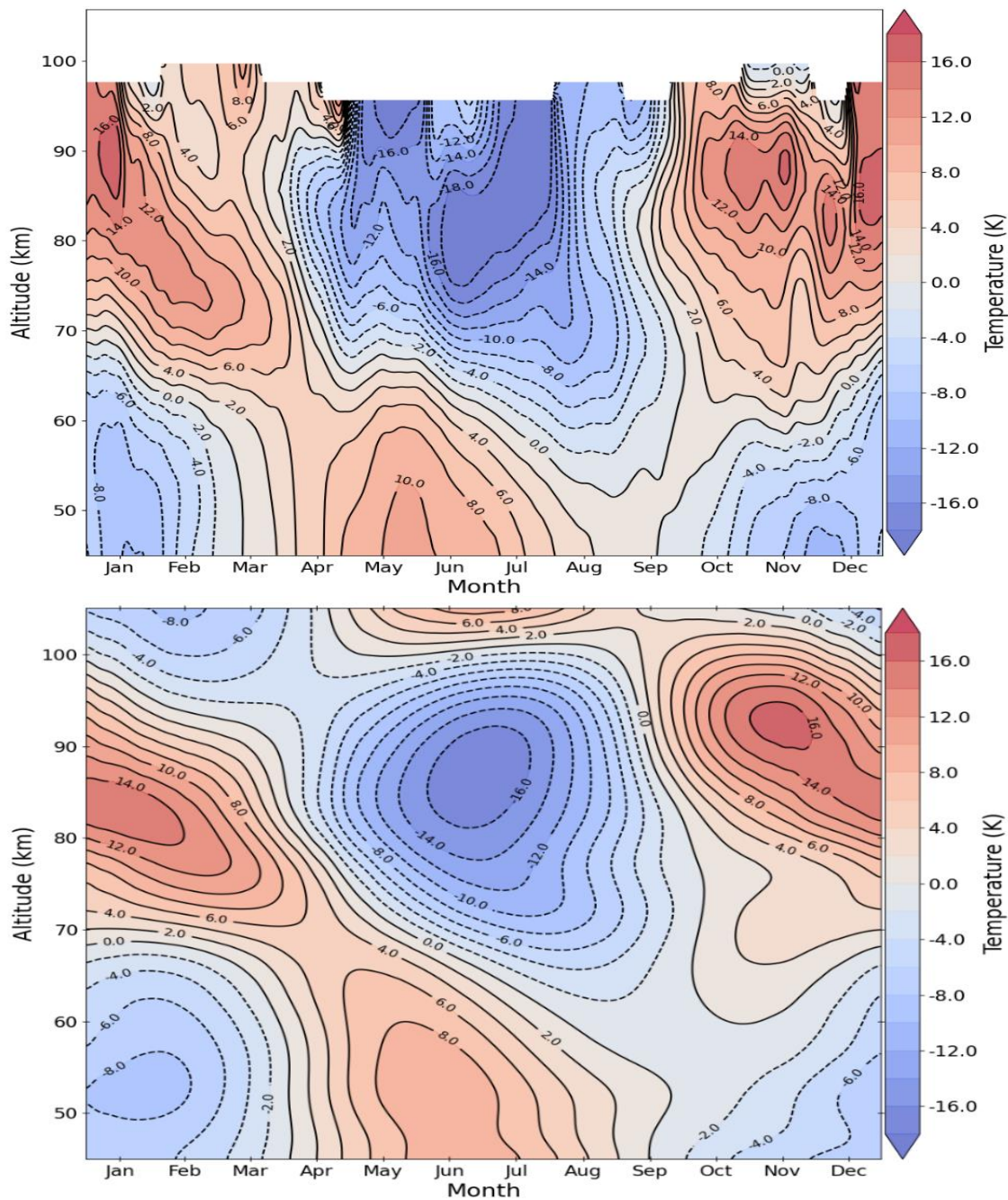


Figure 3.5: Contour plots showing the change in temperature in the climatology with respect to the annual mean temperature. Top: OEM temperature climatology. Bottom: MSIS2 temperature climatology.

OEM annual mean temperature (top) and how the MSIS2 model temperatures change with respect to the model annual mean temperature (bottom). Positive values indicate a

nighttime temperature which is hotter than the annual mean temperature.

The summer mesopause can be identified in both the OEM and MSIS2 climatologies centered around July. The altitude of the mesopause centers around 85 km in both climatologies. The winter mesopause cannot be determined from the OEM data because it does not go high enough, but we can start to see it in the MSIS2 data centered around February. We see similar features in both plots showing higher temperatures descending from mid-January until early- to mid-June. MSIS2 shows this descent starting in October, with the local maximum in early-November around 92 km, and descending all through the winter until April whereas OEM shows a lot more structure in between October and April with a local maxima occurring around 88 km in late-December and around 90 km in mid-January. Counting from January until mid-June, the rate of descent for the high temperatures within the OEM climatology is -9.8 km per month while the rate for the MSIS2 climatology is slower at -7.1 km per month. In both the OEM and MSIS2 plots we see a larger temperature gradient in the spring than in the fall below 60 km. The hot region in the summer below 50 km is centered around early-June in OEM but occurs ~15 days later in MSIS2.

At lower altitudes in Figure 3.5, we see a clear annual oscillation occurring in both OEM and MSIS2 plots with higher temperatures in summer and lower temperatures in winter below 60 km, the opposite being true between 70 km and 100 km. The OEM temperature difference climatology, however, shows higher order harmonics appearing above 70 km which are not apparent in the MSIS2 temperature

difference climatology. A likely cause for the lack of higher order harmonics is the large amount of data averaging within the model (Emmert et al., 2020).

4.2 Upgraded Lidar Results

Figure 3.6 shows the OEM and HC temperature climatologies using observations from the high altitude lidar system which consists of over 130 nights between 2014 and 2015. Due to the small number of nights in the data set, which do not quite cover an entire calendar year, this climatology is based on monthly averages instead of composite monthly averages about each night. Thus, because March and April do not have any data they are left blank. As with the lower altitude lidar temperature climatologies, these two plots show very similar temperatures, especially between May and November. The main differences occur, as with the low altitude temperatures, at the higher altitudes. In this case, they occur above 100 km. These differences occur mainly during the winter months and show a much higher temperature in the HC method. Large differences at high altitudes were also seen, and discussed, in the comparisons from the original lidar data. It is important to note that both the OEM and HC methods take account of the change in neutral atmosphere composition (Argall, 2007; Sox, 2016), which also affects the Rayleigh-scatter cross section. Accordingly, this is not a likely cause for the differences we see. The OEM climatology shows cold temperatures high in the wintertime that may be related to the winter mesopause. This

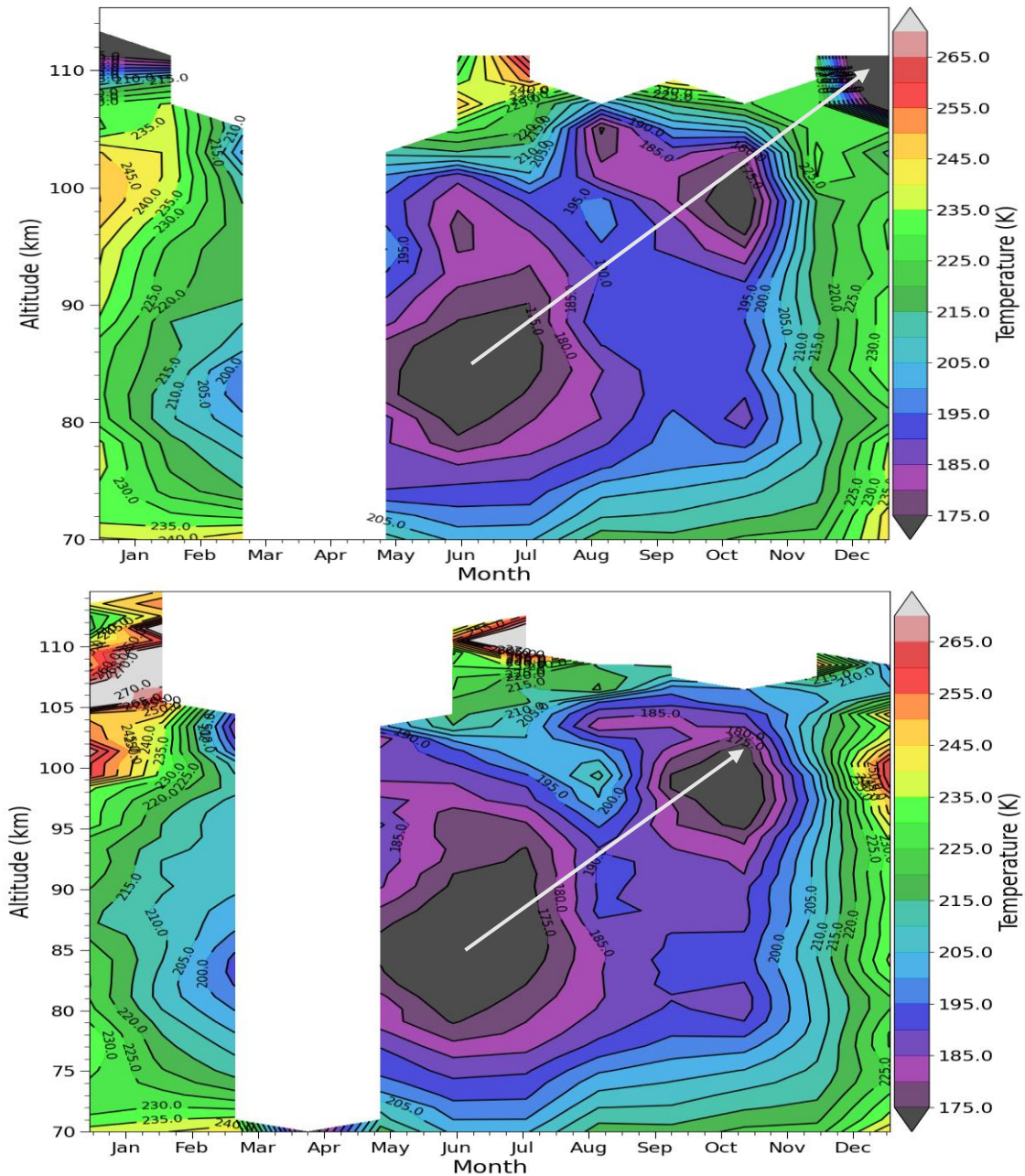


Figure 3.6: Temperature climatology using the upgraded RSL at USU which operated between 2014 and 2015. Top: OEM-reduced temperature climatology from data averaged by month. Bottom: Same as top but with HC-reduced temperatures. The white arrows show the ascent of the mesopause layer in altitude from summer to fall.

appears to be centered below 110 km, though due to insufficient nights of data we cannot define the mesopause for certain. Indeed in the HC plot there is no winter

mesopause apparent. More and better data, meaning higher signal to noise RSL observations collected as often as possible, are needed from the high altitude system to attempt a study of the winter mesopause.

The summer mesopause can be seen clearly in both the HC and OEM climatologies, with minimum temperature regions plotted in dark grey. This cold region is centered between May and August and is centered in altitude around 86 km in both plots. There is another large cold region centered at ~100 km and around mid-October, which can be seen in both plots as well. This region is likely the location of the mesopause during the fall of 2014. With this we can see that the low temperature mesopause region appears to ascend from summer to winter (highlighted by white arrow). We can see a hint of a cool region the OEM climatology of the original temperatures shown in Figure 3.2 between mid-October and December between 95 km and 100 km as well. However, because this is the top altitude limit of the original data set we cannot say for certain that these features are related or if a prominent fall mesopause would be present in other climatologies. More observations using the high-altitude lidar system is needed to confirm the existence of this fall feature.

Further comparisons between the OEM temperature climatologies from the original data and the newer data, Figure 3.2 and Figure 3.6 (top) respectively, we see some similarities in the overall climatology. However, the high altitude lidar temperatures show cooler temperatures in the summer mesopause than those of the low altitude lidar and warmer temperatures in January and December above 90 km. There are three main factors that might contribute to these differences. First, there is a

somewhat significant number of years between the observations taken from the old lidar system and the new lidar system. At a minimum there were 10 years and at a maximum 21 years. There have been studies that show climate change may have an impact on temperature and dynamics in the atmosphere, which would likely propagate upwards in a coupled atmosphere (Roble & Dickinson, 1989; Solomon et al., 2018; Thomas, 1996). Furthermore, the upgraded lidar operated over a single year of the solar cycle, whereas the original lidar operated over a full solar cycle. This means that the averages could reflect a different period of the solar cycle than the single year (Friis-Christensen & Lassen, 1990; Hathaway, 2015). This idea is explored further in Chapter 5. Second, because the newer lidar system is much more powerful (~57 times larger power aperture product) than the old. The regions of difference would have smaller uncertainties with the newer system than with the older system. However, the third point is that there are significantly more nights being averaged using the older lidar data, which lessens the impact a single profile has on the overall climatology and results in smaller uncertainties in each profile. Whatever the cause for the differences may be, the new lidar system will be able to address these issues better by covering a greater altitude range with the larger mirrors, two lasers, and more efficient detectors. It will be used at every opportunity to start building another dense data set like the original set.

5. Discussion/conclusions

The OEM temperature climatologies show good agreement with the HC temperature climatologies, but with notable differences. These differences occur mainly at higher altitudes suggesting there is a common issue behind these differences. Other RSL groups have addressed an issue with the HC method in its reliance on a seed temperature at the topmost altitude. Sica and Haefele (2015) and others (Sica & Argall, 2007; Jalali et al., 2018) have discussed the need to remove the top 10 km to 15 km from the analysis due to the uncertainties and unknown biases introduced into the temperature reduction by using the HC method. This would lower the original lidar temperatures to a max altitude of ~85 km, which is significant. As described in Chapter 2, the OEM provides an advantage over HC in that the top altitude is statistically determined using the averaging kernel matrix to determine the point at which the a priori temperature becomes significant. At this altitude, and beyond, all temperatures are determined to be due to the a priori value rather than the relation to the observed RSL data. Thus, the data under this altitude threshold is expected to be reliable. As such, these differences in analyses may prove to be the largest factor in the differences we are seeing between the OEM and HC temperature climatologies.

The location of the summer mesopause can be seen in both the old and newer climatologies to occur between 80 and 90 km centered around ~83 km in the old data and ~86 km in the newer data. We can see a secondary minimum temperature occurring during the fall in the newer lidar temperatures around 100 km. It is not clear if

this is a feature unique to 2014 or whether it is a third mesopause, a fall mesopause. However, it does appear to show the low temperature region of the summer mesopause ascend upwards towards the winter mesopause. The newer lidar data shows minima in the winter occurring at or above 110 km. Again, due to lack of data during the winter and with the newer data set in general it is unclear if these values are reliable or if they only reflect the winter mesopause of 2014-2015. Published estimates of the location of the winter mesopause put it around 105 km (She et al., 2000; She & von Zahn, 1998; von Zahn et al., 1996). If the winter mesopause was indeed around 110 km in 2014, it would indicate a much warmer winter mesosphere and may provide an interesting study into how tropospheric weather (affecting all life) is reflected in the mesospheric temperature behavior. With few instruments capable of observing this region of the mesosphere this may be challenging. However, a collaborative study with another lidar group such as the one at UWO might prove interesting. Another resource that may be useful is the possibility of comparisons with the SABER instrument aboard NASA's TIMED satellite, which has been operating since January 2002. With the additional upgrades coming shortly to the USU RSL shortly, we expect the range of operation to cover from below 40 km to above 120 km and hope to add to this study by providing another high-quality, dense data set.

References

- Ehard, B., Malardel, S., Dörnbrack, A., Kaifler, B., Kaifler, N., & Wedi, N. (2018). Comparing ECMWF high-resolution analyses with lidar temperature measurements in the middle atmosphere. *Quarterly Journal of the Royal Meteorological Society*, *144*(712), 633–640. <https://doi.org/10.1002/qj.3206>
- Emmert, J. T., Drob, D. P., Picone, J. M., Siskind, D. E., Jones, M., Mlynczak, M. G., et al. (2020). NRLMSIS 2.0: A whole-atmosphere empirical model of temperature and neutral species densities. *Earth and Space Science*. <https://doi.org/10.1029/2020EA001321>
- Friis-Christensen, E., & Lassen, K. (1990). Length of the Solar Cycle: An Indicator of Solar Activity Closely Associated with Climate. *Geol. Soc. Am. Bull*, *102*, 174.
- Hathaway, D. H. (2015). The Solar Cycle. *Living Reviews in Solar Physics*, *12*(1), 4. <https://doi.org/10.1007/lrsp-2015-4>
- Hauchecorne, A., & Chanin, M. L. (1980). Density and temperature profiles obtained by lidar between 35 and 70 km. *Geophysical Research Letters*, *7*(8), 565–568. <https://doi.org/10.1029/GL007i008p00565>
- Hauchecorne, A., Chanin, M. L., & Wilson, R. (1987). Mesospheric temperature inversion and gravity wave breaking. *Geophysical Research Letters*, *14*(9), 933–936. <https://doi.org/10.1029/GL014i009p00933>
- Hauchecorne, A., Chanin, M. L., & Keckhut, P. (1991). Climatology and trends of the middle atmospheric temperature (33–87 km) as seen by Rayleigh lidar over the south of France. *Journal of Geophysical Research*, *96*(D8), 15297. <https://doi.org/10.1029/91JD01213>

- Herron, J., & Wickwar, V. B. (2018). Mid-Latitude Climatologies of Mesospheric Temperature and Geophysical Temperature Variability Determined with the Rayleigh-Scatter Lidar at ALO-USU. *Journal of Geophysical Research*, 59.
- Herron, J. P. (2004). *MESOSPHERIC TEMPERATURE CLIMATOLOGY ABOVE UTAH STATE UNIVERSITY*. All Graduate Theses and Dissertations. Retrieved from <https://digitalcommons.usu.edu/etd/6877>
- Herron, J. P. (2007). *Rayleigh-Scatter Lidar Observations at USU's Atmospheric Lidar Observatory (Logan, UT) - Temperature Climatology, Temperature Comparisons with MSIS, and Noctilucent Clouds*. All Graduate Theses and Dissertations. Retrieved from <https://digitalcommons.usu.edu/etd/4686>
- Jalali, A., Sica, R. J., & Haeefe, A. (2018). Improvements to a long-term Rayleigh-scatter lidar temperature climatology by using an optimal estimation method. *Atmospheric Measurement Techniques*, 11(11), 6043–6058. <https://doi.org/10.5194/amt-11-6043-2018>
- Kafle, D. N. (2009). *Rayleigh-Lidar Observations of Mesospheric Gravity Wave Activity above Logan, Utah*. All Graduate Theses and Dissertations. Retrieved from <https://digitalcommons.usu.edu/etd/466>
- Roble, R. G., & Dickinson, R. E. (1989). How will changes in carbon dioxide and methane modify the mean structure of the mesosphere and thermosphere? *Geophysical Research Letters*, 16(12), 1441–1444. <https://doi.org/10.1029/GL016i012p01441>
- Rodgers, C. D. (2000). *Inverse methods for atmospheric sounding: theory and practice* (Vol. 2). World scientific.
- She, C. Y., & von Zahn, U. (1998). Concept of a two-level mesopause: Support through new lidar observations. *Journal of Geophysical Research: Atmospheres*, 103(D5), 5855–5863. <https://doi.org/10.1029/97JD03450>

- She, C. Y., Chen, S., Hu, Z., Sherman, J., Vance, J. D., Vasoli, V., et al. (2000). Eight-year climatology of nocturnal temperature and sodium density in the mesopause region (80 to 105 km) over Fort Collins, Co (41°N, 105°W). *Geophysical Research Letters*, 27(20), 3289–3292. <https://doi.org/10.1029/2000GL003825>
- Sica, R. J., & Argall, P. S. (2007). Seasonal and nightly variations of gravity-wave energy density in the middle atmosphere measured by the Purple Crow Lidar. *Annales Geophysicae*, 25(10), 2139–2145. <https://doi.org/10.5194/angeo-25-2139-2007>
- Sica, R. J., & Haefele, A. (2015). Retrieval of temperature from a multiple-channel Rayleigh-scatter lidar using an optimal estimation method. *Applied Optics*, 54(8), 1872. <https://doi.org/10.1364/AO.54.001872>
- Solomon, S. C., Liu, H., Marsh, D. R., McInerney, J. M., Qian, L., & Vitt, F. M. (2018). Whole Atmosphere Simulation of Anthropogenic Climate Change. *Geophysical Research Letters*, 45(3), 1567–1576. <https://doi.org/10.1002/2017GL076950>
- Sox, L. (2016). *Rayleigh-Scatter Lidar Measurements of the Mesosphere and Thermosphere and their Connections to Sudden Stratospheric Warmings*. All Graduate Theses and Dissertations. Retrieved from <https://digitalcommons.usu.edu/etd/5227>
- Thomas, G. E. (1996). Global change in the mesosphere-lower thermosphere region: has it already arrived? *Journal of Atmospheric and Terrestrial Physics*, 58(14), 1629–1656. [https://doi.org/10.1016/0021-9169\(96\)00008-6](https://doi.org/10.1016/0021-9169(96)00008-6)
- Wickwar, V. B., Wilkerson, T. D., Hammond, M., & Herron, J. P. (2001). Mesospheric temperature observations at the USU/CASS Atmospheric Lidar Observatory (ALO). In U. N. Singh, T. Itabe, & N. Sugimoto (Eds.) (p. 272). Presented at the Second International Asia-Pacific Symposium on Remote Sensing of the Atmosphere, Environment, and Space, Sendai, Japan. <https://doi.org/10.1117/12.417056>
- Wing, R., Hauchecorne, A., Keckhut, P., Godin-Beekmann, S., Khaykin, S., McCullough, E. M., et al. (2018a). Lidar temperature series in the middle atmosphere as a

reference data set – Part 1: Improved retrievals and a 20-year cross-validation of two co-located French lidars. *Atmospheric Measurement Techniques*, 11(10), 5531–5547. <https://doi.org/10.5194/amt-11-5531-2018>

Wing, R., Hauchecorne, A., Keckhut, P., Godin-Beekmann, S., Khaykin, S., & McCullough, E. M. (2018b). Lidar temperature series in the middle atmosphere as a reference data set – Part 2: Assessment of temperature observations from MLS/Aura and SABER/TIMED satellites. *Atmospheric Measurement Techniques*, 11(12), 6703–6717. <https://doi.org/10.5194/amt-11-6703-2018>

von Zahn, U., Höffner, J., Eska, V., & Alpers, M. (1996). The mesopause altitude: Only two distinctive levels worldwide? *Geophysical Research Letters*, 23(22), 3231–3234. <https://doi.org/10.1029/96GL03041>

CHAPTER 4

OBTAINING ABSOLUTE NEUTRAL DENSITIES IN THE MESOSPHERE FROM RAYLEIGH-SCATTER LIDAR USING AN OPTIMAL ESTIMATION METHOD

Abstract

Observations of absolute neutral densities in the mesosphere and lower thermosphere (MLT) have been difficult to obtain. Direct observations using sounding rockets are expensive and infrequent. Passive observation methods have previously been unable to derive neutral densities directly. To a limited extent, the backscattered signal from Rayleigh-scatter lidar (RSL) has been used, but it is affected by laser power, atmospheric transmission, and composition. We have developed a more effective approach to this problem utilizing an optimal estimation method (OEM). The method is explained, and the resultant OEM density profiles are compared to profiles based on the lidar signal normalized to densities from the MERRA-2 reanalysis model and to the independent, empirical MSIS2.0 model densities. Results show MERRA-2 densities consistently larger than OEM but with similar structure in the density profiles. Due to height and temporal limitations in reanalysis models, seeding densities for systems which begin observations above the upper limits of the model, or which require finer temporal resolution, are impractical. We demonstrate the OEM's capability of retrieving densities from RSL observations starting at 70 km and with 15-minute resolution.

1. Introduction

Measurements of the absolute neutral density in the mesosphere and lower thermosphere (MLT) are difficult to make, only relatively few instruments are capable of making density observations in this significant region of the atmosphere. Rocket sounding observations are capable of direct measurements of temperature and density but are used infrequently because of high cost and logistical complications. Direct measurements from weather balloons are impossible in this region as they can only observe to just above 30 km before the balloon breaks. Passive instruments from the ground and aboard satellites are most commonly used to observe this region. Passive instruments rely on observations of energetic reactions either from solar absorption or external stimuli. Satellites can provide a global view of atmospheric state variables but are limited in temporal resolution for any given location because of their orbital motion. Rayleigh-scatter lidars (RSLs) are the only ground-based instruments capable of making regular night-time observations of the entire MLT. A study by Mwangi et al. (2001) provides a method for estimating the densities of N_2 , O_2 , and O . However, their method relies on temperature measurements from an independent source, such as a collocated sodium lidar, to solve initial value problems for the lidar equation. In this study, we have implemented an optimal estimation method (OEM) for estimating the absolute neutral density that does not rely on temperatures and that minimizes the influence of a priori values.

An OEM for obtaining temperatures from RSL observations was implemented by Sica and Haeferle (2015). It provides a complete uncertainty budget and a derived cut-off height for retrievals while maintaining consistency with the currently used method introduced by Hauchecorne and Chanin (1980) (HC method). Here we adapted the OEM to retrieve the absolute neutral densities throughout the mesosphere using RSL observations above the atmospheric lidar observatory at Utah State University (ALO-USU) in Logan, UT (41.74° N, 111.81° W). The resulting densities are compared to model densities using MSIS2.0 (Picone et al., 2002) and to densities obtained from RSL data with a conventional method using the MERRA-2 reanalysis model (Bosilovich et al., 2015; Koster et al., 2016; Rienecker et al., 2011) for normalization at 45 km. An example of the conventional method is given by Barton et al. (2016). While reanalysis models provide useful data that are grounded in observations, they do not extend in altitude past ~ 65 km. This limitation prevents the use of reanalysis models to scale RSL densities whose lower altitude boundary is above 65 km, such as that of the upgraded ALO-USU RSL. To further demonstrate the capabilities of OEM, data from the large aperture lidar at ALO-USU is used to produce densities at a finer altitude resolution with 15-minute integrations.

2. Absolute Neutral Density Retrieval

The original atmospheric lidar observatory at USU (ALO-USU) operated from 1993 until 2004. It consisted of a 44 cm diameter mirror with a 532 nm Nd:YAG laser

producing a power-aperture product (PAP) of 2.74 Wm^2 to 3.65 Wm^2 depending on laser power (18 W or 24 W at 30 Hz). Nighttime observations were obtained in the mesosphere from 45 km to ~ 95 km with a 37.5 m resolution integrated over 2 minutes. This data set consists of over 950 good nights amounting to more than 5900 hours of observation. The system was overhauled and made operational again in 2014. The upgrades to the system, including four 1.25 m mirrors and using both the 18 W and 24 W lasers, increased the PAP to 206 Wm^2 and the altitude range to between 70 km and above 115 km. Over 90 nights of observations were made with this system between 2014 and mid-2015. Still more recently the 44 cm mirror was repurposed with a second detector system to regain the lower altitudes so that the total altitude range is between 40 km and above 115 km. More details regarding the RSL-USU can be found in Herron (2007), Sox (2016) and Wickwar et al. (2001).

2.1 OEM Density Retrieval

The OEM was developed for use in remote sensing by Rodgers (2000) and is widely used as a retrieval method in passive remote sensing. (Haeferle et al., 2009; Palmer & Barnett, 2001; Watts et al., 2011). The OEM method for obtaining MLT neutral densities follows the work by Sica and Haeferle (2015), where they describe in detail the OEM method for obtaining temperatures from RSL observations, differing only in the state vector and forward model used. The core of OEM is the forward model (given by

equation 4.1) describing the lidar measurements as a function of state and model parameters. The general form for the forward model is written as

$$\vec{y} = F(\vec{x}, \vec{b}) + \epsilon, \quad (4.1)$$

where \vec{y} is the measurement vector, in our case the observed photocounts from RSL, \vec{x} is the state vector for which we are solving, in our case the neutral density profile, \vec{b} is the known model parameter vector, and ϵ is the measurement noise. The solution for the state vector is found by minimizing a cost function associated with the forward model:

$$cost = [\vec{y} - F(\vec{x}, \vec{b})]^T \vec{S}_\epsilon^{-1} [\vec{y} - F(\vec{x}, \vec{b})] + [\vec{x} - \vec{x}_a]^T \vec{S}_a^{-1} [\vec{x} - \vec{x}_a], \quad (4.2)$$

where \vec{S}_ϵ is the error covariance matrix of \vec{y} , and \vec{x}_a is the a priori array with covariance matrix \vec{S}_a . The a priori is used to constrain the solution to physically plausible solutions. The algorithm attempts to minimize the cost value by adjusting the state vector \vec{x} until the second part of the right side of equation 2 becomes smaller than a chosen threshold. A cost value of order unity is the desired outcome.

The forward model used to determine the neutral density based on RSL photocounts is the lidar equation which relates the observed back-scattered photons to

instrument parameters and the number density at a given altitude. Here the equation is written in the general form as from Equation 1:

$$N_t(z) = \psi(z) \frac{n(z)}{z^2} + B, \quad (4.3)$$

where $N_t(z)$ is the observed photocount at altitude z , and $n(z)$ is the neutral number density at altitude z . B is the background noise, which is also retrieved in the OEM.

The instrument function is

$$\psi(z) = C \sigma_R(z) e^{-2\tau_{O_3}(z)} e^{-2\tau_R(z)}. \quad (4.4)$$

Here, C is the lidar constant, also retrieved in the OEM, consisting of the area of the receiver, the receiver efficiency, the detector quantum efficiency, and the number of emitted photons per unit time; $\sigma_R(z)$ is the Rayleigh-scatter cross section; τ_{O_3} is the ozone optical depth at the transmitted wavelength; and $\tau_R(z)$ is the optical depth due to Rayleigh extinction. As the optical depth due to Rayleigh extinction depends on the state vector, $n(z)$, it must be accounted for in the OEM forward model. The composition of the neutral atmosphere begins to change in the mesopause due to photodissociation and diffusive equilibrium of O_2 above 90 km (Argall, 2007). As such, MSIS is used to provide an estimate of the Rayleigh-scatter cross section at each altitude to account for this change.

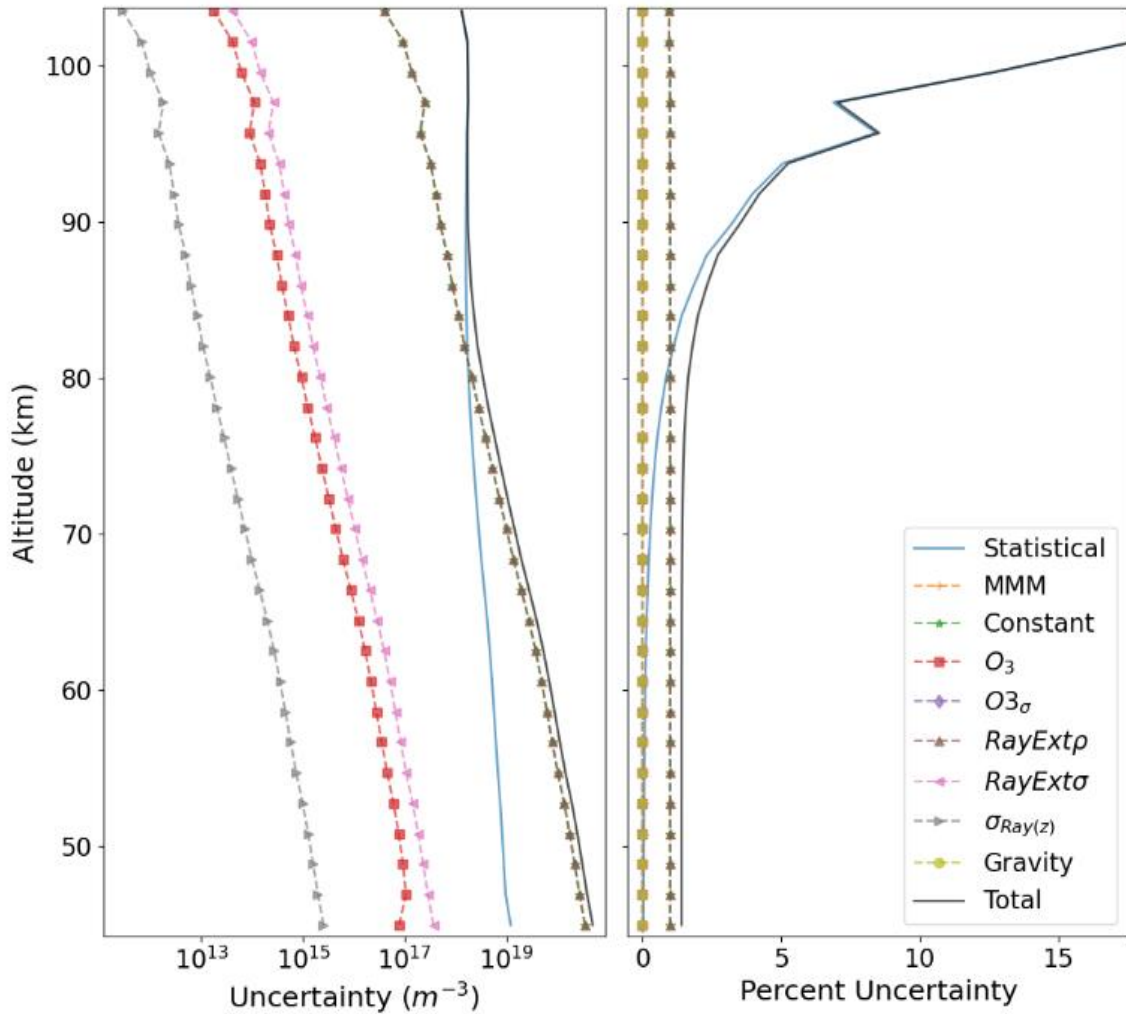


Figure 4.1: Uncertainty budget for the density reduction of RSL observations for the night of January 4, 1995.

The OEM provides a full uncertainty budget for all parameters used to obtain the densities (Figure 4.1). This includes the uncertainty due to model parameters, measurement noise and statistical uncertainties. Along with this, the derived averaging kernel matrix (not shown) is used to determine the sensitivity of the retrieved density to the changes in the real atmosphere and a mathematically derived value for the topmost

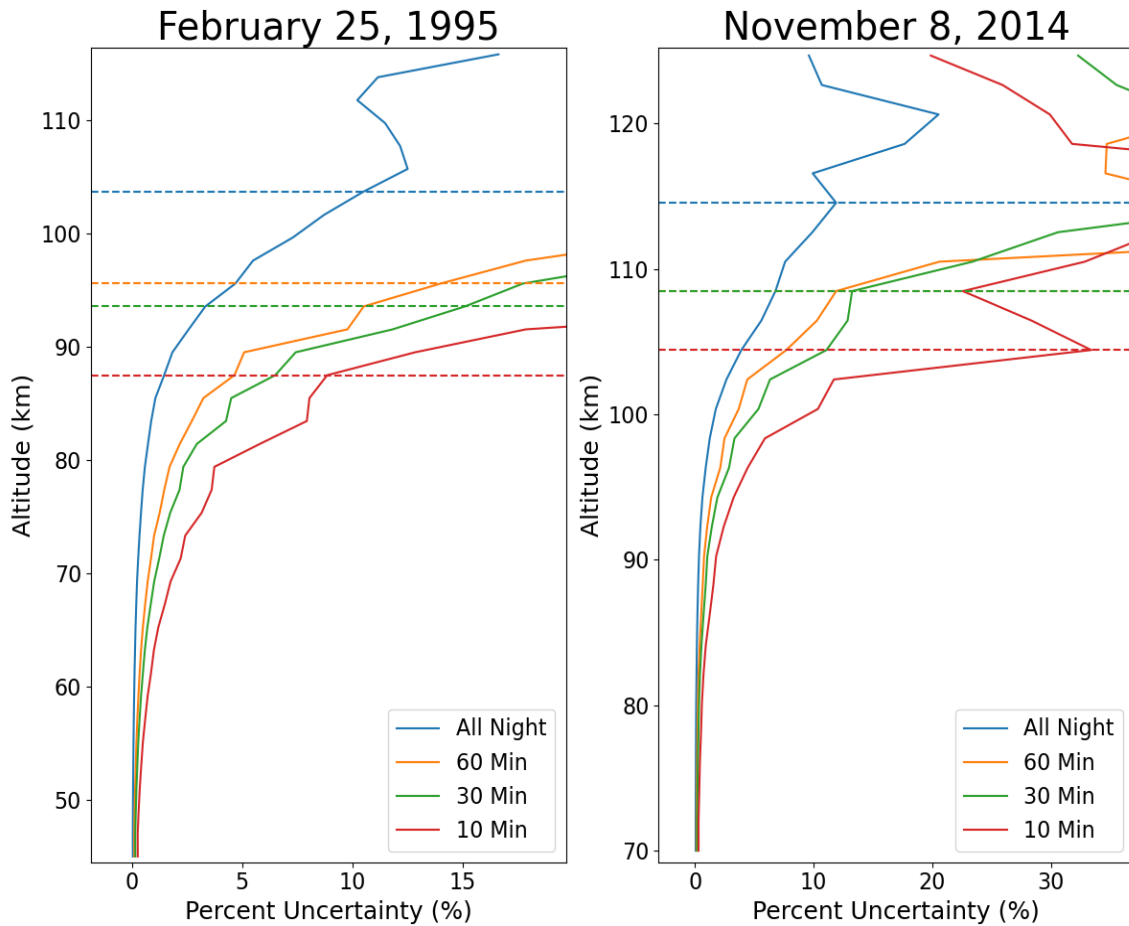


Figure 4.2: Density percent uncertainties at different temporal resolutions for the nights of February 25, 1995 (left) and November 8, 2014 (right). Here we see the percent uncertainties grow with finer temporal resolution along with lowering the top altitude (dashed lines with the 60 min and 30 min profiles in November having the same top altitude).

valid altitude (Rodgers, 2000; Sica & Haefele, 2015). Below the top-most valid altitude,

the a priori densities have minimal effect on the density retrieval (Jalali et al., 2018).

As discussed in chapter 2 with temperature uncertainties, the total OEM density uncertainties depend on the chosen temporal resolution. As an example of this, Figure 4.2 shows the density percent uncertainties for temporal resolutions of all night (9 hours for February 25 and 11.5 hours for November 8), 1-hour, 30-minutes, and 10-minutes all

with a 2 km altitude resolution using the original and upgraded lidar data. Here we see that, along with lowering the top altitude of the profile (dashed lines, discussed in chapter 2), the percent uncertainties increase starting at the lowest altitudes with finer temporal resolution. Above the top altitude the uncertainties are not reliable, as with the data, because the a priori becomes more significant than the observations.

2.2 Reanalysis Model Densities

An alternative method for obtaining an absolute density profile in the mesosphere using RSL observations is by normalizing the observed relative values at some altitude to the model density at that altitude. Reanalysis models, such as MERRA-2, ERA20c and JRA-55, provide estimates for various atmospheric state variables, such as temperature and pressure. Reanalysis model parameters are determined by constraining theoretical calculations to available observations from various sources of ground-based and satellite-based instruments (Gelaro et al., 2017; Harada et al., 2016; Kobayashi et al., 2015; Koster et al., 2016; Poli et al., 2016). They extend the model parameters to above 45 km. The use of empirical data to restrain model calculations gives benefit over using values obtained from strictly theoretical models or strictly from observations. The model chosen for this study is NASA's Modern-Era Retrospective analysis Research and Applications, version 2 (MERRA-2). Model temperature and geopotential height were selected for pressure levels from 5 hPa to 0.1 hPa (~36 km to ~65 km) with ALO-USU

(41.74° N, 111.81° W) at the center of a 1° latitude by 1° longitude grid. Geopotential height was converted into geometric altitude. Then temperature and pressure were interpolated in altitude to 45 km. The ideal gas law was then used to obtain model density values at 45 km. This process was done for each available night of observations from ALO-USU.

Normalized densities ($N_n(z)$) are obtained from RSL signal, $N_r(z)$, by normalizing to unity at an altitude of 45 km:

$$N_r(z) = P_{counts}(z) * R^2 \quad (4.5a)$$

$$N_n(z) = \frac{N_r(z)}{N_r(z = 45)} \quad (4.5b)$$

where $P_{counts}(z)$ are the observed photocounts and R is the relative height above ALO-USU. The distinction between height, R , and altitude, z , is the altitude accounts for height above sea level where the height is relative to the ALO-USU laser as the starting altitude. The RSL relative densities are then scaled to the MERRA-2 density at 45 km by

$$N_a(z) = N_{merra}(z = 45) * N_n(z). \quad (4.6)$$

Uncertainties in the signal follow Poisson statistics where the variance is equal to the signal at each altitude. The effect on uncertainties due to the initial MERRA-2 density values are not represented in the results as they are not made clear in the literature.

Reinecker et al. (2008) outlines the various uncertainties of data assimilated into MERRA-2, which are altitude and latitude dependent, but are unclear on resulting

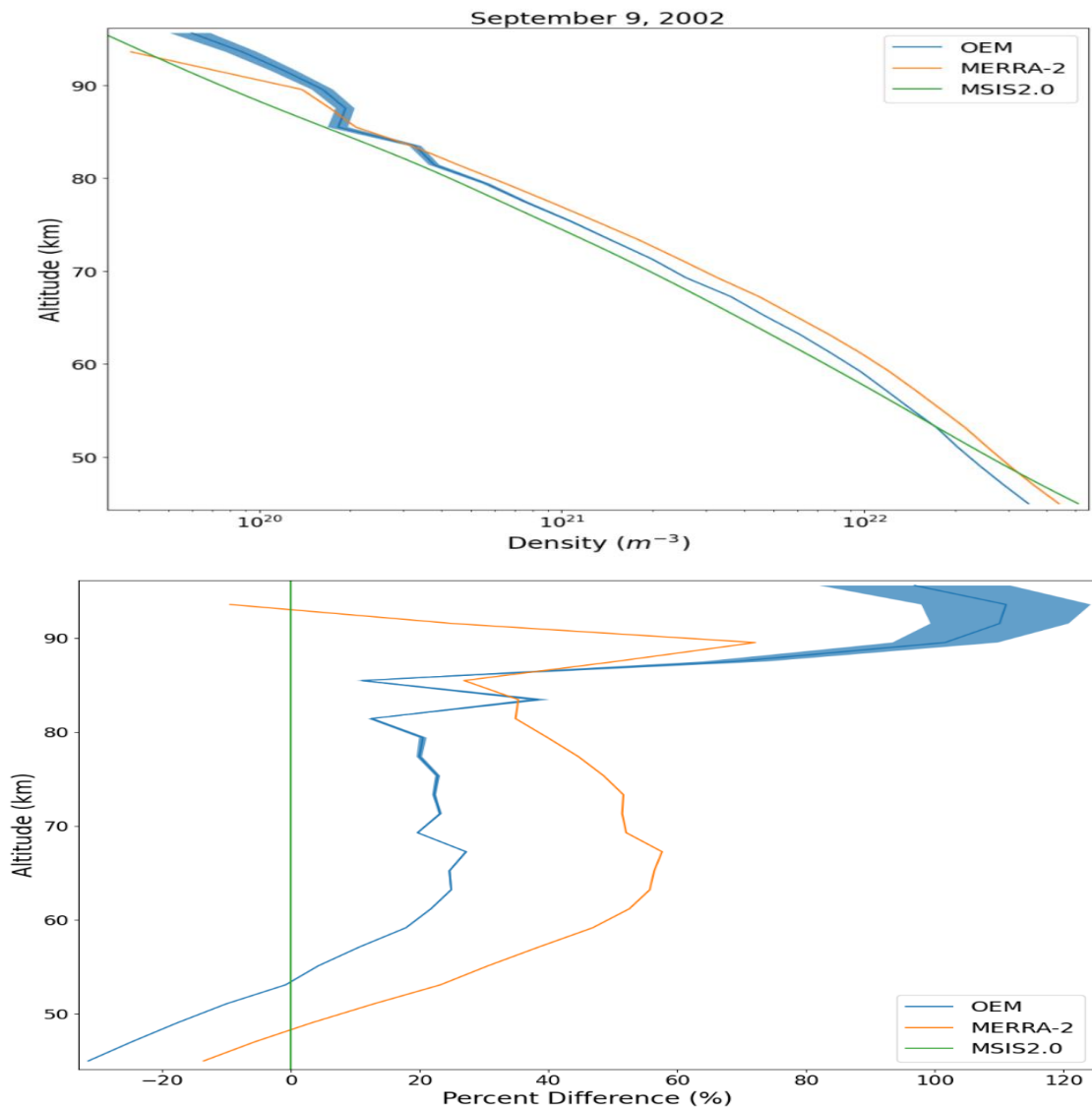


Figure 4.3 a (top): Density profiles from OEM, MERRA-2 and MSIS2.0 for the night of September 9, 2002. Large differences between OEM and MERRA-2 are shown due to a large difference in the scaling value at 45 km from MERRA-2. Figure 4.3b (bottom): Percent difference of OEM and MERRA-2 with respect to MSIS2.0. The large differences in density values can be seen more clearly between OEM and MERRA-2 while the shape of the profile remains similar. The difference between OEM and MERRA-2 is shown to be as large as 25%. This demonstrates the significant influence of the scaling value used to find absolute density and the drawback of this method.

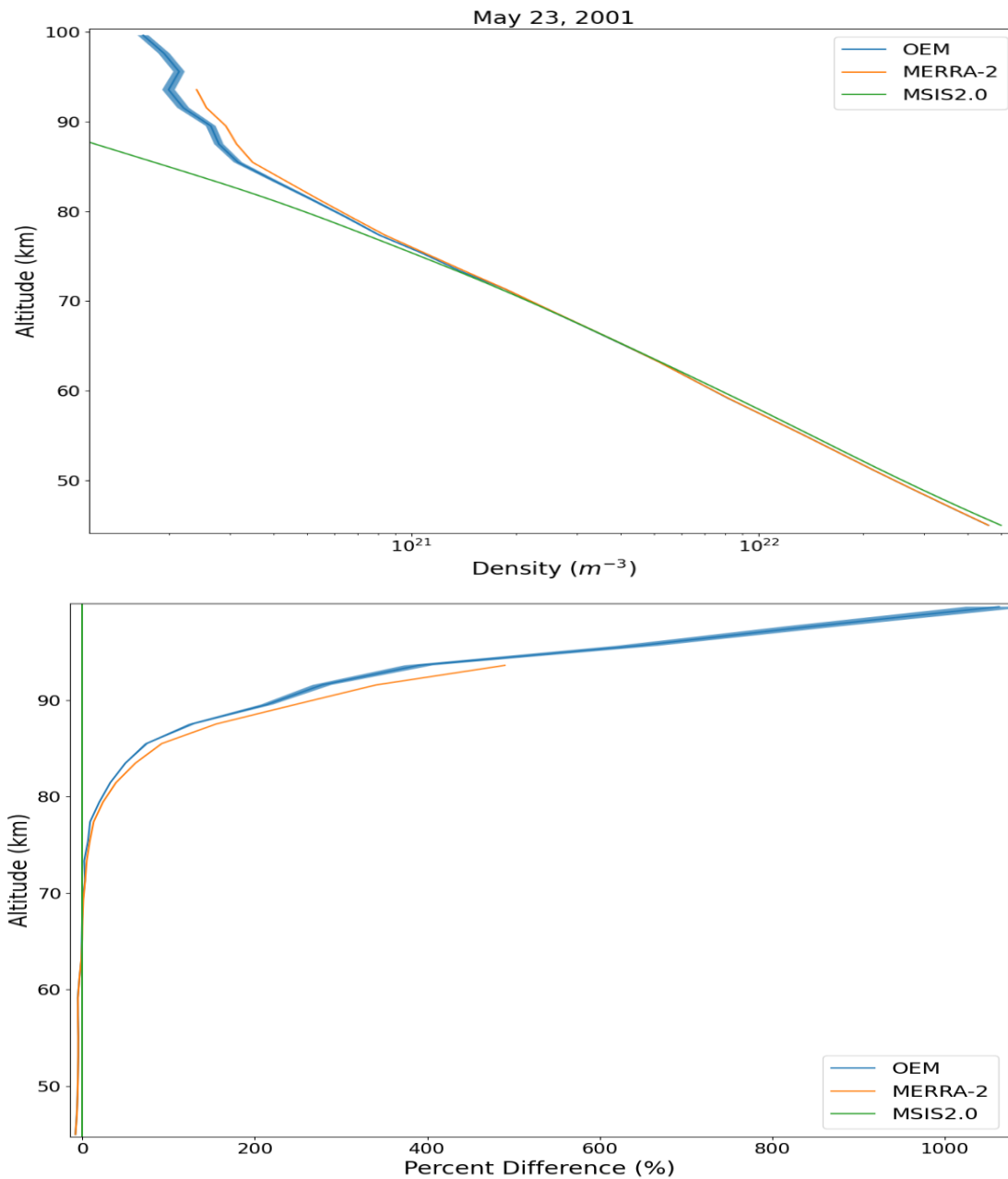


Figure 4.4a (top): Same as Figure 4.3a for May 5, 2001. The initial value in MERRA-2 at 45 km is much closer to the OEM value at 45 km resulting in a better agreement in density profiles. Figure 4.4b (bottom): Same as Figure 4.3b for February 17, 1997. This shows a closer view of the similarities in density profiles produced by scaling and OEM.

uncertainties from model outputs. The topmost altitude where the signal is still deemed useable is determined using an arbitrary value for the ratio of the lidar signal to the

uncertainty (Herron, 2007; Sox, 2016; Wickwar et al., 2001). The chosen threshold is a signal-to-sigma of 1/16. Densities at altitudes associated with a value smaller than this ratio are therefore ignored.

3. Comparison Results

Log plots of the OEM densities, lidar relative densities normalized to the MERRA-2 densities at 45 km, and MSIS2.0 empirical densities for the night of September 9, 2002 are shown in Figure 4.3a. A shift in the MERRA-2 density profile relative to that of the OEM of $\sim 9 \times 10^{21} \text{ m}^{-3}$ is apparent. Figure 4.3b shows the percent difference between OEM and MSIS2.0 and between MERRA-2 and MSIS2.0. The shift is evident in this plot with a difference between OEM and MERRA-2 densities of $\sim 25\%$. The error bars from the MERRA-2 densities are not shown as a result of insufficient information on the model uncertainties. A statistical comparison using the coefficient of determination, r^2 , of the density profiles results in a value of 0.99997. The r^2 value indicates how much variation exists between the two curves with a value of one being a perfect fit, thus the two density profiles show good agreement in structure. This is a further indication that the resulting densities properly reflect the original RSL data. Similar results are shown in Figure 4.4a from May 5, 2001 with a closer match between OEM and MERRA-2 based

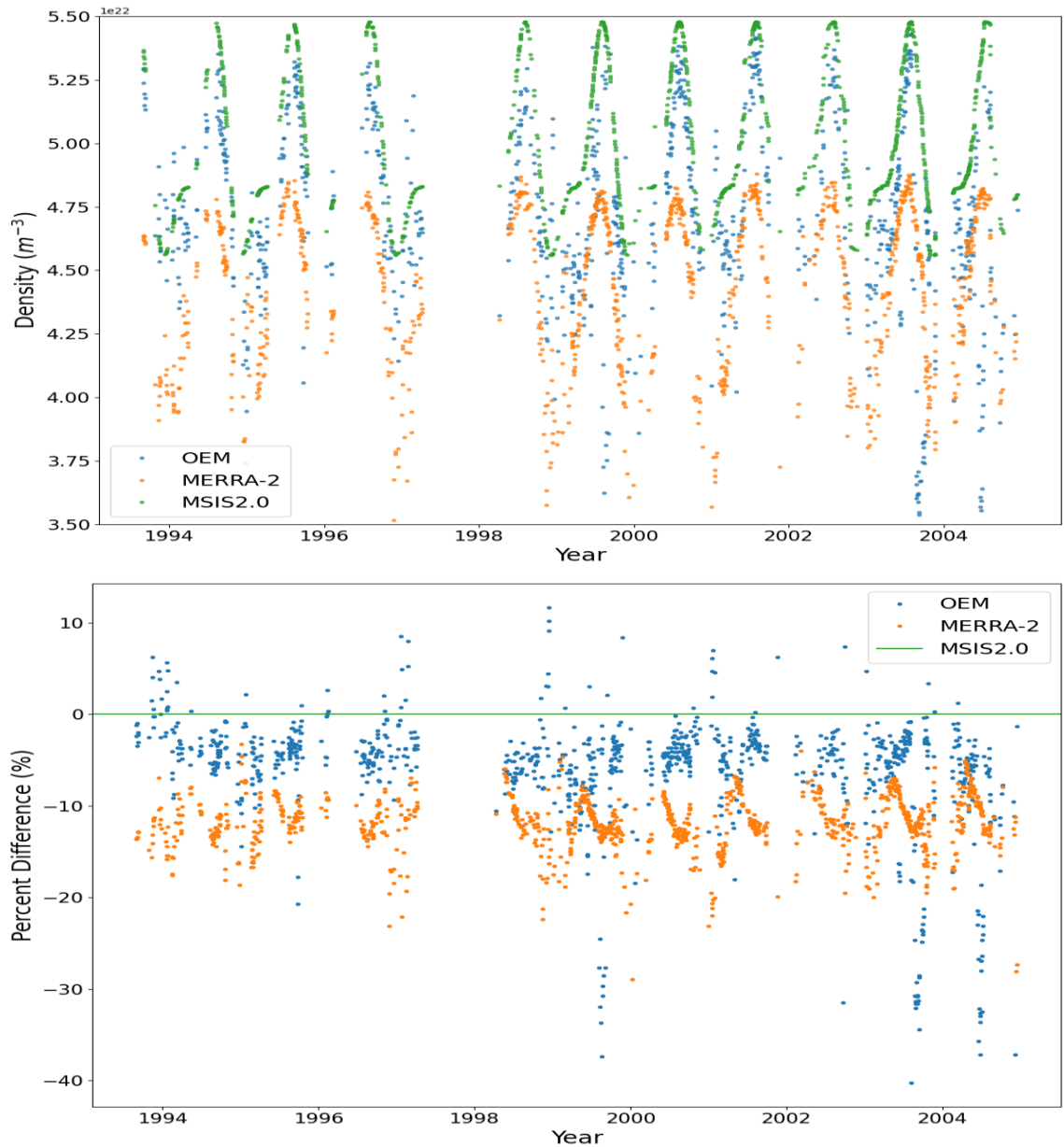


Figure 4.5a (top): Absolute density values for each night of RSL-USU data at 45 km for OEM, MERRA-2 and MSIS2.0. An obvious annual oscillation is present in all three profiles. Figure 4.5b (bottom): The percent difference between OEM and MERRA-2 with respect to MSIS2.0 at 45 km for each night of RSL-USU data. Larger negative values in MERRA-2 demonstrate consistently smaller density values in MERRA-2 over OEM.

densities at lower altitudes. This is further evident in Figure 4.4b with differences less than 1% below 75 km.

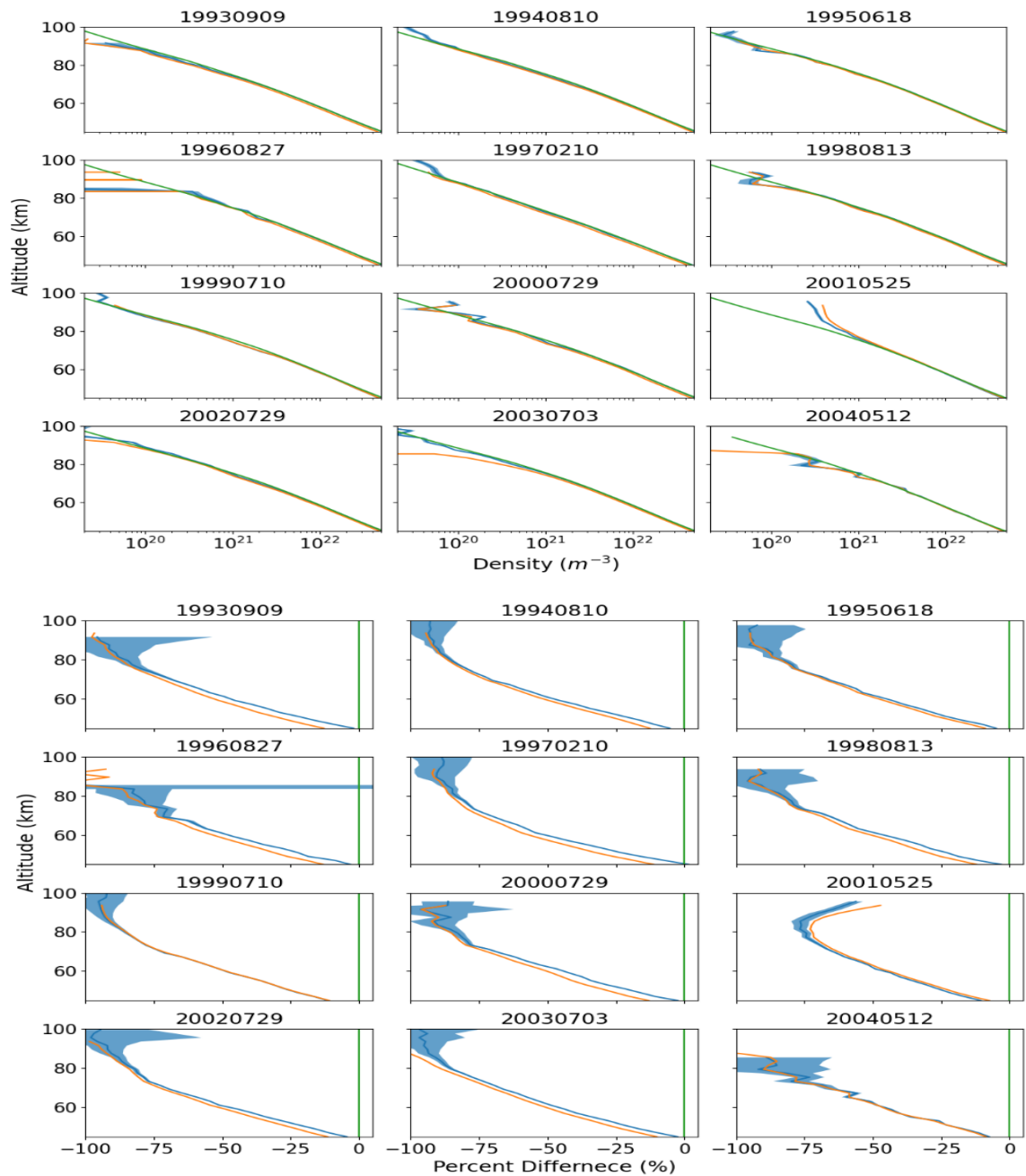


Figure 4.6a (top): Samples of nighttime absolute density profiles from OEM, MERRA-2 and MSIS2.0 from each year of available data. Figure 4.6b (bottom): Samples showing the percent differences between OEM and MERRA-2 with respect to MSIS2.0 from each year of available data.

Figure 4.5a shows the OEM, MERRA-2 and MSIS2.0 density values at 45 km. At this altitude, the MERRA-2 values are independent of the RSL signal. A strong annual

oscillation is seen in all three with peak densities occurring in the summer months. Differences in actual density values can be seen, particularly in Figure 4.5b which shows the percent difference between OEM vs. MSIS2.0 and MERRA-2 vs. MSIS2.0. Here we see consistently smaller density values at 45 km in MERRA-2 than in OEM. A similar result was found by Moser (2019) where reanalysis model temperature values at 45 km are consistently lower than RSL temperatures at that altitude.

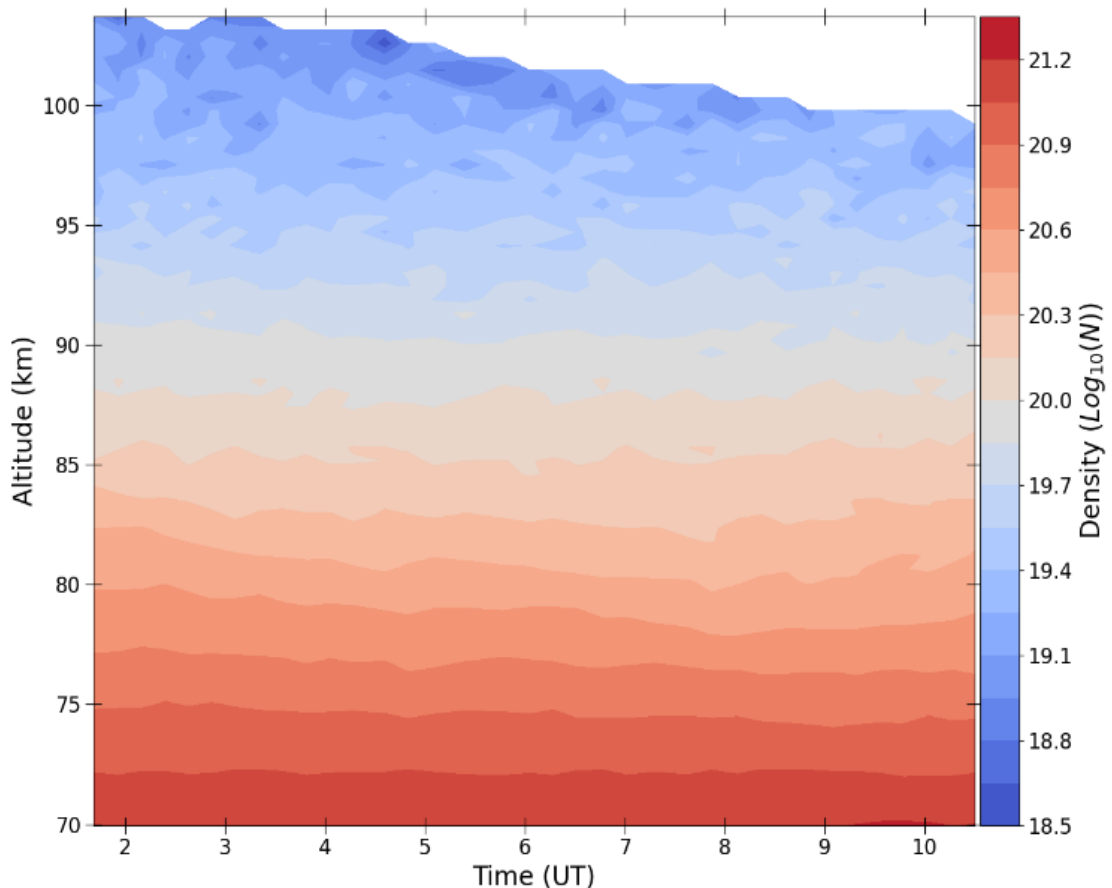


Figure 4.7: A contour plot of the log of density profiles for the night of November 8, 2014. Each profile was integrated over 15 minutes for a total of 36 profiles with an altitude resolution of 500 m.

4. High-Altitude Lidar Densities

The high-altitude lidar densities, which start at 70 km, were produced in 15-minute integrations with an altitude resolution of ~ 500 m for the night of November 8, 2014.

Figure 4.7 shows a plot of the log of the 15-minute integrated absolute neutral densities. The top altitude of each profile declines over the course of the night, starting at ~ 104 km and ending at ~ 99 km, likely due to a combination of declining return signal

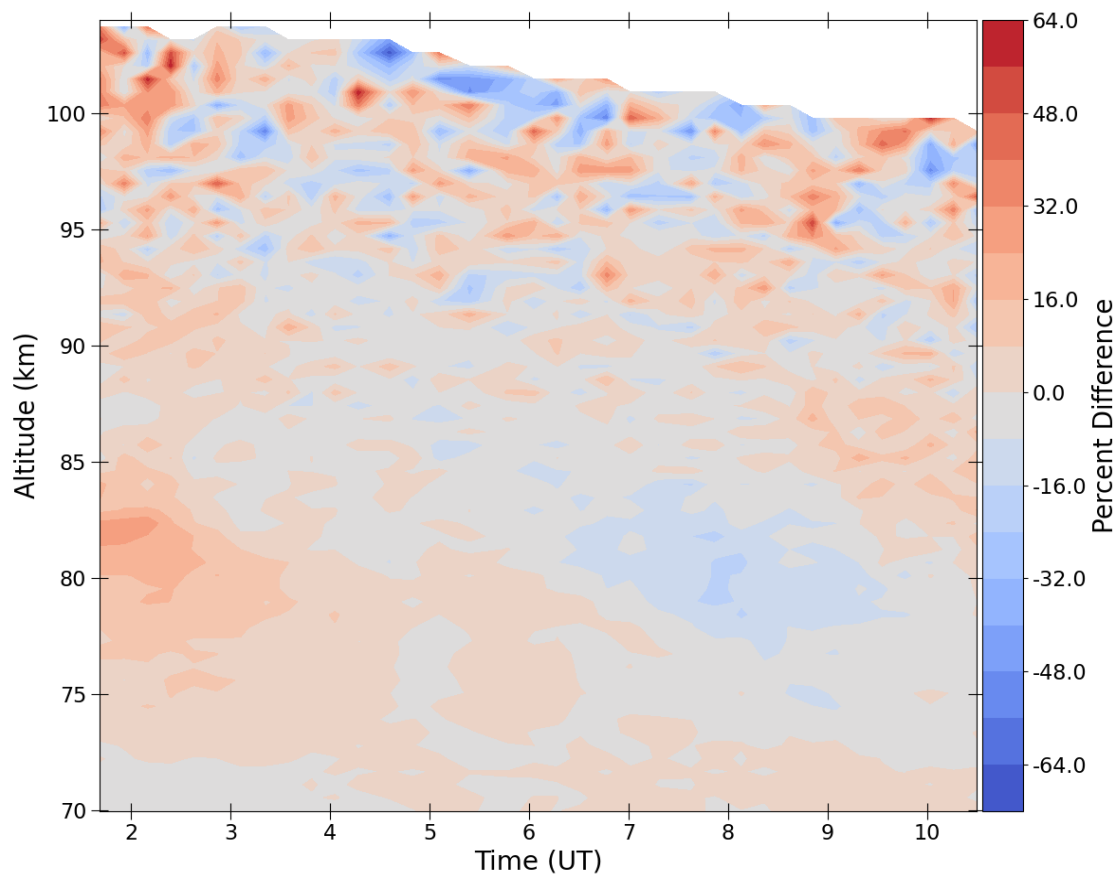


Figure 4.8: Contour plot showing the percent difference of the 15-minute density profiles minus the all-night average density profile.

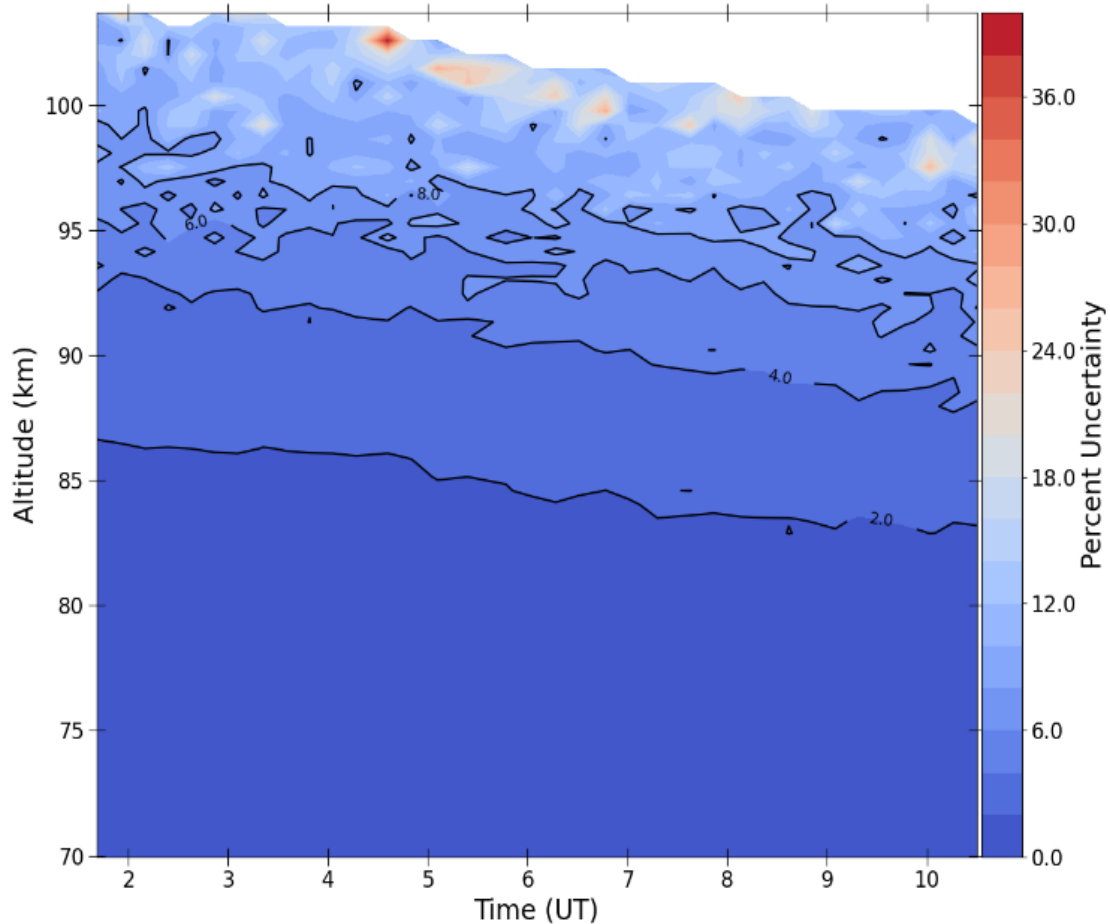


Figure 4.9: Contour plot of the percent uncertainties of the absolute densities from November 8, 2014. Overall, uncertainties are low except for a few pockets at high altitudes.

and increasing background noise. Some features can be noted from this plot, such as high frequency oscillations above 90 km. However, to obtain a closer look at these features, the percent difference of the profiles minus the all-night average density profile (Figure 4.8). Here we see below 75 km that the density is nearly constant with a slight change from lower to higher density in the middle of the night. At ~83 km we see a prominent semi-diurnal oscillation with the maximum centered around 2 UT and the minimum centered around 8 UT. Above this level shorter wavelength oscillations and

turbulence have a larger influence with the largest swings in density occurring at higher altitudes.

Figure 4.9 shows the percent uncertainties for the densities shown in Figure 4.7. The uncertainties increase at a given altitude over the course of the night, again as the photocounts decline and background noise increases. The densities have an uncertainty of 8% and below up to above 95 km for most of the night, increasing to ~10% at 95 km for the last couple of hours. A few profiles with higher uncertainties at high altitudes contribute to a few pockets of uncertainties >20%, but the uncertainties at these altitudes are at or below 18% with an average uncertainty for densities above 100 km being ~13%.

5. Conclusions

OEM offers a new way to obtain absolute neutral densities in the mesosphere using Rayleigh-scatter lidar observations. Benefits over other methods include computation of a full uncertainty budget and densities that have minimal dependence on the a priori values and provide a mathematically derived value for the topmost valid altitude (Jalali et al., 2018; Rodgers, 2000; Sica & Haefele, 2015).

Scaling with reanalysis models can be used to determine the density, however the dependence on a model value to scale to introduces unknowns such as biases in the

model output that are difficult to account for and uncertainties that are not well defined. Also, the altitude limitations of reanalysis models make them impractical if the lower limit of the lidar altitude is above the upper limit of the model. Because of this we were unable to normalize to MERRA-2 with the high-altitude lidar data. Further, a study by Moser (2019) has outlined the large, consistent differences in reanalysis model temperatures at 45 km compared with those obtained at RSL-USU. This discrepancy will transition into the densities through the ideal gas law.

There are other methods for obtaining neutral densities. Seeding densities using sounding rocket observations can provide good density estimates but the infrequency of the observations and the typically remote location of the launch site make this impractical for broader studies of the neutral atmosphere. Obtaining absolute neutral densities can be done numerically using RSL observations, as presented in Mwangi et al., (2001). This method as outlined relies on independent temperature observations from a collocated instrument such as a sodium lidar. This reliance on other measurements limits this method and the use of sodium temperatures limits the altitudes range of the retrieval to approximately between 95 km and 110 km. Additionally, it has been shown there is disagreement between sodium and RSL temperatures (Argall & Sica, 2007; Sox et al., 2018), which merits further study into why these discrepancies exist and to determine which temperature results are the more reliable.

High-altitude RSL observations from ALO-USU were used to obtain densities in the mesosphere and lower thermosphere with 15-minute temporal and 500 m vertical resolution. These finer resolutions can be useful for studies in atmospheric oscillations of higher frequency, such as gravity waves, and could prove useful for estimating drag conditions higher up in near-earth orbit.

References

- Argall, P. S. (2007). Upper altitude limit for Rayleigh lidar. *Annales Geophysicae*, 25(1), 19–25. <https://doi.org/10.5194/angeo-25-19-2007>
- Argall, P. S., & Sica, R. J. (2007). A comparison of Rayleigh and sodium lidar temperature climatologies. *Annales Geophysicae*, 25(1), 27–35. <https://doi.org/10.5194/angeo-25-27-2007>
- Barton, D. L., Wickwar, V. B., Herron, J. P., Sox, L., & Navarro, L. A. (2016). Variations in Mesospheric Neutral Densities from Rayleigh Lidar Observations at Utah State University. *EPJ Web of Conferences*, 119, 13006. <https://doi.org/10.1051/epjconf/201611913006>
- Bosilovich, M., Akella, S., Coy, L., Cullather, R., Draper, C., Gelaro, R., & Kovach, R. (2015). MERRA-2: Initial Evaluation of the Climate, 43, 145.
- Gelaro, R., McCarty, W., Suárez, M. J., Todling, R., Molod, A., Takacs, L., et al. (2017). The Modern-Era Retrospective Analysis for Research and Applications, Version 2 (MERRA-2). *Journal of Climate*, 30(14), 5419–5454. <https://doi.org/10.1175/JCLI-D-16-0758.1>
- Haefele, A., De Wachter, E., Hocke, K., Kämpfer, N., Nedoluha, G., Gomez, R., et al. (2009). Validation of ground-based microwave radiometers at 22 GHz for

stratospheric and mesospheric water vapor. *Journal of Geophysical Research: Atmospheres*, 114(D23).

Harada, Y., Kamahori, H., Kobayashi, C., Endo, H., Kobayashi, S., Ota, Y., et al. (2016). The JRA-55 Reanalysis: Representation of atmospheric circulation and climate variability. *Journal of the Meteorological Society of Japan. Ser. II*, 94(3), 269–302.

Hauchecorne, A., & Chanin, M. L. (1980). Density and temperature profiles obtained by lidar between 35 and 70 km. *Geophysical Research Letters*, 7(8), 565–568.

<https://doi.org/10.1029/GL007i008p00565>

Herron, J. P. (2007). *Rayleigh-Scatter Lidar Observations at USU's Atmospheric Lidar Observatory (Logan, UT) - Temperature Climatology, Temperature Comparisons with MSIS, and Noctilucent Clouds*. All Graduate Theses and Dissertations. Retrieved from <https://digitalcommons.usu.edu/etd/4686>

Jalali, A., Sica, R. J., & Haeferle, A. (2018). Improvements to a long-term Rayleigh-scatter lidar temperature climatology by using an optimal estimation method. *Atmospheric Measurement Techniques*, 11(11), 6043–6058. <https://doi.org/10.5194/amt-11-6043-2018>

Kobayashi, S., Ota, Y., Harada, Y., Ebata, A., Moriya, M., Onoda, H., et al. (2015). The JRA-55 reanalysis: General specifications and basic characteristics. *Journal of the Meteorological Society of Japan. Ser. II*, 93(1), 5–48.

Koster, R. D., McCarty, W., Coy, L., Gelaro, R., Huang, A., Merkova, D., et al. (2016). MERRA-2 input observations: Summary and assessment.

Moser, D. K. (2019). *Juxtaposition at 45 km of Temperatures from Rayleigh-Scatter Lidar and Reanalysis Models*. All Graduate Theses and Dissertations. Retrieved from <https://digitalcommons.usu.edu/etd/7434>

Mwangi, M., Sica, R., & Argall, P. (2001). Retrieval of molecular nitrogen and molecular oxygen densities in the upper mesosphere and lower thermosphere using ground-

- based lidar measurements. *Journal of Geophysical Research: Atmospheres*, 106(D10), 10313–10323.
- Palmer, P. I., & Barnett, J. J. (2001). Application of an optimal estimation inverse method to GPS/MET bending angle observations. *Journal of Geophysical Research: Atmospheres*, 106(D15), 17147–17160.
- Picone, J. M., Hedin, A. E., Drob, D. P., & Aikin, A. C. (2002). NRLMSISE-00 empirical model of the atmosphere: Statistical comparisons and scientific issues: TECHNIQUES. *Journal of Geophysical Research: Space Physics*, 107(A12), SIA 15-1-SIA 15-16. <https://doi.org/10.1029/2002JA009430>
- Poli, P., Hersbach, H., Dee, D. P., Berrisford, P., Simmons, A. J., Vitart, F., et al. (2016). ERA-20C: An atmospheric reanalysis of the twentieth century. *Journal of Climate*, 29(11), 4083–4097.
- Rienecker, M. M., Suarez, M. J., Gelaro, R., Todling, R., Bacmeister, J., Liu, E., et al. (2011). MERRA: NASA's Modern-Era Retrospective Analysis for Research and Applications. *Journal of Climate*, 24(14), 3624–3648. <https://doi.org/10.1175/JCLI-D-11-00015.1>
- Rodgers, C. D. (2000). *Inverse methods for atmospheric sounding: theory and practice* (Vol. 2). World scientific.
- Sica, R. J., & Haeferle, A. (2015). Retrieval of temperature from a multiple-channel Rayleigh-scatter lidar using an optimal estimation method. *Applied Optics*, 54(8), 1872. <https://doi.org/10.1364/AO.54.001872>
- Sox, L. (2016). *Rayleigh-Scatter Lidar Measurements of the Mesosphere and Thermosphere and their Connections to Sudden Stratospheric Warmings*. All Graduate Theses and Dissertations. Retrieved from <https://digitalcommons.usu.edu/etd/5227>

- Sox, L., Wickwar, V. B., Yuan, T., & Criddle, N. R. (2018). Simultaneous Rayleigh-Scatter and Sodium Resonance Lidar Temperature Comparisons in the Mesosphere-Lower Thermosphere. *Journal of Geophysical Research: Atmospheres*, *123*(18), 10–688.
- Watts, P., Bennartz, R., & Fell, F. (2011). Retrieval of two-layer cloud properties from multispectral observations using optimal estimation. *Journal of Geophysical Research: Atmospheres*, *116*(D16).

CHAPTER 5

ABSOLUTE NEUTRAL DENSITY CLIMATOLOGY OVER UTAH STATE UNIVERSITY FROM RAYLEIGH-SCATTER LIDAR OBSERVATIONS USING AN OPTIMAL ESTIMATION METHOD

Abstract

Absolute neutral densities from Rayleigh-scatter observations at Utah State University using an optimal estimation method were used to produce composite annual density climatologies from the original lidar data (1993-2004) and from the upgraded lidar data (2014-2015). High densities in the summer and low densities in the winter were seen around 70 km in both climatologies while low summer and high winter densities were visible around 110 km in the upgraded lidar climatology. Comparisons with model and USU normalized climatologies were made, showing good agreement in the extrema found in the original lidar climatology. Comparisons were also made between climatologies of temperature annual percent variation and density annual percent variation. The results show an interesting relation between the extrema found in both the temperatures and densities. They are both centered around the same time of the year in the summer and winter but they are opposite in their behavior. During the summer we see a high-density region around 70 km, whereas the temperature shows a low region ~10 km higher in altitude. The reverse is true for the winter months.

1. Introduction

Studies of the middle atmosphere depend on the state variables, such as temperature, pressure, wind and geopotential height, available from the various types of equipment capable of observing this region. RSL observations have typically relied on temperature profiles to present the various studies that have been done (Kafle, 2009; Moser, 2019; Sox, 2016; Sox et al., 2018). This has been due to the limitations in the reduction of RSL data in the past. Recently (see Chapter 4), an optimal estimation method (OEM) was used to obtain RSL absolute density profiles along with the temperatures, providing another state variable with which to study the middle atmosphere.

Among the various studies that use RSL data, atmospheric climatologies of RSL observations are useful tools that are used to determine the normal behavior of atmospheric variables such as temperature and density. These provide a standard with which to compare individual nighttime observations. Many examples of temperature climatologies exist in the RSL community (Argall & Sica, 2007; Hauchecorne et al., 1991; Herron, 2004, 2007; Jalali et al., 2018) including those done in Herron and Wickwar (2018) that was updated using OEM temperatures in Chapter 3. Recently, a study was done by Barton et al. (2016) that presented RSL neutral density climatologies from model-seeded densities obtained from the early USU data set between 1993 and 2004. The results show that the density climatology depends greatly on the model data used, which is not ideal. A new USU RSL neutral density climatology, which does not rely

heavily on model densities, is presented herein that uses the absolute densities obtained through using OEM. This new climatology was created using the same method as that used to generate the temperature climatology outlined in Chapter 3. It has a 31-day floating point average for each day of the year, for both the original lidar data and the upgraded lidar data. The resulting climatology was compared with results from Barton et al. (2016) as well as with climatologies produced using other model-seeded densities. The models with which the OEM density climatology was compared are

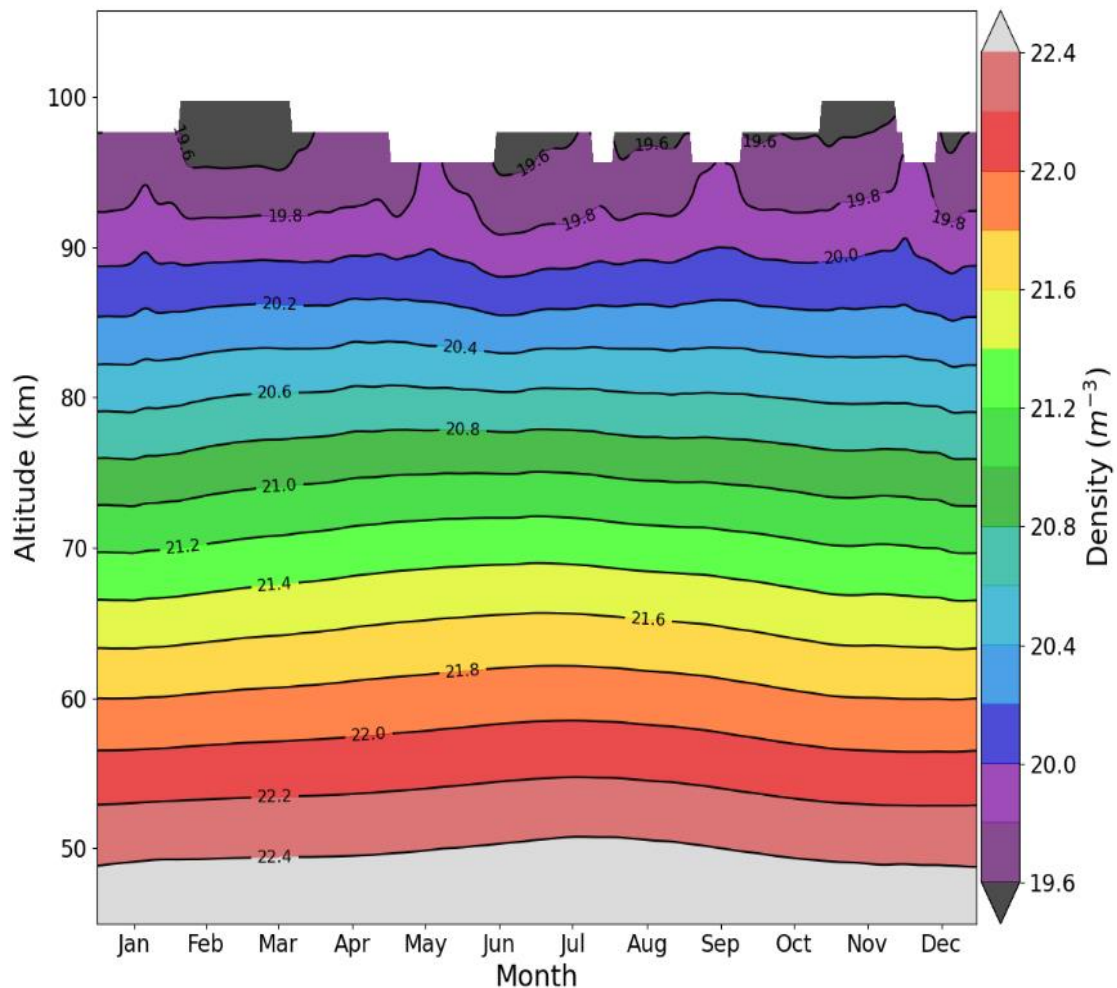


Figure 5. 1: Annual density climatology, using OEM, showing the log of the densities using data from the original lidar (1993-2004).

NASA's Modern Era Retrospective analysis for Research and Applications version 2 (MERRA-2) reanalysis model (Koster et al., 2016; Rienecker et al., 2011) and the Naval Research Lab's Mass Spectrometer Incoherent Scatter radar (MSIS2.0) empirical model (Cheng et al., 2020; Emmert et al., 2020).

2 Absolute Density Climatology

2.1 Original USU RSL System (1993-2004)

A contour plot showing the log of the OEM composite annual absolute density climatology from RSL USU observations between 1993 and 2004 is presented in Figure 5.1. A log scale is used to better view the contours at each altitude range. More gradual changes in the density over the year occur below 85 km. Above that we can start to see more perturbations breaking up the smooth annual cycle. At the highest altitudes we see large perturbations occurring. Although the density values in this region are real, the large bumps found above 90 km, which extend to the top of the profile, could be artifacts of having fewer nights to average. This would cause the few density profiles which reach this altitude to dominate, meaning much less averaging and smoothing occurs. It is possible that these areas of steeper slope in density profiles reflects what is really happening. In this region we know that molecular diffusion begins to suppress the turbulent air motion (Salby, 2012), causing O₂ to split into 2O and the rate of decreasing

density and pressure lessens. Comparisons to results from the upgraded lidar will be discussed in the next section.

Though an annual cycle in Figure 5.1, along with its harmonics, is visible, the log scale makes it somewhat difficult to see the peaks and troughs. Figure 5.2 shows contours of the percentage variation of the density from the annual mean density

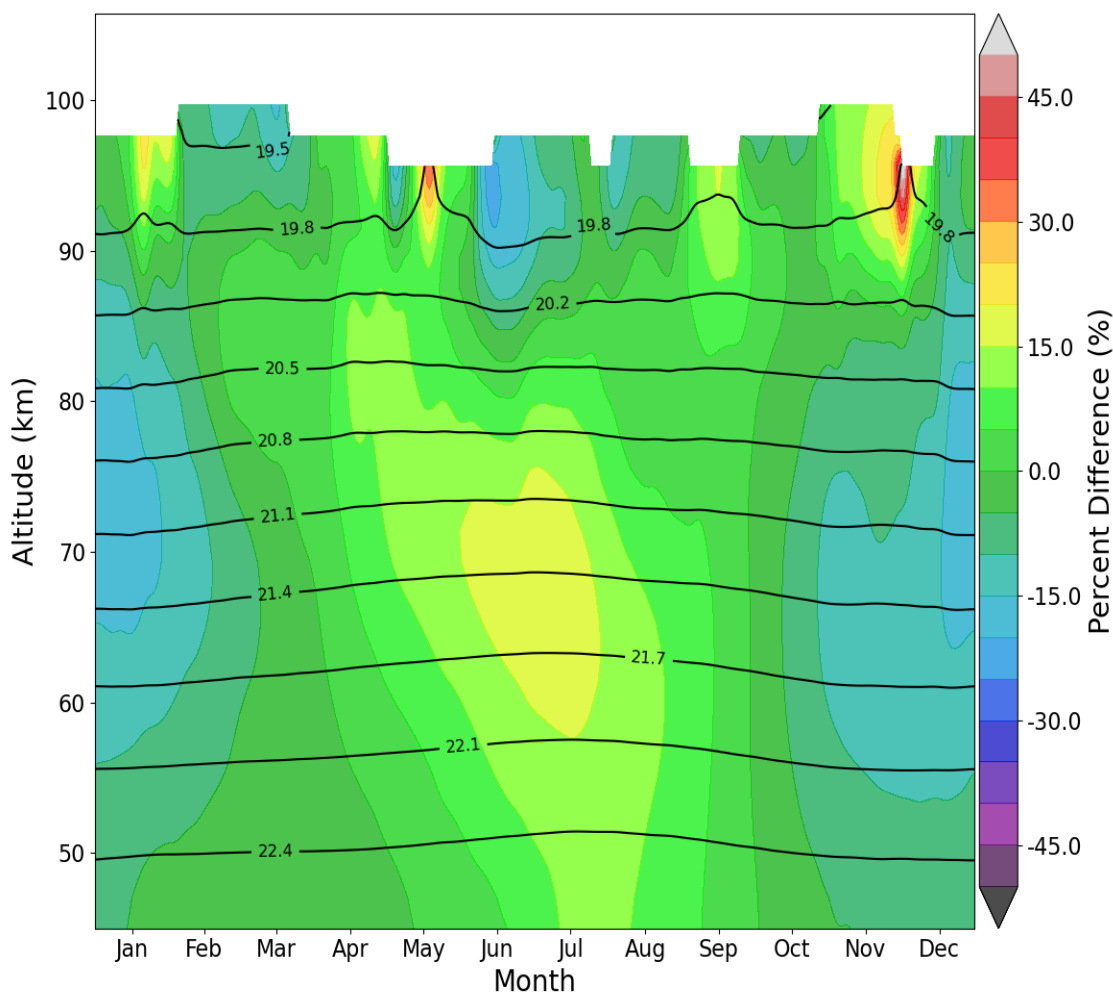


Figure 5.2: Plot showing the annual percent difference in OEM density with the log of the densities superposed on top. This shows the annual oscillation more clearly with peak densities occurring in the summer around 70 km and wintertime low densities centered around 75 km. Also, clear evidence of harmonics of the annual oscillations can be seen above 85 km.

profile superposed on the density contours. The spacing between contour lines is greater here than in Figure 5.1 in order to more clearly see the percent variation in color contour lines. Here we see a clear region of high density which occurs between 60 km and 75 km from late May to early August. In the winter, the lowest densities are between ~65 km and ~81 km from early December to late January, centered about early January. Clear harmonic behavior can be seen with a strong annual oscillation (AO) dominant below 80 to 85 km. Above this, higher order harmonics begin to dominate

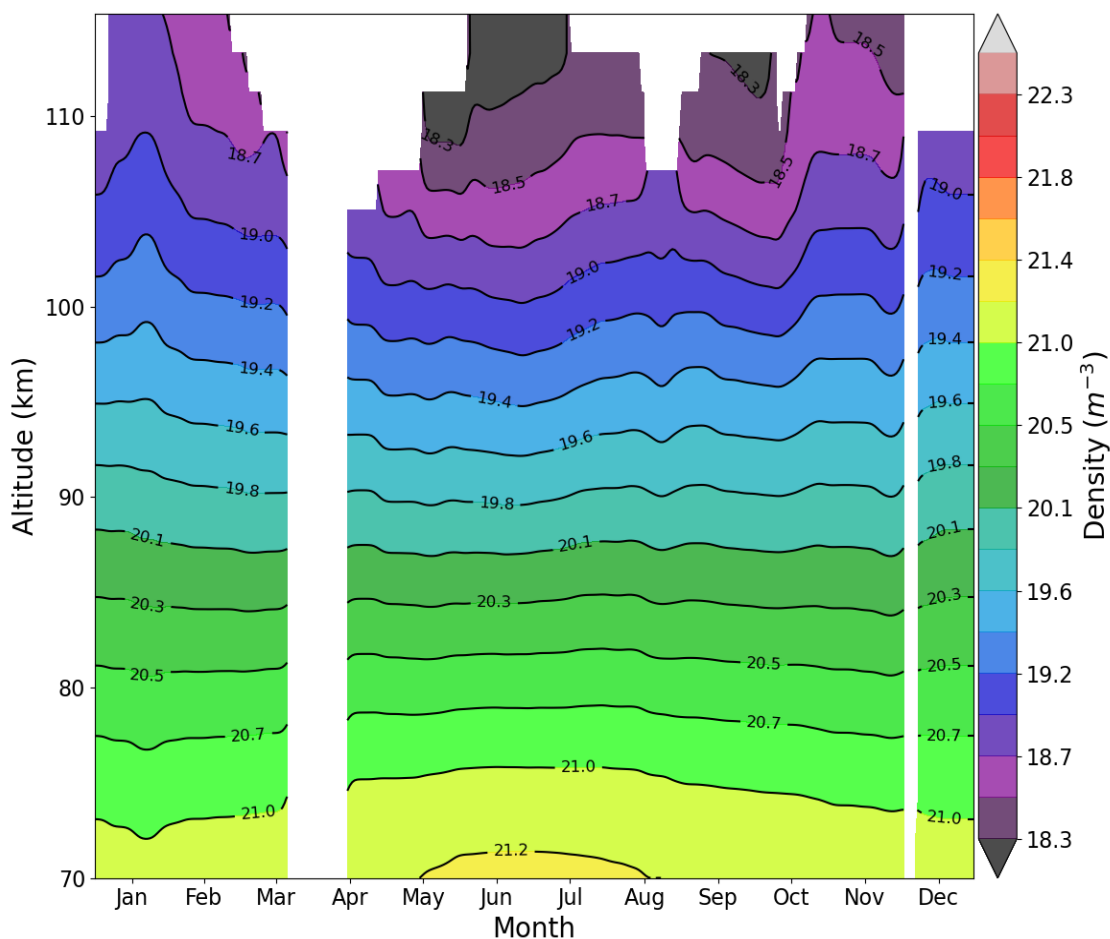


Figure 5.3: Density climatology showing the log of the densities from the upgraded lidar data (2014-2015).

over the AO. The high-density region, around 63 km in June and July, is centered below the low-density region, around 73 km in December and January. This ~ 10 km difference between the high and low density regions can also be seen in the temperature climatology (Figure 3.2).

2.2 Upgraded USU RSL System (2014-2015)

Figure 5.3 shows the contour plot of the log of the annual density climatology using observations from the upgraded USU RSL. Here we see similar density values to those from Figure 5.1, with higher order frequencies apparent above 85 km, without the large jumps we see in the original data. These differences were explored by comparing the single year of densities from the upgraded lidar to an equivalent, single year of densities from the original lidar. Equivalency was based on solar inputs from the annual mean F10.7 and from the sunspot count. The year 2003 produced the closest values, with a mean F10.7 of 128.9 compared to 145.2 for 2014, and a mean sunspot count of 65.8 compared to 74.7 in 2014. Also, the 11-year difference between 2003 and 2014 represents one solar cycle with both occurring near a solar maximum. The solar inputs from 2003 are lower, however they were the closest to the 2014 values of F10.7 and sunspot count of all other years available in the original data.

Figure 5.4 shows the upgraded lidar densities, on the left, next to the 2003 densities, on the right. The number of profiles in the 2003 data set were 150, whereas the 2014 data set has 128. The same scale was used for both contour plots to more easily identify equivalent density levels. A large density spike in the 2003 data can be

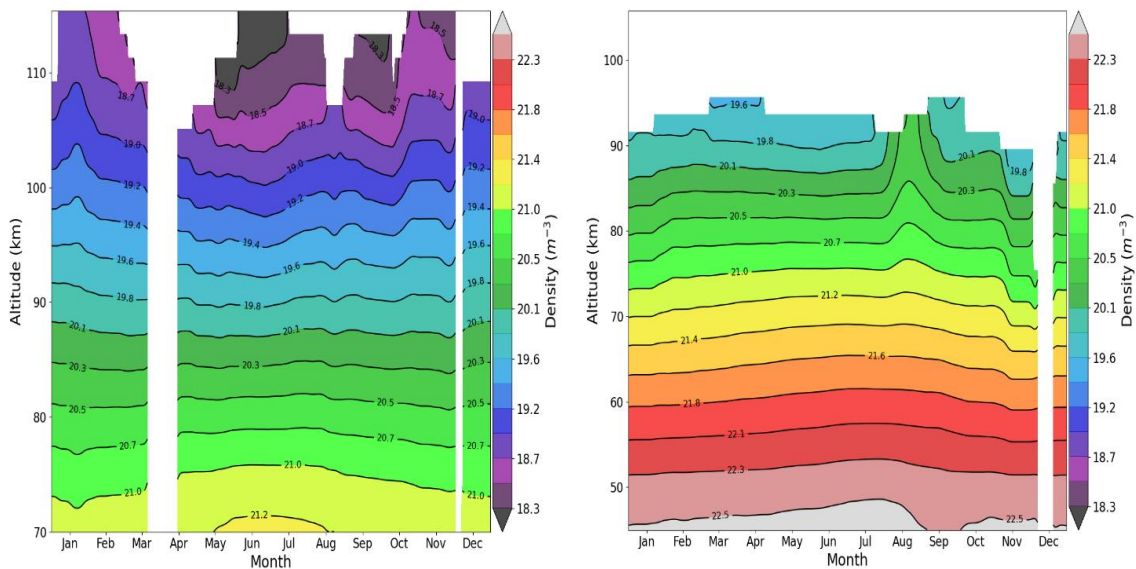


Figure 5.4: Density climatologies from the upgraded lidar (2014-2015), left, and those from the original lidar (2003), right. The log scale is the same in both plots for easier comparison of equivalent density layers.

seen centered around the beginning of September starting just above 70 km, extending to the top of the altitude range. This is not apparent in the 2014 data until higher up, around 80 km, and builds with a double peak rather than the single peak seen in 2003. We also see a drop in density in November starting above 60 km in the 2003 data where in the 2014 data we see the reverse. In January of the 2014 data we see a spike in density starting around 95 km propagating upward. We do see a bump at the same

location above 90 km in the 2003 data, however it is at the top of the altitude range and so we cannot see if it propagates upward also. The spikes we see originate from lower altitudes which suggests they are real since the uncertainties at lower altitudes are smaller, thus the observations are more reliable. Spikes are seen in other annual climatologies which indicates they are unique events within the year they occur. We can see from these two plots is that the differences between the old and new data sets are

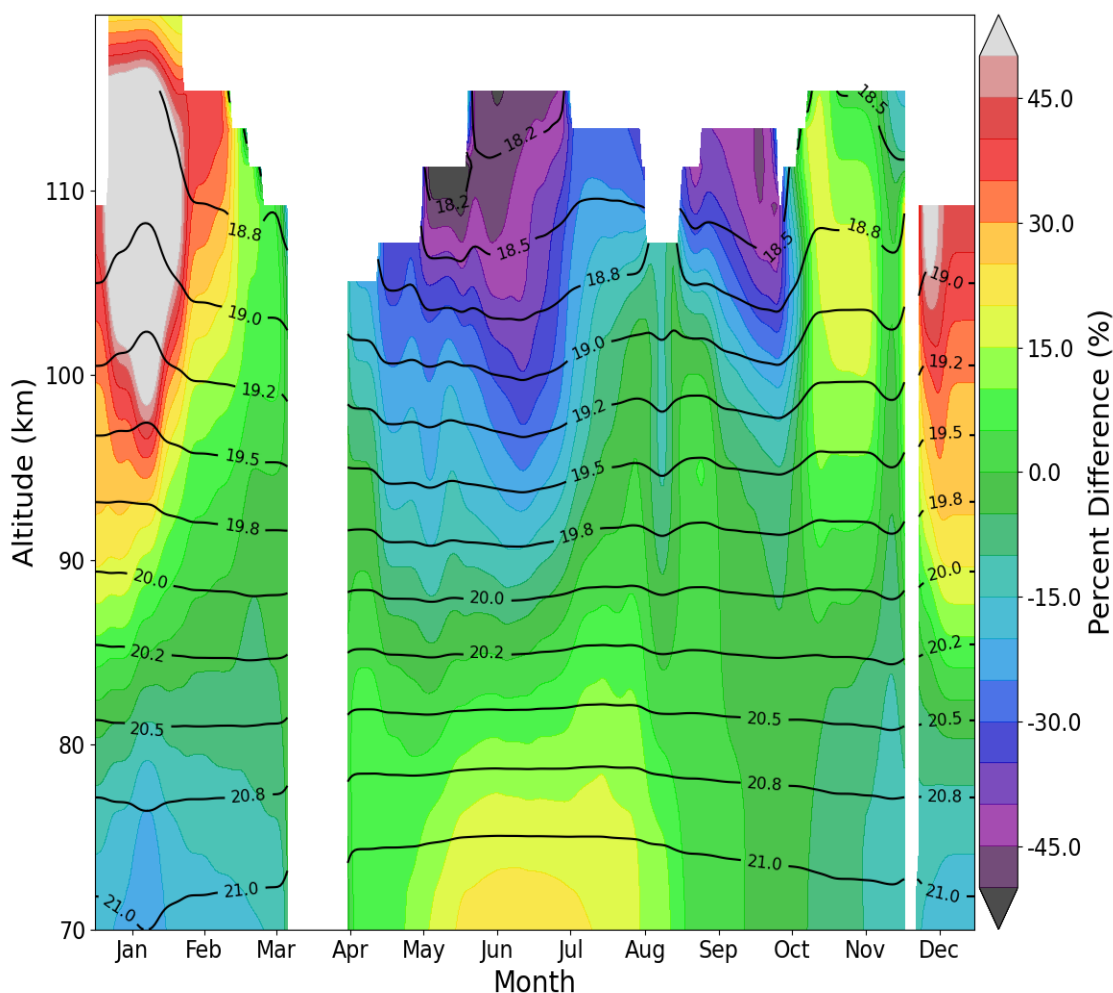


Figure 5.5: Same as Figure 5.2 but with the upgraded lidar densities. Similar maxima and minima to Figure 5.2 are seen around 70 km. Higher up, the maximum occurs in winter around 110 km with the minimum in the summer around the same altitude.

due to more variables than just solar activity and the number of profiles and merits future study.

Similar to Figure 5.2, the contours in Figure 5.5 shows how the density varies from the mean over the year. We can see the top end of the high-density region just above 70 km in the summer with low densities in the winter. The behavior of both data sets below 85 km is remarkably similar. Above 85 km we see harmonics of the annual oscillation starting to become more important. Above 100 km, in the lower thermosphere, the low-density region has a minimum centered around 115 km that stretches from summer into fall while the high-density region occurs in the winter months.

3 Model Comparisons

One of the benefits of using OEM to reduce densities from RSL is that it can be done with data whose starting altitude is higher than reanalysis models can go. Before OEM, the upgraded lidar data could not easily be used to estimate absolute neutral densities using reanalysis models to seed them because they do not extend high enough (for example, MERRA-2 extends to around 65 km maximum with others only extending to just above 45 km). Because of this, only the original lidar densities will be used for comparisons with model-seeded densities and the Barton et al. (2016) results.

Figure 5.6 shows the density climatology on the left from MSIS2.0 densities and on the right USU relative densities normalized to MERRA-2 at 45 km. To be clear, the MSIS2.0 densities are independent of any USU RSL data, they are strictly model densities. In contrast, the so called MERRA-2 densities on the right are obtained by seeding the normalized relative RSL neutral density profiles to the MERRA-2 model density values at 45 km. These are plotted as in Figure 5.2. Note that because the RSL

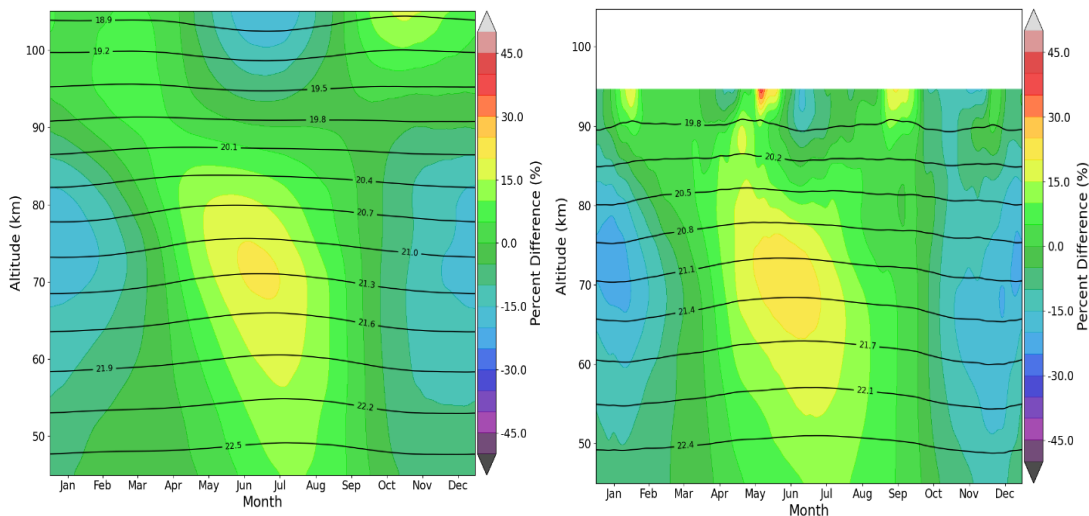


Figure 5.6: Density climatologies from the MSIS2.0 empirical model, left, and from the original USU RSL observations normalized to MERRA-2 densities at 45 km. Similar features in the summer maximum and winter minimum are found in both climatologies.

relative densities are normalized at 45 km, the values at this altitude in the MERRA-2 plot do not have any influence from RSL observation, they are strictly model values.

Above this, however, the RSL observations begin quickly to take over and the influence from the initial values diminishes as altitude increases. This means that the features we see at the higher altitudes reflect the actual RSL observations. Both climatologies

generally show similar high-and low-density areas in the summer and winter, respectively.

Between 90 km and 95 km similar peaks occur in both the OEM (Figure 5.2) and MERRA-2 images, with the notable exception of the peak in early December which is much less pronounced in the MERRA-2 derived plot. The contour lines showing the log of the densities show similar values in each plot, with the MSIS2.0 values slightly higher and the MERRA-2 derived values slightly lower than the other two, up to ~ 95 km where

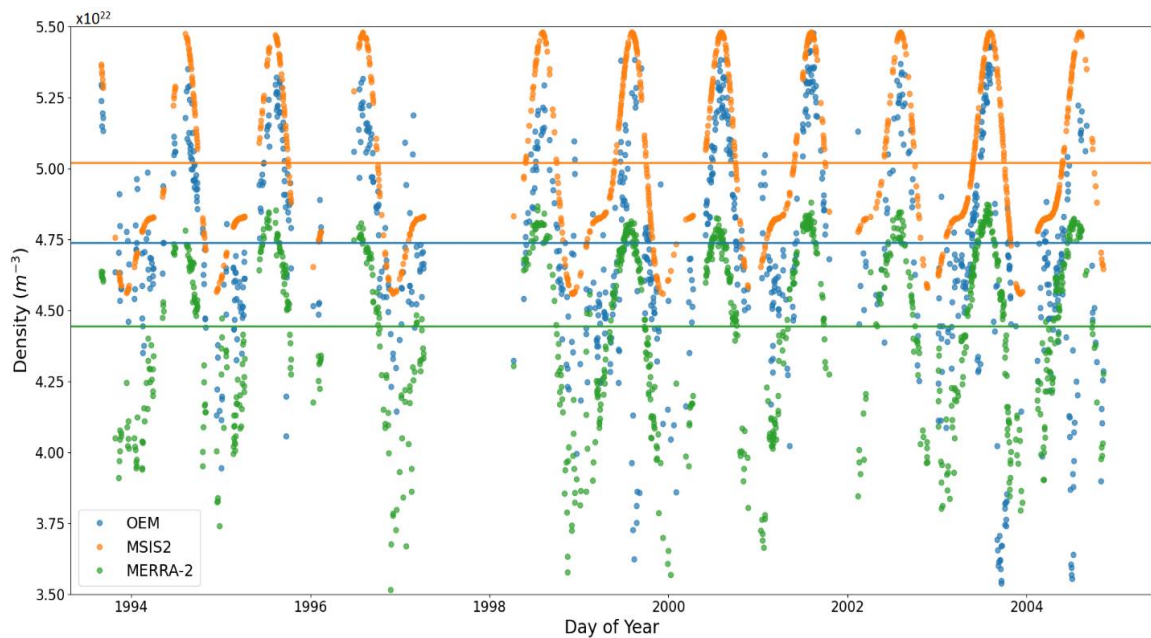


Figure 5.7: Plot of absolute neutral densities at 45 km from the OEM (blue), the MSIS2 model (orange), and the MERRA-2 model (green). The solid horizontal lines represent the value of the average of the densities at 45 km about which the annual oscillation appears to occur. This shows an average difference between OEM and the two models to be around $\pm 3 \times 10^{21} \text{ m}^{-3}$.

we see larger densities occur in the OEM (Figure 5.2). Similar to the temperature climatologies described in Chapter 3, we see higher order frequency oscillations, with

equivalent periods less than the semiannual oscillation (<180 days), occur in the OEM climatology (Figure 5.2) and MERRA-2 seeded climatology but do not occur in the MSIS2.0 climatology. We see many more similarities between the normalized USU densities (Figure 5.6, right) and the OEM-derived USU densities (Figure 5.2) than between either USU-based densities and MSIS2.0 model densities. This is because both methods are highly dependent on the raw RSL observations to produce the densities. The largest benefit of using OEM is that it provides a robust uncertainty budget where the MERRA-2 model does not. So, normalizing to these values produces a large unknown in both precision and accuracy of the model-seeded densities.

Work done by Barton et al. (2016) shows similar plots to Figure 5.6 that were obtained by normalizing other available models, such as ECMWF's ERA and the Climate Prediction Center's CPC, to the original USU data set at 45 km. The results show the significant differences in results from using different normalizing values. The plots do, however, show similar structure in that there are high densities around 70 km in the summer and low density slightly higher in altitude in the winter. Figure 5.7 shows the absolute neutral densities at 45 km from the MSIS2 and MERRA-2 models and the USU density retrieved using OEM. The average density value for each was also plotted horizontally, which is essentially the line about which the annual oscillation apparently occurs. The USU OEM density values are, on average, between the two model values at about $\pm 3 * 10^{21} m^{-3}$. We also see that the USU OEM densities vary more than the models, with a range as large as $1.9 * 10^{22} m^{-3}$ from minimum to maximum while both models have a narrower range of about $1.00 - 1.25 * 10^{22} m^{-3}$.

4 Density and Temperature Climatology Comparison

Some similarities between the OEM temperature climatology shown in Chapter 3 and the OEM density climatology shown here were made previously. Figure 5.8 shows

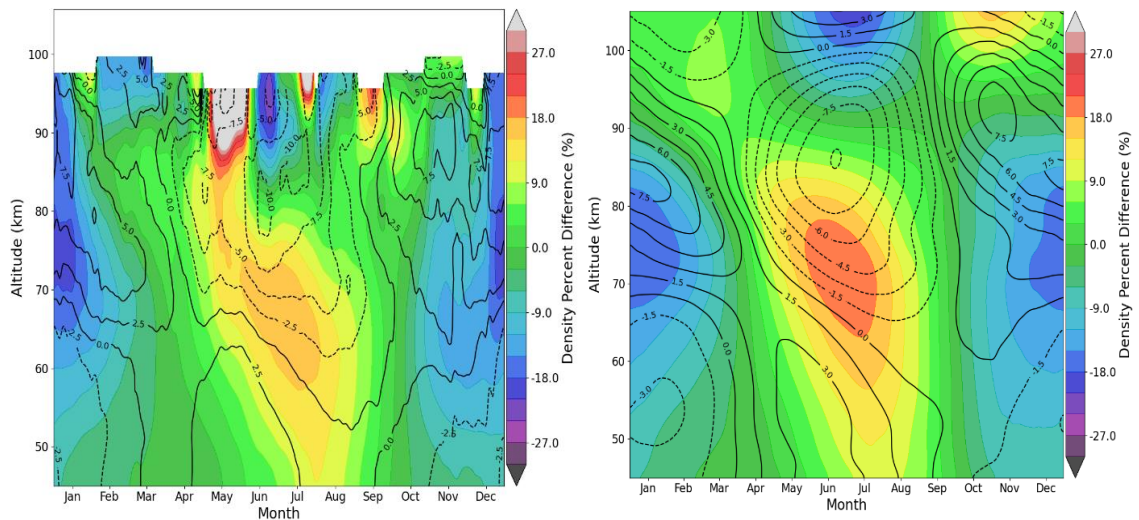


Figure 5.8: Climatologies of the annual percent difference in densities (colored contours) and temperatures (solid and dashed lines) from the original USU RSL data (OEM), left, and from the MSIS2.0 empirical model, right. Both images show the temperature and densities have their maxima and minima occur during the same time of year, but opposite to one another. Also, there is an offset of ~10 km in altitude between the temperature minimum/maximum and the density maximum/minimum.

contour plots from OEM (left) and MSIS2.0 (right) of both the annual percent variation in the temperature (black lines/dashes) and density (colored contours). The MSIS2.0 plot gives us strictly model density and temperature changes for comparison. This gives us the benefit of making a more direct comparison as to how both the density and

temperature are changing over a composite year. We see that, in the OEM temperatures and densities, both have a clear annual oscillation component with the peaks and troughs centered in the summer and winter. However, these extrema occur at opposite times of year with low temperatures occurring in the summer and high densities occurring in summer. We see similar behavior in the MSIS2.0 plot. As mentioned previously, these opposite highs and lows, occurring in the same season, differ in altitude by about 10 km in both the OEM and MSIS2.0 data. We know that through the ideal gas law and hydrostatic equilibrium, the temperatures and densities are directly related as shown in Chapter 2, Equation 2.27. We can take the derivative of this equation with respect to height, h , to get:

$$\frac{1}{n_0} \frac{dn}{dh} = \left(-\frac{T_0}{T^2} \frac{dT}{dh} + \frac{mgT_0}{RT^2} \frac{dT}{dh} \right) e^{-\int_h^{h_0} \frac{m(h')g(h')}{RT(h')} dh'}, \quad (5.1)$$

where density (n), temperature (T), gravity (g) and mean molecular mass (m) all depend on h . First, we can see the inverse relation between density and temperature with the negative sign in front of the first part of the righthand side of the equation. The shift in the positions of minima and maxima from Figure 5.8 are likely dependent on g and m , which depend largely on h , found in the second term on the righthand side of the equation.

5 Conclusions

The climatology produced using the OEM-derived absolute densities shows good structural agreement with the MSIS2.0 model climatology, the MERRA-2 normalized climatology, and those produced in the earlier study by Barton et al. (2016). The main differences are based in the absolute density values in the models, with MERRA-2 generally producing lower densities at 45 km than OEM and MSIS2.0 producing higher densities than OEM. A large benefit to using OEM densities is that we can generate densities using RSL observations that begin at a higher altitude. This was shown with a climatology of the densities from the upgraded USU RSL system. This climatology showed a summer peak density around 70 km, which agrees with the original data set, with an apparent minimum during the summer and into the fall above 115 km. Agreement was demonstrated between climatologies of the percent variation in temperature and density, showing opposite behavior in seasonal extrema and with a separation of ~ 10 km between the maxima and minima altitudes. With the improved lidar system at USU, which will be made operational in 2021, we will be able to obtain density profiles extending from below 40 km to above 120 km. With continued operation, a more complete climatology of the entire mesosphere and lower thermosphere will be made which can be used as a standard against individual nights for comparative purposes.

References

- Argall, P. S., & Sica, R. J. (2007). A comparison of Rayleigh and sodium lidar temperature climatologies. *Annales Geophysicae*, 25(1), 27–35. <https://doi.org/10.5194/angeo-25-27-2007>
- Barton, D. L., Wickwar, V. B., Herron, J. P., Sox, L., & Navarro, L. A. (2016). Variations in Mesospheric Neutral Densities from Rayleigh Lidar Observations at Utah State University. *EPJ Web of Conferences*, 119, 13006. <https://doi.org/10.1051/epjconf/201611913006>
- Cheng, X., Yang, J., Xiao, C., & Hu, X. (2020). Density Correction of NRLMSISE-00 in the Middle Atmosphere (20–100 km) Based on TIMED/SABER Density Data. *Atmosphere*, 11(4), 341. <https://doi.org/10.3390/atmos11040341>
- Emmert, J. T., Drob, D. P., Picone, J. M., Siskind, D. E., Jones, M., Mlynczak, M. G., et al. (2020). NRLMSIS 2.0: A whole-atmosphere empirical model of temperature and neutral species densities. *Earth and Space Science*. <https://doi.org/10.1029/2020EA001321>
- Hauchecorne, A., Chanin, M.-L., & Keckhut, P. (1991). Climatology and trends of the middle atmospheric temperature (33–87 km) as seen by Rayleigh lidar over the south of France. *Journal of Geophysical Research*, 96(D8), 15297. <https://doi.org/10.1029/91JD01213>
- Herron, J., & Wickwar, V. B. (2018). Mid-Latitude Climatologies of Mesospheric Temperature and Geophysical Temperature Variability Determined with the Rayleigh-Scatter Lidar at ALO-USU. *Journal of Geophysical Research*, 59.
- Herron, J. P. (2004). *MESOSPHERIC TEMPERATURE CLIMATOLOGY ABOVE UTAH STATE UNIVERSITY*. All Graduate Theses and Dissertations. Retrieved from <https://digitalcommons.usu.edu/etd/6877>

- Herron, J. P. (2007). *Rayleigh-Scatter Lidar Observations at USU's Atmospheric Lidar Observatory (Logan, UT) - Temperature Climatology, Temperature Comparisons with MSIS, and Noctilucent Clouds*. All Graduate Theses and Dissertations. Retrieved from <https://digitalcommons.usu.edu/etd/4686>
- Jalali, A., Sica, R. J., & Haeefe, A. (2018). Improvements to a long-term Rayleigh-scatter lidar temperature climatology by using an optimal estimation method. *Atmospheric Measurement Techniques*, 11(11), 6043–6058. <https://doi.org/10.5194/amt-11-6043-2018>
- Kafle, D. N. (2009). *Rayleigh-Lidar Observations of Mesospheric Gravity Wave Activity above Logan, Utah*. All Graduate Theses and Dissertations. Retrieved from <https://digitalcommons.usu.edu/etd/466>
- Koster, R. D., McCarty, W., Coy, L., Gelaro, R., Huang, A., Merkova, D., et al. (2016). MERRA-2 input observations: Summary and assessment.
- Moser, D. K. (2019). *Juxtaposition at 45 km of Temperatures from Rayleigh-Scatter Lidar and Reanalysis Models*. All Graduate Theses and Dissertations. Retrieved from <https://digitalcommons.usu.edu/etd/7434>
- Rienecker, M. M., Suarez, M. J., Gelaro, R., Todling, R., Bacmeister, J., Liu, E., et al. (2011). MERRA: NASA's Modern-Era Retrospective Analysis for Research and Applications. *Journal of Climate*, 24(14), 3624–3648. <https://doi.org/10.1175/JCLI-D-11-00015.1>
- Salby, M. L. (2012). *Physics of the Atmosphere and Climate*. Cambridge University Press.
- Sox, L. (2016). *Rayleigh-Scatter Lidar Measurements of the Mesosphere and Thermosphere and their Connections to Sudden Stratospheric Warmings*. All Graduate Theses and Dissertations. Retrieved from <https://digitalcommons.usu.edu/etd/5227>

Sox, L., Wickwar, V. B., Yuan, T., & Criddle, N. R. (2018). Simultaneous Rayleigh-Scatter and Sodium Resonance Lidar Temperature Comparisons in the Mesosphere-Lower Thermosphere. *Journal of Geophysical Research: Atmospheres*, *123*(18), 10–688.

CHAPTER 6

TIDES IN THE MESOSPHERE USING RAYLEIGH-SCATTER LIDAR TEMPERATURE AND DENSITY OBSERVATIONS FROM JULY 20-24, 2003

Abstract

Solar atmospheric tides are global-scale oscillations observable in variables such as temperature, density and wind. They mainly originate in the troposphere and stratosphere through solar radiation absorption, causing them to propagate upwards where they deposit energy and momentum in to the middle and upper atmosphere. Five nights of temperature and density profiles retrieved from the Utah State University Rayleigh-scatter lidar were used identify the diurnal tide and its harmonics. The amplitudes and phases for these tides were obtained using a least squares fit. The $n=1-4$ tides were then removed from the data at each altitude and a Fourier analysis was done for each night to view the higher order harmonics. Evidence of nonmigrating oscillations, such as from gravity waves, affecting the resulting peak frequencies can be seen. Peak frequencies in the temperatures and densities were shown to match, with only differing relative amplitudes, providing us with two independent observations of the same phenomena and proof that we can use absolute neutral densities to study atmospheric waves.

1. Introduction

Atmospheric tides are oscillations that occur on a global scale in atmospheric fields such as temperature, pressure, density and wind. The periods of these tides are subharmonics of a solar or lunar day. The solar diurnal tide has a period of 24 h while the lunar diurnal tide has a period of 24.8 h. The solar and lunar semidiurnal tides have periods of 12 h and 12.4 h, respectively. Other harmonics exist as integer fractions of 24 h and 24.8 h. Lunar tides are driven by the gravitational pull of the moon (see Sandford et al., 2006) for analysis of lunar tides observed in meteor radar data). Solar tides are driven mainly by thermal excitation and, to a much lesser extent, the gravitational pull of the sun.

The most significant driver of atmospheric tides comes from thermal excitation due to solar radiation. Solar radiation absorption by H₂O in the troposphere and O₃ in the stratosphere are the most well-known tidal sources (Chapman & Lindzen, 1970; Forbes et al., 2006). Tides generated in the lower atmosphere will propagate up and away from their source, transporting energy and momentum in to the middle and upper atmosphere (Oberheide et al., 2007; Teitelbaum & Vial, 1981). This makes studying tides in the atmosphere important for understanding the dynamics and energetics of Earth's middle and upper atmosphere and can be used to couple the lower and middle atmospheres together.

Identifying the diurnal and semi-diurnal tides using RSL observations is difficult due to the nighttime-only observations. There have been studies that use multiple consecutive nights of observations to attempt to identify the diurnal and semidiurnal tidal amplitudes and phases (Dao et al., 1995; Leblanc et al., 1999; Meriwether et al., 1998) and then to compare their results with model results. In this chapter, a similar approach is used. Five consecutive nights of observation during July of 2003 are identified to use for this tidal study. Attempts were made to establish the presence of the tidal influences using Fourier analysis and the Lomb-Scargle method to find the most influential frequencies on these nights both consecutively and individually.

2. Classical tidal theory

In classical tidal theory, tides are treated as perturbations of state variables, such as temperature or density, in the atmosphere. This treatment of classical theory, here, follows that of Forbes (1995) and Oberheide (2006). The atmosphere is assumed to be horizontally stratified with negligible viscosity such that the zonal, following longitude, mean wind and temperature gradient are zero. These assumptions allow us to represent the atmospheric wave motions as linear perturbations in an initially motionless state. The linearized equations for perturbations in spherical coordinates are (Holton, 1975):

$$\frac{\partial u}{\partial t} - 2\Omega \sin(\theta) v + \frac{1}{a \cos\theta} \frac{\partial \Phi}{\partial \lambda} = 0, \quad (6.1)$$

$$\frac{\partial v}{\partial t} + 2\Omega \sin(\theta) u + \frac{1}{a} \frac{\partial \Phi}{\partial \lambda} = 0, \quad (6.2)$$

$$\frac{\partial^2 \Phi}{\partial t \partial z} + w N^2 = \frac{\kappa J}{H}, \quad (6.3)$$

$$\frac{1}{a \cos \theta} \left[\frac{\partial u}{\partial \lambda} + \frac{\partial}{\partial \theta} (v \cos \theta) \right] + \frac{1}{\rho_0} \frac{\partial}{\partial z} (\rho_0 w) = 0. \quad (6.4)$$

where

- u zonal (eastward) velocity
- v meridional (northward) velocity
- w upward velocity
- Φ geopotential height
- N^2 buoyancy frequency squared = $\kappa g/H$
- Ω Earth's angular velocity
- ρ_0 density $\propto e^{-z/H}$
- z altitude
- λ longitude
- θ latitude
- κ $R/c_p \approx 2/7$
- J heating rate per unit mass
- a Earth's radius
- g acceleration due to gravity
- H scale height

t time

Equations 6.1 and 6.2 represent the local conservation of momentum in the zonal and meridional direction, Equation 6.3 describes the energy and Equation 6.4 is the continuity equation. Now let s be the zonal wavenumber and σ the frequency of waves that propagate longitudinally so that:

$$\{u, v, w, \Phi, J\} = \{\hat{u}, \hat{v}, \hat{w}, \hat{\Phi}, \hat{J}\} e^{i(s\lambda - \sigma t)}. \quad (6.5)$$

In this convention, the zonal wavenumber, s , is a positive integer, with $s = 0$ allowed, so that positive values for the frequency, σ , correspond to waves that propagate eastward while negative values correspond to westward propagating waves. By substituting Equation 6.5 into Equations 6.1-6.4, substituting $\partial/\partial t \rightarrow -i\sigma$ and $\partial/\partial \lambda \rightarrow is$, allows us to combine these equations into a single second-order partial differential equation for $\hat{\Phi}(z, \theta)$:

$$-\left(\frac{i\sigma}{\epsilon gh} \mathcal{L}\right) \hat{\Phi} + \frac{1}{\rho_0} \frac{\partial}{\partial z} \left(\frac{\rho_0 i\sigma}{N^2} \frac{\partial}{\partial z} \hat{\Phi} \right) = -\frac{1}{\rho_0} \frac{\partial}{\partial z} \left(\frac{\rho_0 \kappa f}{HN^2} \right), \quad (6.6)$$

$$\mathcal{L} = \frac{\partial}{\partial \mu} \left[\frac{1 - \mu^2}{\eta^2 - \mu^2} \frac{\partial}{\partial \mu} \right] - \frac{1}{\eta^2 - \mu^2} \left[-\frac{s(\eta^2 + \mu^2)}{n(\eta^2 - \mu^2)} + \frac{s^2}{1 - \mu^2} \right], \quad (6.7)$$

where $\mu = \sin(\theta)$, $\epsilon = \frac{(2\Omega a)^2}{gh}$, $\eta = \sigma/2\Omega$ and h is a separation constant referred to as

the equivalent depth.

Further separation of latitude, θ , and altitude, z , can be done by letting:

$$\hat{\Phi} = \sum_n \Theta_n(\theta) G_n(z), \quad (6.8)$$

$$\hat{f} = \sum_n \Theta_n(\theta) J'_n(z) \quad (6.9)$$

From Equations 6.1, 6.2, 6.5 and 6.8 we can express the horizontal velocity components in terms of Θ_n and G_n :

$$\hat{u} = \frac{\sigma}{4\Omega^2 a} \sum_n U_n(\theta) G_n(z), \quad (6.10)$$

$$\hat{v} = -\frac{i\sigma}{r\Omega^2 a} \sum_n V_n(\theta) G_n(z), \quad (6.11)$$

where

$$U_n = \frac{1}{(\eta^2 - \sin^2 \theta)} \left[\frac{s}{\cos \theta} + \frac{\sin \theta}{\eta} \frac{\partial}{\partial \theta} \right] \Theta_n, \quad (6.12)$$

$$V_n = \frac{1}{(\eta^2 - \sin^2 \theta)} \left[\frac{s \tan \theta}{\eta} + \frac{\partial}{\partial \theta} \right] \Theta_n. \quad (6.13)$$

The resulting equations from separating altitude and latitude are the *vertical structure equation* for an isothermal atmosphere:

$$i\sigma H \left[\frac{1}{\rho_0} \frac{\partial}{\partial z} \rho_0 \frac{\partial}{\partial z} G_n \right] + \frac{1}{\rho_0} \frac{\partial}{\partial z} (\rho_0 \kappa J'_n) = -\frac{i\sigma \kappa}{h_n} G_n, \quad (6.14)$$

and *Laplace's tidal equation* (horizontal structure equation):

$$\mathcal{L}\Theta_n + \epsilon\Theta_n = 0. \quad (6.15)$$

Equation 6.15 represents an eigenfunction-eigenvalue problem where, given specified s and σ , a complete set of orthogonal eigenfunctions (Θ_n , called *Hough functions*) and eigenvalues (ϵ) can be obtained. Hough functions can be expressed as an infinite sum of associated Legendre polynomials. Each pair of eigenfunctions and eigenvalues constitute a mode of oscillation. These modes can be identified by expressing s , the zonal wavenumber or number of wave crests occurring along a latitude circle, and σ , the frequency. The meridional index, n , provides information on the number of latitudinal nodes and symmetry characteristics of Θ_n .

The vertical and horizontal components are coupled through the set of eigenvalues referred to as the equivalent depth, h_n given by $h_n = \frac{H}{1-\kappa}$. The vertical wavelength is given by:

$$\lambda_{z,n} = \frac{2\pi H}{\alpha_n} = \frac{2\pi H}{\sqrt{\frac{\kappa H}{h_n} - \frac{1}{4}}}. \quad (6.16)$$

For large or negative values of h_n the waves are evanescent or trapped. To observe vertically propagating waves the condition $0 < h_n < 4\kappa H$ must be met.

3. Migrating and nonmigrating tides

Migrating solar tides propagate westward and follow the apparent motion of the Sun. This is due to the primary driving force of solar radiation absorption by water vapor and ozone in the troposphere and stratosphere respectively (Oberheide et al., 2002).

Due to the rotation of the Earth, the solar radiation input into the atmosphere is periodic from the perspective of a ground-based observer. The period of these oscillations are subharmonics of a solar day.

Nonmigrating tides are waves which do not propagate following the apparent motion of the sun. They can propagate eastward, westward or remain stationary. These tides are produced through various processes such as interactions brought on by longitudinal differences in topology and land-sea contrast (Oberheide et al., 2007), through nonlinear interactions between global-scale waves, and large-scale latent heat release due to deep convective activity in the troposphere (Hagan & Forbes, 2002). Due to the sources of oscillation, nonmigrating tidal components are typically less significant than migrating tidal components.

Tidal oscillations can be represented by taking the real part of Equation 6.5:

$$A_{n,s} \cos(s\lambda - \sigma_n t - \phi_{n,s}), \quad (6.17)$$

where $A_{n,s}$ is the amplitude of the oscillation of the observed field, $\phi_{n,s}$ is the tidal phase and n is a positive integer that denotes a subharmonic of a solar day. A wave crest (maximum amplitude) occurs when

$$\phi_{n,s} = s\lambda - \sigma_n t \quad (6.18)$$

is satisfied. The horizontal wave speed of the tide, c_{ph} is obtained by differentiating Equation 6.18.

$$s d\lambda - \sigma_n dt = 0 \quad (6.19)$$

$$c_{ph} \equiv \frac{d\lambda}{dt} = \frac{\sigma_n}{s} \quad (6.20)$$

For solar tides, the n^{th} harmonic frequency is $\sigma_n = n\Omega$ where Ω is the rotation rate of the Earth ($\Omega = (2\pi/24) h^{-1}$). Equation 6.17 can be represented in terms of local time, $t_L = t + \lambda/\Omega$:

$$A_{n,s} \cos((s+n)\lambda - n\Omega t_L - \phi_{n,s}). \quad (6.21)$$

For migrating solar tides, $s = -n$ (for $n < 0$ which indicates westward propagating tides), Equation 6.21 becomes:

$$A_{n,s} \cos(|n|\Omega t_L - \phi_{n,s}). \quad (6.22)$$

This shows that for migrating solar tides, the amplitude variations that occur at the

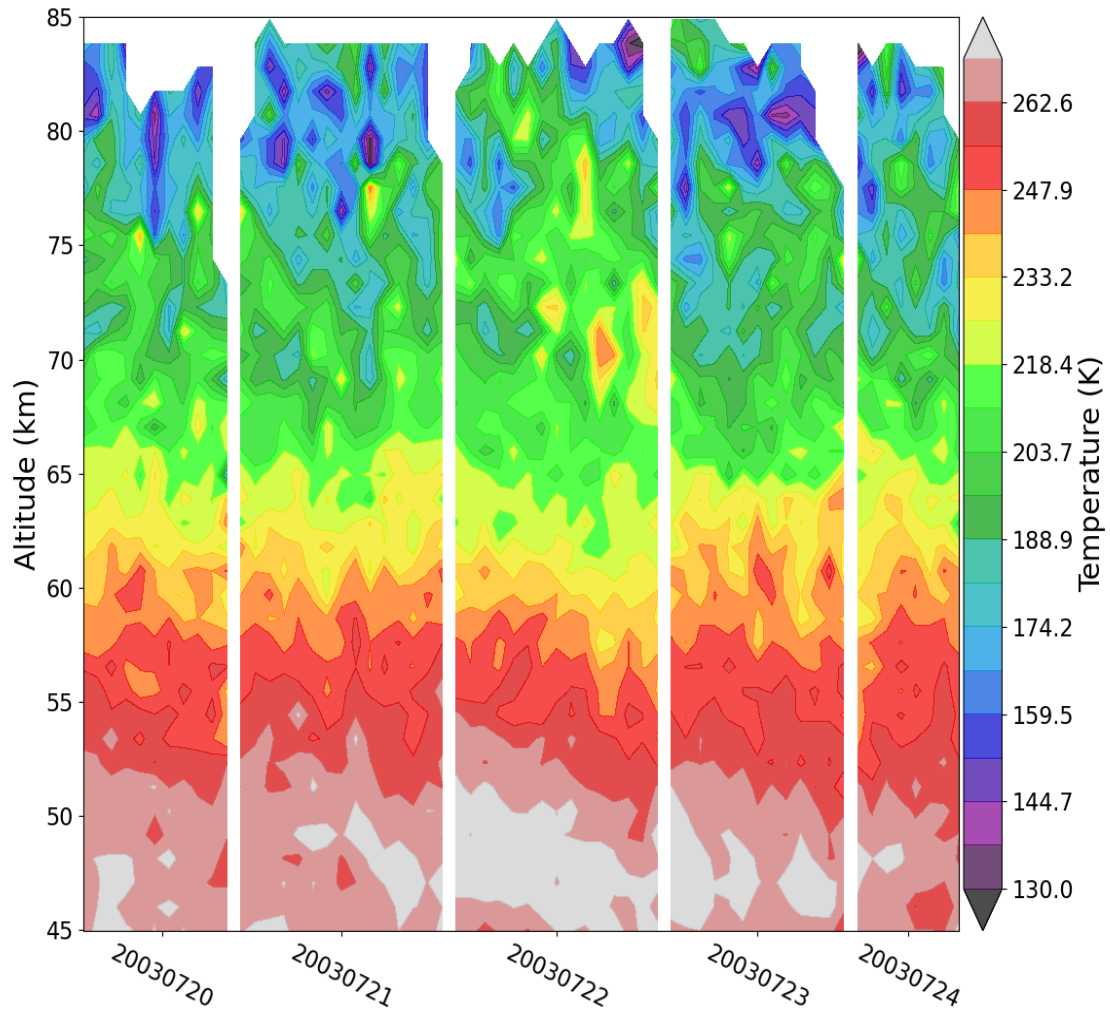


Figure 6. 1: Plot of temperature profiles with 30-minute and with 1-km altitude resolution from the nights of July 20-24, 2003. The gap between each night is scaled down for easier viewing of the nightly temperatures.

same local time are the same at all longitudes. The diurnal tide occurs when $n = -1$ and $s = 1$, moving westward with the apparent motion of the Sun. Because the RSL at

USU observes from a fixed geographical location with a stationary vertical beam, the non-migrating components cannot be distinguished from the migrating components.

4. USU RSL Tides

Five consecutive nights of data from July 20 through July 24, 2003, totaling 62 hours of observation, were chosen for this study. The observations for each night were reduced into temperature (Figure 6.1) and absolute density (not shown) profiles with a 1 km vertical resolution and 30-minute temporal resolution. The gap between each night in the figure is scaled down for easier viewing of the temperatures. Because the RSL only operated at night, it is difficult to observe the long period wave structure on individual nights and so we looked at multiple consecutive nights to determine their influences. Due to the gaps in data between nights of observation, a Lomb-Scargle periodogram (LSP) analysis was used on the five nights to identify the prominent peaks in frequency in both the temperature and density profiles. Figure 6.2 shows the LSP at eight different altitudes from the RSL density and temperature profiles. Here we see the temperature and density LSPs are nearly identical, both showing prominent diurnal and semidiurnal tidal signatures. Also shown are the locations where the $n=3$, 4, and 5 harmonics are located. The peaks of these higher-order harmonics are slightly shifted from the center frequency which might indicate interference from other wave sources such as gravity waves. The large relative power values for the diurnal and semidiurnal signatures indicate the strong presence of these tides. The larger width at the base of

the 24-hour location is likely due to the relatively small number of observed hours. With more nights, or longer observations such as are available in the winter, the width of the base would likely narrow.

Having established the presence of the tides with the LSP, we used a least-squares fit to find the amplitude and phase for each tidal component. Because the RSL operates only at night, the diurnal and semidiurnal components are difficult to find on individual nights. We must, then, use the five consecutive nights to generate a composite view of these tides. To do this, the data were arranged in order by hours past

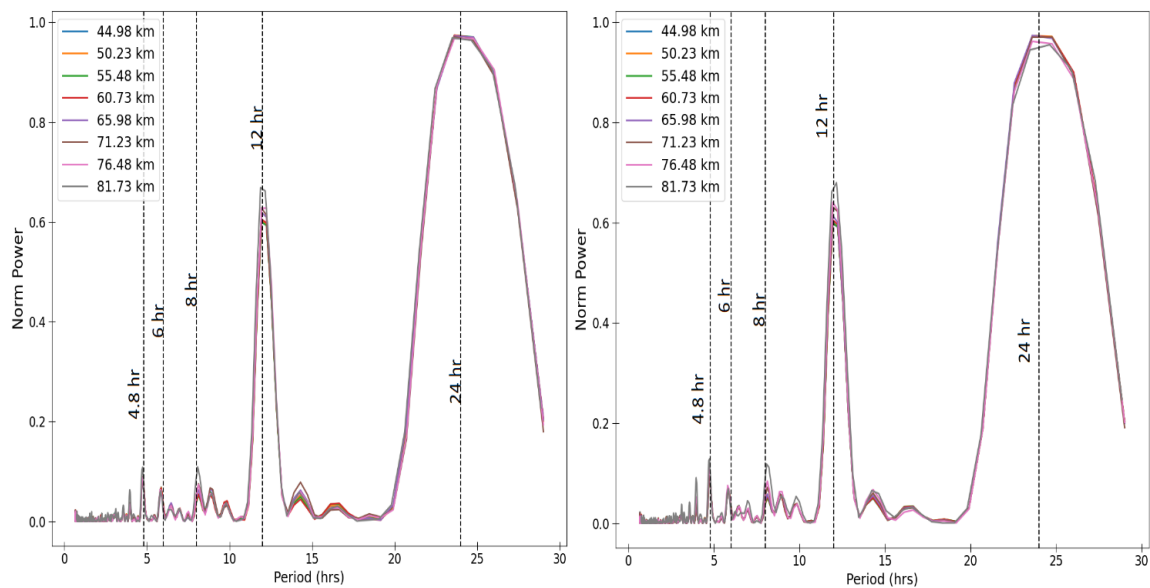


Figure 6.2: Lomb-Scargle periodograms of the temperature (left) and density (right) from July 20-24, 2003 (62 hours total). Both periodograms show remarkably similar peaks for the $n=1-5$ tides.

midnight, UTC, on July 20th. The amplitude profiles are plotted in Figure 6.3. The blue profiles are the temperature amplitudes, and the red profiles are the density

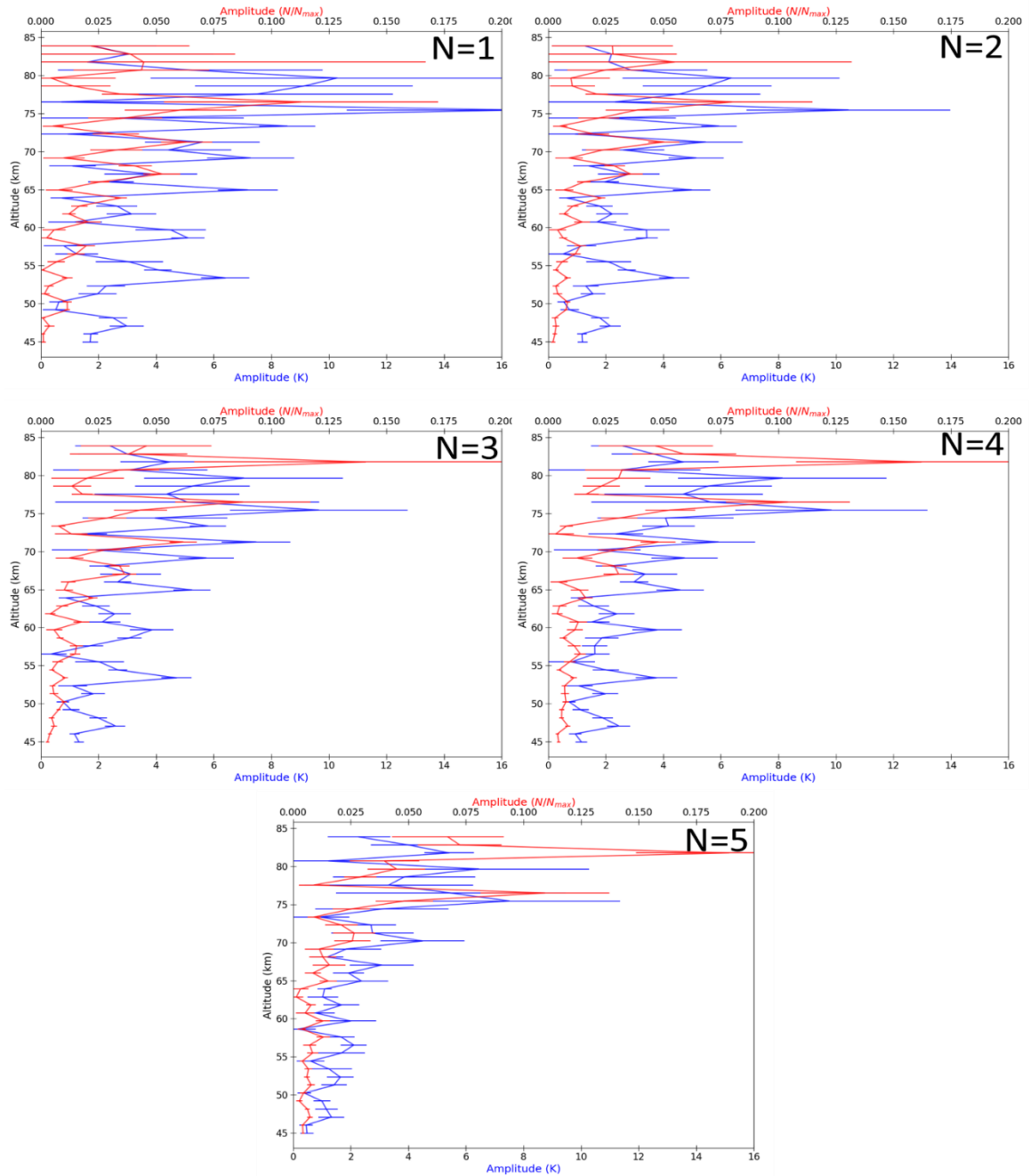


Figure 6.3: Plot of the temperature (blue) and density (red) amplitudes of the first 5 harmonics of the diurnal tide (including the diurnal tide itself) from July 20-24, 2003. The peaks of the amplitudes appear to be offset by about 3 km in altitude.

amplitudes, which were plotted relative to the 5-day mean density. The peak temperature amplitudes occur around 75 km with the peak amplitude found in the

diurnal component. The density amplitude peaks appear to be offset from the temperature peaks by $\sim 2-3$ km with large peaks found around 77 km in all amplitude profiles. The largest amplitudes are found in the higher order tides, with the $n=5$ tide

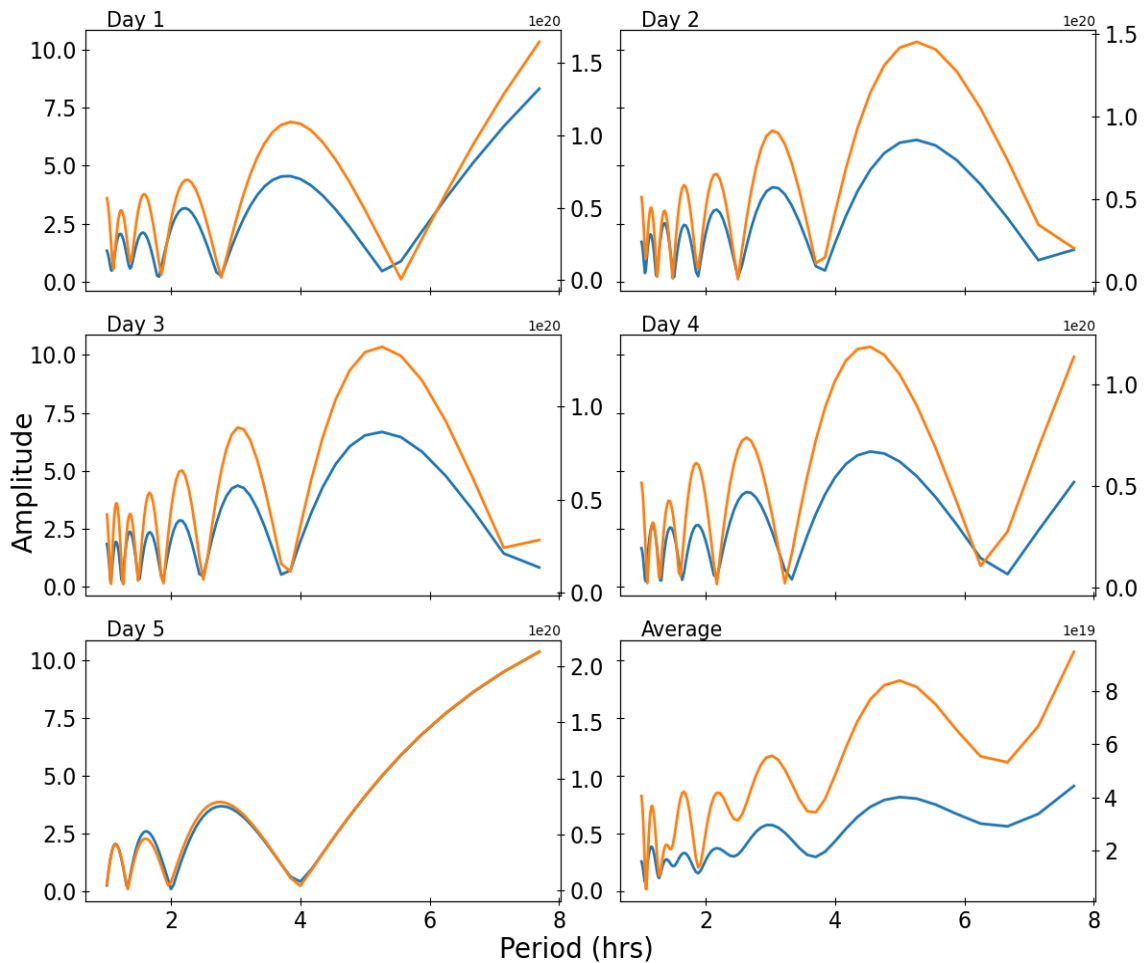


Figure 6.4: Frequency spectrum of temperatures (blue) and densities (orange) at 65 km. The $n=1-4$ tidal components have been removed from each night. Both temperature and density peaks appear at the same frequencies which shows that the FFT is able to see the same waves in both variables.

producing a maximum amplitude around 83 km. This difference, or offset, in altitude with the temperature amplitude peaks agrees with what was found in Chapter 5 where

it was noted that the altitude where the maximum and minimum temperature and densities occur differs by ~ 10 km. The offset in the altitude of the peak amplitudes may be contributing to these differences in the altitudes of the climatological extrema. The averaged vertical wavelength is 16.1 ± 1.3 km for the temperature and 18.1 ± 1.9 km for the density.

Next, we looked at the frequency spectrum for each night to see what oscillations are left after subtracting the main tidal components. This was done by using the coefficients found by using a least squares fit with Equation 6.22, producing the amplitude and phase components at each altitude. We then generated a superposition of the $n=1-4$ tides at each altitude using these coefficients and then subtracted each from the 5-day temperatures (and densities). A fast-Fourier transform (FFT) was used to convert the data into frequency space for each night at each altitude. In order to produce reliable spectra, the FFT requires uniform spacing in the data. This limits the top altitudes of the analysis as they vary in height for each 30-minute profile, some of which do not extend as high as others. Thus, the temporal data may have gaps where the temperature or density values are missing and the FFT is less reliable at these altitudes. This starts to occur in most of the 5 nights at around 80 km.

Figure 6.4 shows the resulting temperature and density frequency spectra for each night at 65 km. The first and last nights are notably different than the middle nights. This is because there were far fewer 30-minute profiles for use in the analysis. Otherwise, we see that the density and temperatures exhibit remarkably similar wavelike behavior over the course of a given night with the relative amplitudes being

the most notable difference. The peak amplitudes differ in frequency for each night, with nights 2 and 3 producing the closest spectra to one another. The peak amplitude in the densities occurs on night 2 centered around a period of 5.25 hours. As this is not a harmonic of the diurnal tide, it likely represents a superposition of waves included within the width of the peak such as the $n=4, 5$ and 6 tides with likely higher frequency gravity waves included. As such, it is likely that gravity waves are a major factor as to why we do not see the same peaks for each night. This is because gravity waves are, generally, shorter term phenomena that are produced by weather related or topographically related sources and likely will not be present over consecutive nights (Beissner, 1997; Ehard et al., 2016; Pugmire, 2018;). This has an impact on the location of the peak frequencies day to day. The peak in the temperatures and densities do occur centered around the same frequencies, suggesting we are seeing the same waves in both variables, though with differing relative amplitudes with respect to one another.

5. Conclusions:

Temperature and density tides were explored using RSL observations over 5 nights in July, 2003. A LSP was used to identify the dominant periods of oscillation, showing strong diurnal and semidiurnal signatures over the 5 nights. There were also strong signals in the 8-hour and 6-hour tides. The average vertical wavelength of the tides was found to be 16.1 ± 1.3 km for the temperature and 18.1 ± 1.9 km for the density. A study of RSL diurnal tidal perturbations by Dao et al. (1995) found the diurnal

amplitude at Haleakala, Maui in June 1993 to be 19.7 ± 1.1 km. Though the latitude is quite different, and the studies are 8 years apart, our values for the vertical wavelength are consistent with this value.

A superposition of sine functions was used to remove the influence of the $n=1-4$ tides from the signal over 5 nights and an FFT analysis was done for each night using the results at each altitude. The density and temperature FFTs agree in the frequencies of the dominant oscillations, with only minor variations in relative amplitudes. This agreement between variables that both originate from the same RSL observations, but whose data reduction methods are independent from one another, gives credence to the validity of the frequencies found in the FFT analysis.

References:

- Beissner, K. C. (1997). *Studies of Mid-latitude Mesospheric Temperature Variability and Its Relationship to Gravity Waves, Tides, and Planetary Waves*. All Graduate Theses and Dissertations. Retrieved from <https://digitalcommons.usu.edu/etd/4687>
- Chapman, S., & Lindzen, R. S. (1970). *Atmospheric tides: thermal and gravitational*. Springer Science & Business Media.
- Dao, P. D., Farley, R., Tao, X., & Gardner, C. S. (1995). Lidar observations of the temperature profile between 25 and 103 km: Evidence of strong tidal perturbation. *Geophysical Research Letters*, 22(20), 2825–2828. <https://doi.org/10.1029/95GL02950>
- Ehard, B., Achtert, P., Dörnbrack, A., Gisinger, S., Gumbel, J., Khaplanov, M., et al. (2016). Combination of Lidar and Model Data for Studying Deep Gravity Wave Propagation. *Monthly Weather Review*, 144(1), 77–98. <https://doi.org/10.1175/MWR-D-14-00405.1>

- Forbes, J. M. (1995). Tidal and planetary waves. *The Upper Mesosphere and Lower Thermosphere: A Review of Experiment and Theory, Geophys. Monogr. Ser., 87*, 67–87.
- Forbes, J. M., Russell, J., Miyahara, S., Zhang, X., Palo, S., Mlynczak, M., et al. (2006). Troposphere-thermosphere tidal coupling as measured by the SABER instrument on TIMED during July–September 2002. *Journal of Geophysical Research*, *111*(A10), A10S06.
<https://doi.org/10.1029/2005JA011492>
- Hagan, M. E., & Forbes, J. M. (2002). Migrating and nonmigrating diurnal tides in the middle and upper atmosphere excited by tropospheric latent heat release. *Journal of Geophysical Research*, *107*(D24), 4754. <https://doi.org/10.1029/2001JD001236>
- Holton, J. (1975). The dynamic meteorology of the stratosphere and mesosphere(Book). *Research Supported by the National Science Foundation Boston, American Meteorological Society(Meteorological Monograph., 15*(37).
- Leblanc, T., McDermid, I. S., & Ortland, D. A. (1999). Lidar observations of the middle atmospheric thermal tides and comparison with the High Resolution Doppler Imager and Global Scale Wave Model: 2. October observations at Mauna Loa (19.5°N). *Journal of Geophysical Research: Atmospheres*, *104*(D10), 11931–11938.
<https://doi.org/10.1029/1999JD900008>
- Meriwether, J. W., Gao, X., Wickwar, V. B., Wilkerson, T., Beissner, K., Collins, S., & Hagan, M. E. (1998). Observed coupling of the mesosphere inversion layer to the thermal tidal structure. *Geophysical Research Letters*, *25*(9), 1479–1482.
<https://doi.org/10.1029/98GL00756>
- Oberheide, J., Hagan, M. E., Roble, R. G., & Offermann, D. (2002). Sources of nonmigrating tides in the tropical middle atmosphere: SOURCES OF NONMIGRATING TIDES. *Journal of Geophysical Research: Atmospheres*, *107*(D21), ACL 6-1-ACL 6-14.
<https://doi.org/10.1029/2002JD002220>
- Oberheide, J., Wu, Q., Killeen, T., Hagan, M., & Roble, R. (2007). A climatology of nonmigrating semidiurnal tides from TIMED Doppler Interferometer (TIDI) wind data. *Journal of Atmospheric and Solar-Terrestrial Physics*, *69*(17–18), 2203–2218.

Pugmire, J. R. (2018). *Mesospheric Gravity Wave Climatology and Variances Over the Andes Mountains*. All Graduate Theses and Dissertations. Retrieved from <https://digitalcommons.usu.edu/etd/7387>

Sandford, D. J., Muller, H. G., & Mitchell, N. J. (2006). Observations of lunar tides in the mesosphere and lower thermosphere at Arctic and middle latitudes. *Atmos. Chem. Phys.*, 11.

Teitelbaum, H., & Vial, F. (1981). Momentum transfer to the thermosphere by atmospheric tides. *Journal of Geophysical Research*, 86(C10), 9693. <https://doi.org/10.1029/JC086iC10p09693>

CHAPTER 7

CONCLUSIONS AND FUTURE WORK

1. Summary and Conclusions

The work in this dissertation is largely centered around a new approach at Rayleigh-scatter lidar (RSL) data reduction. The optimal estimation method (OEM) was introduced to the RSL community by Sica and Haeefele (2015) as an improvement in temperature reduction over the long-used HC method (Hauchecorne & Chanin, 1980). The benefits of OEM over HC include a more robust uncertainty analysis and a well-defined top altitude, below which the temperatures are deemed valid. This method was used to reduce RSL temperatures obtained at Utah State University and produce temperature climatologies from the original data (1993-2004) and the upgraded system data (2014-2015). The OEM climatologies were compared with temperature climatologies produced from the original data using the HC method (Herron & Wickwar, 2018) and with MSIS2.0 model temperatures. The OEM temperatures were found to be slightly higher overall than the HC temperatures, particularly above 85 km. Other RSL groups using the HC method have suggested that the top 10 km to 15 km should be removed from any analysis because it is difficult to know how much the seed temperature, used at the top altitude in the profile to retrieve temperatures, is influencing these lower altitude values. This is not a problem for OEM since the method accounts for all inputs, even calculating the uncertainties for each component in the forward model, and uses the averaging kernel to define the topmost valid altitude in the

profile by defining the amount of influence the a priori temperature has on the resulting temperature profile.

The OEM was used, for the first time, to obtain absolute neutral densities (as opposed to temperatures) from RSL observations. This novel approach was developed by using a modified version of the forward model used in the temperature reduction. Previous to this work, a model value was needed to normalize RSL relative neutral densities in order to obtain an absolute scale. This introduces large uncertainties, which are difficult to define for model variables, into the analysis. Work done by Barton et al. (2016) reflects this issue as they produce climatologies of USU densities normalized to various models at 45 km which differ greatly in absolute scale. Furthermore, Moser (2019) showed that reanalysis model temperatures vary greatly from the USU RSL values at 45 km. Since the RSL values at this altitude are well defined we know the issue is with the model values. This is a problem when trying to normalize densities since this process relies on combining two model variables, the temperature and pressure, to generate the density, using the ideal gas law. Densities retrieved using the OEM provide a robust uncertainty budget with a well-defined top cutoff altitude. Like the temperature retrieval (Sica & Haefele, 2015), the a priori density does not have a large impact on the resulting density profile.

Using the RSL absolute densities reduced using OEM, we generated the first density climatologies. Results showed that around 70 km there is a region of high densities that occurs in the summer and of low densities in the winter. This was apparent in both the original lidar data and the new extended lidar data. The upgraded

lidar shows another possible set of maxima and minima centered around 110 km, with the low density occurring in the summer and the high density in the winter, though because this is the upper limit of the climatology, we cannot say for certain these are the correct altitudes for the maxima and minima. Comparisons of MSIS2.0 model densities and USU densities normalized to MERRA-2 show high- and low-density regions like those found in the OEM density climatology. The MERRA-2 normalized climatology shows similar higher frequency oscillations, which equate to periods less than that of the semi-annual oscillation (<180 days), above 85 km. The temperature and density annual percent variations were directly compared showing the time of year when the maxima/minima occur are the same for both, but opposite to each other so that when the density experiences a maximum the temperature experiences a minimum. We also see a shift in altitude of ~10 km between where the density and temperature extrema occur.

A case study into tides was presented using the RSL temperatures and densities focusing on the nights of July 20-23, 2003. The reduction was done using a 30-minute time resolution with a 1 km altitude resolution. A Lomb-Scargle periodogram was used to identify the diurnal tide and its harmonics to verify they are present. Once identified, a least squares fit was applied across the 5 nights at each altitude to retrieve the amplitudes and periods of the $n=1-5$ tides. These were used to generate a superposition of the $n=1-4$ tides in order to remove their influence from each night. Once these were removed, an FFT was used to identify the peak frequencies left over. It was shown that the density and temperatures both show peaks at the same frequencies which indicates

the waves are identifiable in both the density and temperature profiles. This provides us with another state variable with which to study atmospheric waves. We also saw that the frequency of the peaks changed day to day suggesting that shorter period, non-migrating harmonics are present such as gravity waves.

2. Future Work

The introduction of a new method of obtaining absolute neutral densities opens the door to many new studies. We now have another state variable with which to study atmospheric phenomena. As such, we can use these data to verify other studies performed using temperature such as characterizing gravity waves (Kafle, 2009), identifying sudden stratospheric warming events with RSL observations (Sox, 2016), and regional comparisons of climatologies (Herron, 2007).

With an upgraded lidar system, extending the altitude range above 120 km, we can study the changes in the neutral composition directly. This can be done through further modification of the OEM forward model to retrieve the individual components making up the neutral atmosphere. We can then study at what point O begins to become important in the neutral composition. With enough observations over time a climatology of the neutral atmosphere in the lower thermosphere will be possible to create. This would provide valuable data for the improvement of models such as MSIS2.0.

Further work is ready to be done with atmospheric pressure. By obtaining the pressure, we will add yet another state variable that can be used to study the atmosphere. This can be done in two ways. We can use the ideal gas law to simply calculate the pressures using the OEM temperatures and densities. We can also formulate a new forward model with the OEM to extract pressures directly from RSL observations. Apart from providing an interesting study into the OEM itself by comparing the resulting pressures with each method, we can then see how the pressure changes over a composite year and where its extrema are located in altitude and compare these results with those from Chapter 5.

References

- Barton, D. L., Wickwar, V. B., Herron, J. P., Sox, L., & Navarro, L. A. (2016). Variations in Mesospheric Neutral Densities from Rayleigh Lidar Observations at Utah State University. *EPJ Web of Conferences*, 119, 13006.
<https://doi.org/10.1051/epjconf/201611913006>
- Hauchecorne, A., & Chanin, M.-L. (1980). Density and temperature profiles obtained by lidar between 35 and 70 km. *Geophysical Research Letters*, 7(8), 565–568.
<https://doi.org/10.1029/GL007i008p00565>
- Herron, J., & Wickwar, V. B. (2018). Mid-Latitude Climatologies of Mesospheric Temperature and Geophysical Temperature Variability Determined with the Rayleigh-Scatter Lidar at ALO-USU. *Journal of Geophysical Research*, 59.
- Herron, J. P. (2007). *Rayleigh-Scatter Lidar Observations at USU's Atmospheric Lidar Observatory (Logan, UT) - Temperature Climatology, Temperature Comparisons with*

- MSIS, and Noctilucent Clouds*. All Graduate Theses and Dissertations. Retrieved from <https://digitalcommons.usu.edu/etd/4686>
- Kafle, D. N. (2009). *Rayleigh-Lidar Observations of Mesospheric Gravity Wave Activity above Logan, Utah*. All Graduate Theses and Dissertations. Retrieved from <https://digitalcommons.usu.edu/etd/466>
- Moser, D. K. (2019). *Juxtaposition at 45 km of Temperatures from Rayleigh-Scatter Lidar and Reanalysis Models*. All Graduate Theses and Dissertations. Retrieved from <https://digitalcommons.usu.edu/etd/7434>
- Sica, R. J., & Haefele, A. (2015). Retrieval of temperature from a multiple-channel Rayleigh-scatter lidar using an optimal estimation method. *Applied Optics*, 54(8), 1872. <https://doi.org/10.1364/AO.54.001872>
- Sox, L. (2016). *Rayleigh-Scatter Lidar Measurements of the Mesosphere and Thermosphere and their Connections to Sudden Stratospheric Warmings*. All Graduate Theses and Dissertations. Retrieved from <https://digitalcommons.usu.edu/etd/5227>

CURRICULUM VITAE

Jonathan Price

Department of Physics
 Utah State University, Logan, UT 84322
 Cell Phone (801) 389-3302
 E-mail: jonathanprice1@live.com

Education

PhD, May 2021	Utah State University, Logan, Utah, USA Advisor: Dr. V. Wickwar	August 2015- GPA 3.21
B.S., Physics. 2015	Utah State University, Logan, Utah,	May 2012-May GPA 3.27

Research Interests

Mesospheric density from Rayleigh scatter lidar
 Mesospheric temperatures from Rayleigh scatter lidar
 Data processing and analysis

Research Experience

Graduate Student , Department of Physics, USU May 2021	August 2015- Logan, UT
--	-------------------------------

Dissertation title: Absolute Neutral Densities and Temperatures and their Climatologies in the Middle Atmosphere using an Optimal Estimation Method with Rayleigh-Scatter Lidar Observations obtained at Utah State University

I applied a new lidar temperature reduction technique called the optimal estimation method to data collected at Utah State University. Originally developed in MATLAB, I ported the method into Python and processed the temperatures for the existing USU Rayleigh-scatter lidar observations. I was then able to introduce a novel approach to obtain the absolute neutral densities from Rayleigh-scatter lidar observations building upon the OEM method. Using this method, the neutral densities can be obtained directly from the Rayleigh-scatter lidar observations without direct dependence on a model density value. This new method adds another state variable

with which to study the neutral atmosphere. I am currently working on a paper for publication regarding the new density retrieval method.

I helped improve the lidar to operate two detector channels to collect data in the atmosphere from 35 km to 80 km and 70 km to 120 km. This allows signals to be combined to obtain densities and temperatures from 35 km to 120 km.

I converted all original data processing routines from IDL to Python.

Undergraduate Student, Department of Electrical and Computer Engineering, 2013-2015
USU Logan, UT

I used data collected by the SABER instrument aboard NASA's TIMED satellite to study gravity waves in the upper mesospheric region of the atmosphere.

I used Matlab to process large amounts of data to find multiple peaks in energy profiles that might suggest propagating waves in the atmosphere.

Teaching Experience

Instructor Aug 2016-May 2019

Utah State University

I prepared course content using Canvas, graded assignments, gave instruction and assisted students with lab setups and data analysis. I also held office hours and assigned final grades. I taught basic python analysis techniques to lab students for use in their data analysis.

“Intermediate Laboratory” (Phys 3870), Fall '16,'17,'18
“Advanced Laboratory” (Phys 3880), Spring '17,'18,'19

Lab Teaching Assistant August 2015-May 2016

Utah State University

Intermediate Lab (Phys 3870), Advanced Lab (Phys 3880). I assisted with grading and helping students set up and perform lab projects. I helped students use the observatory telescope for special projects.

Teaching Assistant Spring 2018, Spring 2019

Utah State University

Utilizing the Arduino Microcontroller (Phys 2400) and Physics, Making, And Arduinos

(Phys 3500). I helped develop the Phys 2400 course and provided demonstrations and instructions on simple projects using sensors with Arduino. I taught basic soldering techniques as well. I also assisted by demonstrating more advanced sensors that students could choose to use in their final projects.

Undergraduate Student Mentor

August 2016-Present

Utah State University

I have mentored 7 undergraduate students on their senior research projects (Phys 4900). These projects include searching for exoplanets using the USU observatory, exploring Arduino for use in the physics lab, detecting the redshift of stars using a high resolution spectrometer, creating a spectrometer using a transmission grating with a ccd camera for astronomical spectroscopy and monitoring solar activity using a solar filter with a portable telescope. I helped obtain funding for equipment through the physics department and the office of research and graduate studies at USU as well as SPIE. I worked with students to design experiments and do observations. I helped students prepare posters for presenting their research at the Student Research Symposium at USU. I gave suggestions to improve their final experiment writeup which is submitted to Digital Commons through the USU library.

Publications

Journals

Price, J., Rozum, J., Ware, G., & Baker, D. (2014). Global Nightly OH and O₂ Mesospheric Airglow: Examining a Decade of Measurements Using the NASA SABER Satellite Sensor. The Journal of the Utah Academy of Sciences, Arts, & Letters, 91.
<http://www.utahacademy.org/wp-content/uploads/2015/03/JUASALfulltext2014-finalrevised.pdf>

Presentations

Price, J. Absolute Densities in the Mesosphere. Utah State University Department of Physics Colloquium. October 24, 2017.

Price, J. Tidal Observations throughout the Mesosphere using Rayleigh Lidar Data. Utah State University Department of Physics Colloquium. September 25, 2018.

Price, J. Correlation of OH and O₂ Airglow in the Night-Time Mesosphere. Utah Academy of Sciences, Arts, & Letters 2015 Annual Conference. Snow College, Ephraim, UT. March 27, 2015. <http://www.utahacademy.org/wp-content/uploads/2015/01/JUASAL-fulltext-final-2015-corrected.pdf>

Posters

Price, Jonathan L.; Wickwar, Vincent B.; Herron, Joshua P.; "Absolute Neutral Densities in the Mesosphere from ALO-USU Rayleigh Lidar Observations" (2018). 2018 CEDAR Workshop, Santa Fe, NM.

Price, Jonathan L.; Wickwar, Vincent B.; Herron, Joshua P.; "Obtaining Absolute Neutral Densities in the Mesosphere Using Rayleigh-Scatter Lidar Observations with Reanalysis Models" (2018). AGU Fall Meeting 2018, Washington, DC.

Price, Jonathan L.; Wickwar, Vincent B.; Sox, Leda; Emerick, Matthew T.; Herron, Joshua P.; Elliott, Shayli; Ward, Bryant; and Lovelady, Benjamin, "Obtaining Continuous Observations from the Upper Stratosphere to the Lower Thermosphere Using the ALO-USU Rayleigh-Scatter Lidar." (2016). 2016 Joint CEDAR-GEM Workshop, Santa Fe, NM. *Posters*. Paper 27.

http://digitalcommons.usu.edu/atmlidar_post/27

Price, J., Griffin, D. Stellar Spectroscopy. Student Research Symposium, Utah State University, Logan, UT. April 2015.

<http://digitalcommons.usu.edu/researchweek/ResearchWeek2015/All2015/192/>

Awards

2017	Howard L. Blood Summer Fellowship
2018	Keith Taylor Summer Fellowship
2019-2021	College of Science Summer Fellowship
	Utah NASA Space Grant Consortium Fellowship

Professional Affiliations

International Society for Optics and Photonics (SPIE): USU Chapter Treasurer, May 2016-May 2017

USU Chapter President May 2017-May 2018

USU Chapter Secretary May 2018-May 2019

CEDAR student member

AGU student member

Skills

Languages: English (Fluent), Spanish (Intermediate)

Computer skills: Python, MATLAB, Excel, C, C++, Fusion 360.

General: Mechanical and electrical troubleshooting/repair. Leadership experience in volunteer organizations. Lidar maintenance and operation. Data analysis and modeling. Report writing. Research presentation. Fast learner. Work well with others.